Phenotypic impact of individual conserved neuronal microexons and their master regulators in zebrafish

Laura Lopez-Blanch[1,2,7], Cristina Rodríguez-Marin[1,2,9], Federica Mantica[1,2,9], Luis P. Iñiguez[1,2], Jon Permanyer[1], Elizabeth M. Kita[1], Tahnee Mackensen[1,2], Mireia Codina-Tobias[1,8], Francisco Romero-Ferrero[1,3], Jordi Fernandez-Albert[1], Myriam Cuadrado[4], Xosé R. Bustelo[4,5], Gonzalo G. de Polavieja[3], Manuel Irimia[1,2,6,10]

1 - Centre for Genomic Regulation (CRG), The Barcelona Institute of Science and Technology, Barcelona, Spain.
2 - Universitat Pompeu Fabra (UPF), Barcelona, Spain.
3 - Champalimaud Research, Champalimaud Foundation, Lisbon, Portugal.
4 - Instituto de Biología Molecular y Celular del Cáncer, CSIC and Universidad de Salamanca, Salamanca, Spain.
5 - Centro de Investigación Biomédica en Red de Cáncer (CIBERONC), Instituto de Salud Carlos III, Madrid, Spain.
6 - ICREA, Barcelona, Spain.
7 - Current affiliation: ZeCardio Therapeutics, Sant Feliu de Llobregat, Barcelona, Spain
8 - Current affiliation: Biozentrum, University of Basel, Basel, Switzerland.
9 - Co-second authors
10 - Corresponding author.

Manuel Irimia

Universitat Pompeu Fabra
Dr. Aiguader, 88, 08003 Barcelona, Spain
e-mail: mirimia@gmail.com
Phone: +34933160189, Fax: +34933160099

Abstract

Microexons exhibit striking evolutionary conservation and are subject to precise, switch-like regulation in neurons, orchestrated by the splicing factors *Srrm3* and *Srrm4*. Disruption of these regulators in mice leads to severe neurological phenotypes, and their misregulation is linked to human disease. However, the specific microexons involved in these phenotypes and the effects of individual microexon deletions on neurodevelopment, physiology, and behavior remain poorly understood. To explore this, we generated zebrafish lines with deletions of 18 individual microexons, alongside *srrm3* and *srrm4* mutant lines, and conducted comprehensive phenotypic analyses. We discovered that while loss of *srrm3*, alone or together with *srrm4*, resulted in significant alterations in neuritogenesis, locomotion, and social behavior, individual microexon deletions typically produced mild or no noticeable effects. Nonetheless, we identified specific microexons associated with defects in neuritogenesis (*evi5b*, *vav2*, *itsn1*, *src*) and social behavior (*vti1a*, *kif1b*). Additionally, microexon deletions triggered coordinated transcriptomic changes in neural pathways, suggesting the presence of molecular compensatory mechanisms. Our findings suggest that the severe phenotypes caused by *Srrm3/4* depletion arise from the combined effects of multiple subtle disruptions across various cellular pathways, which are individually well-tolerated.

INTRODUCTION

Alternative splicing, the differential processing of introns and exons in eukaryotic pre-mRNAs, is the main mechanism generating transcriptomic and proteomic diversity in vertebrates. A large fraction of human multi-exonic genes exhibit alternative splicing (Pan, et al. 2008; Wang, et al. 2008), and a substantial portion of it is regulated in a cell type and tissue dependent manner (Tapial, et al. 2017). A paradigmatic example of tissue-specific regulation are neural microexons, tiny exons ranging from 3 to 27 nucleotides (nts) in length (Irimia, et al. 2014). While a few microexons had been anecdotally reported before (e.g., (Worley, et al. 1997; Dergai, et al. 2010)), the discovery of hundreds of microexons regulated in a tight neural-specific manner dates back to a decade ago (Irimia, et al. 2014; Li, et al. 2015). Neural microexons are often completely skipped in most cell types, including stem cells and neural progenitors, and are sharply switched on during neuronal differentiation by their master regulators *Srrm3* and *Srrm4* (Irimia, et al. 2014; Nakano, et al. 2019). More recently, inclusion of a subset of neural microexons has been reported in endocrine pancreatic cells of mammals, where *Srrm3* is also expressed (Juan-Mateu, et al. 2023).

The potential functional relevance of cell type-specific microexons is supported by multiple lines of evidence. First, neural microexons are the most conserved type of alternative splicing described so far, showing remarkable conservation across jawed vertebrates and, in some instances, from human to cephalochordates and arthropods (Torres-Méndez, et al. 2019; Torres-Mendez, et al. 2022). Second, the impact of numerous microexons on protein function has been demonstrated, and they often modulate protein-protein interactions or protein interactions with other molecules (Ellis, et al. 2012; Kjer-Hansen and Weatheritt 2023; Roth, et al. 2023). Third, loss-of-function models for their highly specific master regulators show dramatic phenotypes, particularly in mammals. For instance, a homozygous mouse gene trap for *Srrm4* exhibits strong neurodevelopmental defects (Quesnel-Vallières, et al. 2015), while another gene trap for *Srrm3* also displays multiple neurodevelopmental phenotypes (Nakano, et al. 2019), as well as pancreas-derived physiological alterations (Juan-Mateu, et al. 2023). Moreover, the heterozygous mouse gene trap for *Srrm4* has been shown to have defects on neuronal activity and it exhibits multiple hallmarks of autism spectrum disorder (ASD) (Quesnel-Vallieres, et al. 2016), in line with the reported misregulation of microexons in various human patients with ASD (Irimia, et al. 2014). In zebrafish, we have recently demonstrated that *srrm3* mutants exhibit severe photoreceptor malformations and degeneration, leading to vision loss and early mortality under standard rearing conditions (Ciampi, et al. 2022).

Despite these studies, however, how misregulation of specific microexons leads to the dramatic phenotypes observed for the mutants of their master regulators is still largely unknown. For instance, it is not yet known whether these phenotypes are caused by a few microexon targets with strong effects (e.g., as in the paradigmatic example of Fgfr alternative splicing for *Esrp1/2* (Bebee, et al. 2015; Burguera, et al. 2017)) or by a complex cumulative effect of multiple small molecular impacts. A major limitation is that the cellular and organismal phenotypes caused by the removal or downregulation of individual microexons has only been assessed for a few cases, mainly using mouse models or cell cultures. In many such cases, loss-of-function microexon models show relatively mild but robust phenotypes. Importantly, these phenotypes range from defects on neurite growth (Worley, et al. 1997; Zibetti, et al. 2010; Ohnishi, et al. 2014; Quesnel-Vallières, et al. 2015) to neuronal malfunction and behavioral abnormalities (Wang, et al. 2015; Gonatopoulos-Pournatzis, et al. 2020; Poliński, et al. 2023). However, other cases did not reveal noticeable phenotypes (e.g., (Matalkah, et al. 2022)), and the potential impact of the publication bias towards positive results is difficult to evaluate.

To tackle this major open question, common to other tissue-specific splicing regulators, in this study we generated stable CRISPR-Cas9 deletion mutants in zebrafish for 18 highly conserved neural-specific microexons regulated by *srrm3/4*. We phenotypically characterized these lines,

along with mutant lines for *srrm3* and *srrm4*, across multiple levels, including axon guidance, neurite growth, larval and juvenile locomotion, larval sensory responses, and social behavior in juveniles. In contrast to the marked phenotypes observed for their master regulators, especially *srrm3*, most microexon mutants showed no phenotypes for most tests, with a few notable exceptions. Transcriptomic analysis of mutant larvae and their wild type siblings suggests that coordinated misregulation of specific neural-related pathways may provide functional compensations at the molecular level. In summary, while the presence of non-studied microexon targets with strong functional effects cannot be ruled out, our results are in line with a model in which the phenotypes of the master regulators are caused by the combined impact of multiple milder perturbations affecting many cellular pathways.

RESULTS

Identification and characterization of *srrm3/4*-regulated neural microexons in zebrafish

To identify neural exons and microexons in zebrafish, we employed a similar approach to that described recently for mammals (Juan-Mateu, et al. 2023)(see Methods). Using transcriptome-wide quantifications of exon inclusion for multiple cell and tissue samples from *VastDB* (Tapial, et al. 2017), we identified a total of 708 neural exons with sufficient read coverage in at least five tissues. Of these, 246 (34.8%) corresponded to microexons of 3-27 nt, 139 (19.6%) to 28-51 nt exons and 323 (45.6%) to exons longer than 51 nts (Figure 1 - figure supplement 1A, Table S1). For comparison, we identified 919 neural exons in human with equivalent expression criteria, which showed a similar proportion of microexons (Figure 1 - figure supplement 1A). As in the case of mammalian programs (Juan-Mateu, et al. 2023), a subset of zebrafish neural microexons were also substantially included in endocrine pancreatic cells, whereas smaller fractions were detected in muscle and, less expectedly, immune tissues (Figure 1A). Tissue-specific regulation was validated by RT-PCR assays for all 21 selected conserved neural microexons (see below) using independent RNA samples (Figure 1 - figure supplement 1B).

Neural microexons show sharp progressive upregulation during embryo development (Figure 1B). In terms of function, genes harboring microexons are strongly enriched in Gene Ontology (GO) terms related to vesicle-mediated transport, endocytosis, GTPase activity, synaptic organization and neuron development (Figure 1C), in line with previous studies (Irimia, et al. 2014; Torres-Mendez, et al. 2022). Zebrafish microexons are also significantly more conserved in human than long exons in terms of neural regulation (Figure 1D; P = 6.8e-03, two-sided Fisher's Exact test between microexons and long exons). However, this increased conservation was relatively minor and, in fact, similar at the genomic level ("no event ortholog" in Figure 1D). This contrasts with the reciprocal comparison, where human neural microexons appeared substantially more conserved at the genomic and regulatory level in zebrafish (Figure 1 - figure supplement 1C), and suggests that zebrafish has evolved a larger fraction of lineage-specific microexons. Finally, 191/243 (78.6%) of neural microexons with sufficient read coverage were affected (ΔPSI < -15) by *srrm3/4* loss-of-function in 5 dpf larva and/or retina (see Methods), in contrast to 82/136 (60.3%) and 122/317 (38.5%) exons of length 28-51 nts and longer, respectively (Figure 1E; P = 8.4e-22, two-sided Fisher's Exact test between microexons and long exons). A similar fraction of human orthologs (98/121, 81.0%) responded to the ectopic expression of the regulator in HEK293 cells (Figure 1 - figure supplement 1D). In addition, the genome-wide effect of *srrm3/4* loss-of-function in zebrafish is strongly biased towards small exons (Figure 1F), as previously reported (Ciampi, et al. 2022).

Stable microexon deletions do not compromise viability and overall morphology

To investigate the functional impact of neural-specific *srrm3/4*-regulated microexons, we selected 21 highly conserved microexons for further characterization (Table S2). These microexons were selected based on various criteria, including sharp neural-specific inclusion

and strong *srrm3/4* regulation in zebrafish, as well as high regulatory conservation in human, both in terms of tissue-specificity and *SRRM3/4* regulation (Figure 2A). In addition, we prioritized some microexons for which a molecular function had been reported (e.g., *apbb1*, *itsn1*, *kif1b*, *mef2ca*, *src*), and the host gene had no close paralogs (e.g., *reln*, *madd*, *src*) and/or had important roles in development and neurobiology (*gli2b*, *gli3*, *cdon*, *mef2ca*, *shank3a*, *shank3b*, *reln*). Moreover, we included representatives of the main enriched GO categories (Figure 1C), such as vesicle transport and endocytosis (*itsn1*, *src, vti1a*), GTPase activity (*vav2*, *evi5b, ap1g1, asap1b, madd, dock7*), synapse organization (*shank3a*, *shank3b*) and microtubule binding (*kif1b*).

We generated stable zebrafish lines for the deletion of each of these microexons using the CRISPR-Cas9 system and designing pairs of guide RNAs (gRNAs) targeting the neighboring upstream and downstream intronic sequence (Figure 2B, Table S3; see Methods). We selected two founders for each microexon showing a clean genomic deletion covering the entire microexon. Such deletions are expected to result in normal expression of the host gene but skipping the microexon in every cell, including neurons, which can be validated through RT-PCR assays with primers spanning the neighboring exons (Figure 2B,C and Figure 2 - figure supplement 1). However, for three of these microexons (*spock3*, *pus7*, and *dock7*; asterisks in Figure 2A), the genomic deletion led to the inclusion of cryptic sequences predicted to create frameshifts and thus gene downregulation, and were consequently excluded from subsequent phenotypic analyses. For comparison, we also included mutant lines for the master regulators of microexons, *srrm3* and *srrm4*, as well as the double mutant line (Figure 2D). Our previous work on these lines (Ciampi, et al. 2022) showed that mutation of *srrm3* has a major impact on microexon inclusion in the retina, whereas *srrm4* loss of function has a very small effect.

Initial characterization of the 18 microexon deletions revealed no gross morphological abnormalities and no differences in body size compared to their heterozygous siblings at the juvenile stage (~30 dpf, Figure 2E). Similar results were obtained for *srrm4* mutants. This contrasts with the *srrm3* mutant line, for which we had previously shown that homozygous mutants die between 12-20 dpf, likely due to feeding problems caused by their impaired vision (Ciampi, et al. 2022). Here, we have reared these fish using special conditions that increase food availability, allowing them to reach the adult stage (see Methods). However, adult *srrm3* homozygous mutants were subfertile, showed reduced body size at 90 pdf (Figure 2E; P = 0.007, two-sided t-test) and had multiple locomotor and behavioral abnormalities (Video S1 and see below).

Some microexons exhibit robust defects on neurite outgrowth *ex vivo*

To begin investigating the impact of microexon deletions on zebrafish neurodevelopment, we assessed two phenotypes at the cellular level related to axon guidance and neurite outgrowth. Homozygous *Srrm4* KO mice showed severe defects on axonal midline crossing through the corpus callosum (Quesnel-Vallières, et al. 2015). Thus, to evaluate potential axon guidance alterations, we first studied Mauthner cells in individual 48 hpf larvae. All studied larvae for all microexon deletions appeared normal, as well as those from *srrm3*, *srrm4* and double mutant lines (Figure 2F).

Next, we focused on neurite outgrowth, a phenotypic trait reported to be altered in primary neuronal cultures of homozygous *Srrm4* KO mice (Quesnel-Vallières, et al. 2015), as well as for various loss-of-function models of individual microexons in mouse (e.g. *Kdm1a* (Zibetti, et al. 2010), *Zfyve27* (Ohnishi, et al. 2014; Ohnishi, et al. 2017), *L1cam* (Jacob, et al. 2002)). To robustly quantify neurite growth, we developed a new protocol to generate primary neuronal cultures from zebrafish larvae (Figure 3 - figure supplement 1A, see Methods). In brief, HuC:GFP-positive cells were isolated using Fluorescence-activated Cell Sorting (FACS) at 48

hpf and plated on Poly-D-Lysine coated 8-microwell glass slides (1cm^2/well) at a density of 200,000 cells/well in Neurobasal (NB) supplemented media at 28ºC and 5% CO2. Isolated HuC:GFP-positive cells lose their neurites, which are then progressively regrown in culture, as observed by acetylated tubulin staining (Figure 3 - figure supplement 1B,C). For each microexon deletion, as well as the regulator mutant lines, we measured the longest neurite for each cell at 10 and 24 hours after plating (hap) (Figure 3A). A few microexon deletion mutants showed significantly different neurite length distributions compared to control wild type (WT) larvae at 10 hap and/or 24 hap that were highly robust across replicates and founder lines (Figure 3B-D, Figure 3 - figure supplement 2). Interestingly, deletions resulted in opposite differences in overall neurite length depending on the microexon: decreased (*vav2*), increased (*evi5b*, *itsn1*) or with distinct effects at 10 and 24 hap (*src*). In the case of the regulators, whereas neither *srrm3* nor *srrm4* individual mutants exhibited significant alterations in neurite length, the double mutant had strongly decreased neurite lengths at 10 hap compared to control siblings (Figure 3B-D, Figure 3 - figure supplement 2).

At the molecular level, the microexons in both ITSN1 and SRC have been shown to modulate interaction with DNM1 (Dergai, et al. 2010), which is involved in synaptic vesicle recycling and is important for neurite outgrowth (Bodmer, et al. 2011). In the case of *vav2*, which encodes a Guanine nucleotide exchange factor (GEF), the deleted 15-nt microexon falls close to its RhoGEF domain (Figure 3E). To test if it could affect its GEF activity, we performed a SRF promoter activation assay upon *vav2* overexpression in COS cells, a well-established method to assess VAV protein activity (see Methods). Whereas overexpression of both zebrafish VAV2 isoforms, with and without the microexon, increased reporter activation with respect to the negative control, the microexon-containing isoform displayed significantly stronger activity (Figure 3F,G; ~3-fold increase over the skipped form, P = 4.1e-03, Student's t-test). Finally, the 10-nt microexon in *evi5b* falls at the 3′ of the gene and its inclusion is predicted to generate an alternative C-termini (Figure 3H). Since *evi5b* is a GTPase activating protein (GAP) of *rab11* and overexpression of *rab11* has been reported to increase neurite outgrowth (Eva, et al. 2010), we tested whether microexon inclusion altered its interaction with RAB11. However, NanoBRET assays revealed a strong, but similar, interaction with RAB11 for both EVI5B isoforms (Figure 3I). We thus speculate that microexon inclusion may disrupt the coiled-coil domain at the C-terminus of EVI5B, where interactions with the centrosome occur (Faitar, et al. 2005), perhaps causing changes in subcellular location.

Individual microexon deletions have little impact on larval activity patterns

We next assessed potential defects in larval activity levels, thigmotaxis and habituation to mechanical tapping stimuli. For this purpose, for each line, we placed 5 dpf larvae derived from a cross of two heterozygous parents into individual wells of a 48-well plate and recorded their activity using a DanioVision system during a predefined series of intervals under light or dark conditions (Figure 4A; see Methods). Specifically, after 5 minutes of habituation, we recorded baseline activity in the light for 25 minutes, and then for five alternating intervals of 10 minutes of dark and light. Finally, a series of 30 tappings (1 Hz frequency) was applied. Overall, we found that homozygous *srrm3* and *srrm3/4* mutant lines showed significant and strong alterations for multiple parameters compared to their WT and heterozygous siblings (Figure 4B, Figure 4 - figure supplement 1-14). In contrast, *srrm4* and microexon deletion lines exhibited little or no defects, and those were generally not consistent across clutches and founder lines (Figure 4 - figure supplement 1-14). In particular, *srrm3* mutants had increased activity in baseline and light interval conditions (Figure 4C), whereas the double mutant showed only a significant, yet milder, increase during the light intervals. Interestingly, larvae with homozygous *evi5b* microexon deletion also showed mildly significantly increased baseline activity (Figure 4C). In the case of the transitions between dark and light conditions, and vice versa, *srrm3* and *srrm3/4* mutants had strong and significant alterations in the relative activity response compared to control siblings (Figure 4B,D and Figure 4 - figure supplement 5,6).

This phenotype could be in part due to the impaired vision of these mutants (Ciampi, et al. 2022), although they nonetheless showed a substantial response to changes in the light/dark conditions (Figure 4 - figure supplement 1). In contrast, only double *srrm3/4* mutant larvae displayed significant alterations in habituation to tapping, measured as the difference in activity between the first tap and taps 3-5 or taps 21-30 (Figure 4E). Finally, we also evaluated thigmotaxis, or the preference of a larva to be close to the wall of the well (Figure 4F), since increased time spent in the periphery is generally associated with higher anxiety levels in multiple systems and model organisms. Surprisingly, both *srrm3* and *srrm3/4* mutants showed significant abnormalities in thigmotaxis, but they did so in opposite directions (Figure 4B). Where *srrm3* homozygous mutant fish exhibited a bias towards the periphery in baseline conditions, double *srrm3/4* mutants had a robust and consistent preference for the center of the well, which was significant for baseline, dark and light intervals (Figure 4F,G). In summary, these studies show that, whereas globally misregulating microexons has a major impact on multiple activity and stimuli response patterns, deleting individual microexons has only a minor impact on those patterns.

Effects of global and individual microexon misregulation on juvenile social behavior

Neural microexons were found to be misregulated in the brains of some individuals with ASD (Irimia, et al. 2014). Consistently, heterozygous mice from a *Srrm4* mutant model, which exhibit similar levels of global microexon misregulation as human ASD patients, displayed multiple hallmarks of ASD, including decreased habituation to stimuli and reduced preference for social interactions (Quesnel-Vallieres, et al. 2016). Moreover, a mouse model mimicking the ASD misregulation of a single microexon in *Cpeb4* also showed a range of autistic-like behavioral phenotypes (Parras, et al. 2018). Therefore, we next set out to assess potential social defects in zebrafish mutant microexon lines. For this purpose, we implemented a custom version of the behavioral set-up developed in (Hinz and de Polavieja 2017)(Figure 5 - figure supplement 1) and used *idtracker.ai* (Romero-Ferrero, et al. 2019) to track activity and interactions of pairs of ~1 month old juveniles (Figure 5A; see Methods). For all lines except for the double *srrm3/4* mutant, which could not reach this age, we aimed at blindly assaying at least 10 pairs of each genotype combination (two heterozygous [Het-Het], two homozygous for the deletion [Del-Del] or one of each [Het-Del]), when possible. For each fish on a pair, we quantified different parameters related to locomotion (speed, normal and tangential acceleration, distance traveled), anxiety (distance to the center of the arena) and leadership (time following the other fish in the pair). In addition, we quantified the distance between the two fish from a pair and the overall agreement between their movement vectors (polarization), both of which give a measure of their social preference. Specifically, WT juvenile fish display a very strong social behavior, with small inter-individual distances and highly concordant movements (Hinz and de Polavieja 2017).

We found no statistically significant differences ($P < 0.01$) for any locomotion or anxiety related parameter for any microexon deletion or for either *srrm3* or *srrm4* mutant lines (Figure 5B). This was the case when comparing the average values of the two homotypic pairs (Het-Het vs Del-Del; same "S") or the values of Het and Del fish within heterotypic pairs (Het-Del; different "D"), although some potential trends could be observed (Figure 5B and Figure 5 - figure supplement 2-10). In contrast, *srrm3* mutants as well as two microexon deletions, *vti1a* and *kif1b*, showed significant defects in social parameters (Figure 5B-D). In particular, homozygous Del fish for the three mutations exhibited significantly higher leadership, i.e., an increase in the time spent in front of a paired Het fish, as visually evident in the heatmaps of relative positions (Figure 5C). Increased leadership could, to some extent, be considered an autism-like phenotype, as it suggests reduced social preference in the Del fish compared to the Het one, which tends to follow its pair closely. In line with this, the inter-individual distance was increased in Del-Del pairs compared to other genotype combinations for *srrm3* and *vti1a* (Figure 5D), while the polarization was decreased in *srrm3* mutant pairs (Figure 5 - figure

supplement 9). These differences in social behavior were relatively minor for *vti1a* and *kif1b* mutants, but very strong for *srrm3* fish, which displayed a dramatically reduced social behavior, as it could be also visualized in recordings of groups of five homozygous mutants compared to groups of WT ones (Videos S2 and S3).

Transcriptomic analyses suggest potential compensatory changes through regulation of neural-related pathways

Given the minor phenotypes we observed for most microexon deletions, it is conceivable that defects in individual protein functions are compensated for by other molecular changes. Hence, we aimed at assessing global transcriptomic alterations in microexon mutants lines. For this purpose, we generated RNA-seq data for pools of ~10 5 dpf homozygous mutant larvae (Del) and wild type siblings (WT) for the 18 microexon deletions, as well as for the *srrm3* mutant line (Figure 6A, Figure 6 - figure supplement 1 and Table S6; see Methods). As expected, all microexon deletions led to minor changes in expression for most genes (absolute delta corrected VST expression < 0.5; Figure 6B). To identify potential compensatory changes, we first focused on changes in the expression of the host gene as well as its closely related paralogs. A few microexon deletions resulted in substantial relative changes in the expression of the host gene (e.g., *apbb1*, *mef2ca, kif1b*), particularly towards increased levels, and/or of some of the paralogs (e.g., *apbb1*, *evi5b*, *gli3, mef2ca, shank3b*) (Figure 6B). Some of these changes may have straightforward interpretation. For instance, inclusion of the 24-nt microexon in the human ortholog of *mef2ca* has been reported to increase its transactivation activity (Zhu, et al. 2005); therefore, an increase in overall expression levels of the isoform without the microexon could conceivably compensate for the deletion of the microexon. Next, we reasoned that, while individual genes may not exhibit strong expression changes, coordinated changes in specific cellular pathways could identify significant patterns shared across multiple microexon deletions. For this purpose, we summed the absolute changes in expression (WT vs Del) for each gene across the 18 microexon deletions and performed a positive Gene Set Enrichment Analysis (GSEA) with these joint differential expression values. This revealed various groups of related GO categories that showed coordinated gene expression changes across the microexon lines (Figure 6C). Remarkably, these categories were highly related to neuronal function and organization (e.g., channels, G-protein coupled receptor activity, synapse, axon, etc.). Many of these categories were also differently expressed in *srrm3* mutant larvae (Figure 6C). Importantly, the same coordinated changes were not observed in all microexon deletions or they did not occur in the same direction (up- or down-regulation)(Figure 6C). This is in line with the patterns observed for neurite growth (e.g. *vav2* and *evi5b*; Figure 3) or for other phenotypic traits (e.g., insulin secretion in beta cells (Juan-Mateu, et al. 2023)), and it suggests that different microexons within the *srrm3*-regulated program may have opposite impacts. Finally, we looked at expression changes in manually curated gene sets of special relevance for neurobiology and/or embryo development, including gene orthologs associated with ASD or schizophrenia, as well as multiple signaling pathways. Some of these sets were widely significantly misregulated across microexon lines, particularly those related to ASD and the synapse (Figure 6D). In summary, while microexon deletions lead to mild changes in expression of individual genes, they often result in significant, coordinated effects on specific neurally related pathways, which may suggest molecular compensation.

DISCUSSION

Despite the major defects observed for the loss-of-function models of their master regulators (Calarco, et al. 2009; Nakano, et al. 2012; Quesnel-Vallières, et al. 2015; Nakano, et al. 2019; Torres-Mendez, et al. 2022), it is still unknown how individual microexons underlie those phenotypes. In this study, we set out to address this question by generating and characterizing 18 microexon deletion zebrafish lines, along with mutant lines of *srrm3* and *srrm4*. To phenotypically characterize these lines, we implemented a battery of tests, aiming at evaluating a wide range of potential neural defects at multiple levels: cellular (neuritogenesis), tissue (gross morphology and axon guidance), behavioral (individual stimuli response, collective interactions) and molecular (transcriptome-wide gene expression patterns). These assays provide a clear picture: while loss of function of the master regulators had strong defects at nearly all levels, particularly for *srrm3* (consistent with (Nakano, et al. 2019; Ciampi, et al. 2022)), all individual microexon deletions were viable and exhibited mild or no detectable alterations in nearly every feature we measured.

These results thus raise a major fundamental question: why do individual microexon deletions lead to such mild phenotypes? There are several potential explanations, most of which are not mutually exclusive. First, the easiest explanation is that most microexons could simply lack any relevant function. However, this is unlikely for the majority of the microexons we have studied, as they are conserved from zebrafish to human, for at least 450 million years of evolution. Moreover, functions at the protein level have been reported for the mammalian orthologs of few of these microexons, including the modulation of protein-protein interactions (*apbb1* (Irimia, et al. 2014), *itsn1* (Dergai, et al. 2010), *src* (Dergai, et al. 2010)), transactivation activity (*mef2ca* (Zhu, et al. 2005)) or motor activity (*kif1b* (Matsushita, et al. 2009)). In addition, we uncovered here a difference in GEF activity between the two isoforms of *vav2*, which are in accordance with the impact of the microexon deletion on neurite growth (Moon and Gomez 2010).

Second, another set of trivial explanations relate to the experimental design, and include that (i) we may not be assessing the traits that these microexons are impacting, (ii) we may not have the sensitivity to robustly measure the magnitude of the changes caused by microexon removal, and/or (iii) the effects may not manifest under optimal laboratory conditions. The latter has been shown to be key, for instance, for embryo growth phenotypes upon *Mbnl3* KO in mouse, which only manifested when the mothers were subjected to calorie restricted diets (Spruce, et al. 2022), or for shadow enhancers in fruit fly, whose effects were only appreciated upon suboptimal temperature conditions (Frankel, et al. 2010).

Third, related to the second point, it is also possible that relatively small perturbations can be compensated for by other molecular changes, particularly under optimal conditions. While this is a very complex hypothesis to test, we have uncovered substantial changes in gene expression in the host gene and/or related paralogs (a classic compensatory mode (El-Brolosy, et al. 2019)), as well as significant coordinated expression changes in gene categories enriched for neural functions. In this scenario, the mild effects of single microexon deletions could be neutralized. In contrast, the global microexon misregulation upon *srrm3/4* mutation would introduce a high number of small changes impacting multiple pathways that could not be properly compensated for altogether, thus causing large phenotypes. Interestingly, it is possible that, despite its many positive aspects as a model organism, zebrafish could be a less suited system to assess the mild phenotypic effects expected for microexon deletions, given the additional whole genome duplication of teleosts compared to most other vertebrates (Amores, et al. 1998). This higher number of paralogs confers zebrafish much higher genetic redundancy compared to mammals, which can be used for potential compensatory changes. Consistent with this idea, various studies have identified robust phenotypes for individual microexon deletions *in vivo* in mouse models (e.g., (Wang, et al. 2015; Gonatopoulos-Pournatzis, et al. 2020; Poliński, et al. 2023)), although publication biases cannot be excluded

(i.e., towards positive results (e.g. see (Matalkah, et al. 2022)) and due to the higher number of mouse vs zebrafish studies).

Finally, relatedly, another potential explanation may reside in the very nature of the molecular role of microexons. Given that they encode for only a few amino acids and they exhibit dramatic cell type specificity, microexon inclusion is expected to contribute to the specialization of a protein for a given context (e.g. the synapse) with respect to the broadly expressed microexon-skipping isoform. In this scenario, both protein isoforms would be partly redundant by definition, as they play equivalent roles but specialized for different contexts, much like two gene paralogs. Therefore, and particularly under optimal conditions, this redundancy is likely to mask the effects of the individual microexon deletions.

Nevertheless, whatever the explanation(s) behind the lack of strong phenotypes observed for most microexon deletions, the exceptional conservation of these exons for hundreds of millions of years can be considered an evolutionary paradox. This case is reminiscent of other highly conserved genomic elements, whose deletions usually lead to viable animals, with little or no alterations, such as the ultraconserved elements (Ahituv, et al. 2007) or some long non-coding RNAs (Goudarzi, et al. 2019). Further research should solve this paradox by providing the missing pieces (i.e., lack of sensitivity or adequate conditions, compensation, redundancy), which will help to better understand the roles and physiological relevance of individual microexons and, more generally, of tissue-specific alternative exon programs.

MATERIALS AND METHODS

Definition of neural-specific alternative exons

Inclusion tables for zebrafish samples were downloaded from *VastDB* (Tapial, et al. 2017) (vastdb.crg.eu). To define neural-enriched exon and microexon programs we parsed these RNA-seq datasets to identify tissue-specific exons using the script *Get_Tissue_Specific_AS.pl* script (Martín, et al. 2021) (https://github.com/vastdb-pastdb/pastdb), requiring the following cut-offs: i) absolute difference in the average exon inclusion level (using the percent-spliced-in metric, PSI) between the target tissue and the averages across other tissues of |ΔPSI| > 15 (*--min_dPSI* 15), ii) global |ΔPSI| > 25, i.e., difference between target tissue inclusion average and the average of all other tissues combined (*--min_dPSI_glob* 25), iii) a valid average PSI value in at least N = 5 tissues (*--N_groups* 5), and iv) sufficient read coverage in at least n = 1 samples per valid tissue group (*--min_rep* 1), i.e., score VLOW or higher as provided by *vast-tools* (Tapial, et al. 2017). A config file with the tissue groups for each RNA-seq sample was provided as input (Table S5). To better capture all microexons with biased inclusion in certain tissue groups, we excluded from the tissues with known or expected partial overlap of microexon inclusion from comparisons in those tissues (for example, neural, endocrine pancreas, muscle and heart), as provided in the column EXCLUDED in the config files. All neural-enriched microexons in zebrafish are provided in Table S1. Human neural microexons were obtained from (Juan-Mateu, et al. 2023), which were defined with similar parameters but *--min_rep* 2.

Functional, evolutionary and regulatory characterization of zebrafish microexons

To visualize the inclusion levels of neural microexons during zebrafish development, inclusion patterns of all microexons across developmental stages (from egg to 7 dpf) were collected from VastDB. GO enrichment analysis for genes harboring zebrafish microexons was performed using the software ClueGO (Bindea, et al. 2009). The gene background set (N = 15,811) consisted of genes containing exons of any kind with the expression level requirements used to define tissue-enriched exons (see above). In particular, they were derived by running the *Get_Tissue_Specific_AS.pl* script with the same parameters used for the tissue-enriched microexon call and requiring sufficient read coverage in neural samples. Exon conservation between zebrafish to human (and vice versa) was assessed as follows. First, we generated gene orthogroups between zebrafish and human by complementing the gene orthologies from *Ensembl* (v80) with those provided in (Ciampi, et al. 2022). We then ran *ExOrthist main* (v1.0.2; (Marquez, et al. 2021)) using the default conservation cutoffs for long evolutionary distances to infer exon orthogroups. In order to increase the sensitivity of the exon orthology calls, we also considered non-annotated exons identified by *vast-tools* (Tapial, et al. 2017) (*--extraexons* option) and we provided pre-computed *liftOver* hits between the two species (computed with the *ExOrthist* companion script *get_liftovers.pl*) to be directly integrated in the exon orthogroups (*--bonafide_pairs* option). Genome conservation was estimated based on the resulting exon orthogroups, while neural-enriched regulatory conservation was assessed based on the ΔPSI values (average PSI in neural samples - average PSI in other tissues) from the *Get_Tissue_Specific_AS.pl* script as described above (using the *--test_tis* option). If the exon had sufficient read coverage, it was considered regulatory conserved if ΔPSI ≥ 15. To evaluate regulation by *srrm3/4* in zebrafish, we obtained the ΔPSI for each exon with sufficient coverage between mutant and control samples for three different pairs of samples: (i) retina from *srrm3* KO or WT 5 dpf larvae (Ciampi, et al. 2022), (ii) retina from *srrm3/4* double KO and *srrm4* KO 5 dpf larvae (Ciampi, et al. 2022), (iii) whole *srrm3/4* double KO and WT 5 dpf larvae (this study, see below). We then selected the lowest ΔPSI value for each exon and plotted their distributions for each exon type (Figure 1E,F). Human data was obtained from (Torres-Méndez, et al. 2019).

Zebrafish husbandry and genotyping

Fish procedures were approved by the Institutional Animal Care and Use Ethic Committee (PRBB–IACUEC). Zebrafish (*Danio rerio*) were grown in the PRBB facility at 28°C 14 h light/10 h dark cycle. All lines generated were reared under standard facility conditions, with the exception of the *srrm3* line, which needed special conditions. These special conditions consisted of water with a salinity of 5 ppm (parts per million) and no renewal of water for 48 hours, which allowed higher survival of rotifers (*Brachionus plicatilis*), and thus kept higher food availability for longer periods of time. This allowed homozygous *srrm3* mutants to feed and survive beyond 12-20 dpf, when they would otherwise die due to issues derived from their impaired vision (Ciampi, et al. 2022). These homozygous *srrm3* mutants grew slowlier and were substantially smaller than their siblings. Therefore, we separated them at ~1 month post-fertilization (mpf) and reared them separately, to avoid competition with their siblings and to be able to closely monitor them.

All zebrafish mutant lines were generated using the Tg(HuC:GFP) line (Park, et al. 2000) as background, kindly provided by Elisa Martí's laboratory at the Institute of Molecular Biology of Barcelona (IBMB). To preserve colony health and maintain genetic diversity, an AB wild-type line was regularly incorporated. Fish were outcrossed with AB individuals every two generations to prevent inbreeding, and HuC:GFP fluorescent embryos were manually selected. For Figure 2E, fish size was measured by determining the standard body length, following the methodology described by (Naslund 2014). For adult fish genotyping or 3-5 dpf larvae, a piece of the caudal fin was cut and disaggregated using 100 uL of NaOH 50mM for 15 minutes at 96°C. To neutralize the reaction, 10uL of 1M Tris-HCl pH=7.4 was added. 2 ul were used as templates for PCR with the pairs of primers designed to amplify the genomic region of interest (Table S4) and using GoTaq® Flexi DNA Polymerase kit (Promega, M7806). PCR products were run on agarose (Invitrogen, 16500500) gels at 2% in TBE.

Individual and massive crosses were carried out in crossing tanks and the resulting eggs were screened for overall health from embryo collection to 5 dpf. Embryos were collected into Petri dishes with E3 medium with methylene blue and placed into the incubator at 28ºC. For each experiment, we used either homozygous (Del) or heterozygous (Het) mutant incrosses, as specified. In the case of the double *srrm3/4* mutant, for which adults were not viable, and given that srrm4 homozygous mutants displayed largely no phenotypes, we used *srrm3+/+,srrm4-/-* as controls, to which we often refer as WTs for simplicity in the different plots. Mutant lines of the regulators were generated in (Ciampi, et al. 2022).

Generation of microexon deletion lines using CRISPR-Cas9

We selected pairs of guide RNAs (gRNAs) to target the 21 selected microexons using CRISPRscan (https://www.crisprscan.org/)(Moreno-Mateos, et al. 2015). The pairs of gRNAs were chosen to be positioned one upstream and one downstream of the microexon region, spanning a maximum of 100 bp from the edges of the microexon. This design aimed to minimize any potential impact on the surrounding intronic regions. Sequences for all gRNAs are provided in Table S3. The gRNA synthesis protocol was adapted from (Gagnon, et al. 2014) and optimized for efficient *in vitro* transcription using MEGAshortscript™ T7 (Thermo Fisher, AM1354). This protocol allows for the transcription of up to 96 sgRNAs in a single well plate. Briefly, the protocol involved annealing oligos to create the template for T7 gRNA transcription, followed by template purification using QIAquick (Qiagen, 28104) and quantification with Qubit dsDNA BR kit (Thermo Q32850). gRNA was synthesized using the MEGAshortscript™ T7 (Thermo, AM1354), purified by precipitation, and finally quantified using the Qubit RNA HS assay (Thermo, Q32852) The final gRNAs were then ready for use for CRISPR-Cas9 injections. Embryos were injected at the 1-2 cell stage with either single or

double gRNAs. Initial single gRNA injections were performed to evaluate the efficiency of individual gRNAs and to enhance the effectiveness of subsequent double gRNA injections for establishing the stable deletion lines. The injection mix contained Cas9 protein (PNABio, CP01-50) at 300 ng/µL, sgRNAs at 50 ng/µL, and Phenol Red solution (Merck, P0290) in sterile Milli-Q water.

gRNA efficiency was validated using a pool of 16 embryos at 48 hours post-injection (hpi) for each injection. DNA extraction was performed using a standard HotSHOT protocol (Samarut, et al. 2016). Fluorescent PCR was performed on genomic DNA, followed by analysis with a Fragment Analysis Service (GeneScan, Thermo) to achieve single-nucleotide resolution of mutations induced by the sgRNAs. GeneScan™ 500 color ROX™ (Thermo, 4310361) was used as a reference size marker. The most effective sgRNAs were selected based on their capacity to produce multiple deletions near the microexon region. Double gRNA validation was performed using standard semi-quantitative PCR.

Validation of microexon inclusion levels in WT and mutant lines

Primers for RT-PCR assays to validate microexon inclusions were taken from VastDB (Tapial, et al. 2017) or designed to span the upstream and downstream exon, optimizing the detection of the two bands for inclusion and exclusion isoforms while avoiding excessive amplification bias of the short isoform (Rukov, et al. 2007). Primer sequences are provided in Table S4. For RNA extraction, embryos or fresh tissues from embryos and adults were homogenized in TRIzol (Thermo, 15696018) using a MiniBeadBeater (Biospec Products) for 40 seconds, along with the addition of glass beads (Merck, G8772-100G). RNA was extracted for event (Figure 1 - figure supplement 1B) and knockout (KO) validations (Figure 2 - figure supplement 1) using TRIzol/chloroform extraction protocol. Final RNA concentrations were quantified using a Qubit Fluorometer with the RNA HS Assay Kit (Invitrogen, Q32855). Total RNA was then reverse transcribed to synthesize cDNA using SuperScript III Reverse Transcriptase (Invitrogen, 18080044), according to the manufacturer's guidelines. cDNA was quantified using Nanodrop and 2 µL of cDNA at 100 ng/µL was used for validation, employing standard PCR conditions with variations similar to those used for genotyping; initial denaturation at 96°C for 3 minutes, followed by 40 cycles of 20 seconds at 96°C, 30 seconds of annealing at 56°C, and a 1-minute elongation at 72°C, concluding with a final elongation step of 5 minutes at 72°C. The resulting PCR products were separated by gel electrophoresis on a 2.5% to 4% ultrapure agarose gel (Invitrogen, 16500500) on SB buffer containing SYBR Safe DNA Gel Stain (Invitrogen, S33102), depending on the size of the products.

Immunofluorescence of Mauthner cells (3A10)

For whole-mount immunostaining of Mauthner cells, incrosses of heterozygous parents from microexon and regulator mutant lines were used. Embryos were initially treated with 0.003% 1-phenyl 2-thiourea (PTU, Sigma-P7629) starting at 20 hpf to inhibit pigment development. At 48 hpf, the embryos were dechorionated and fixed overnight in 4% paraformaldehyde (PFA) at 4°C. The immunostaining protocol began with washing the embryos in 0.2% Triton X-100 in phosphate-buffered saline (PBSTx), followed by a permeabilization step using cold acetone at -20°C for 10 minutes. The samples were then washed again in PBSTx and blocked for 1 hour in a blocking solution consisting of PBSTx and 10% goat serum. Subsequently, the embryos were incubated at 4°C for 24 hours with the primary antibody anti-3A10 (AB_531874, Developmental Studies Hybridoma Bank), a neurofilament marker. After this incubation, the embryos were thoroughly washed in PBSTx before being incubated with the secondary antibody, Alexa goat anti-mouse 594 (1:500, Thermo Fisher Scientific, A-11034). Embryos were then genotyped as described above, and dorsally mounted in low-melting agarose. Imaging was performed using a standard fluorescent microscope (Leica DMI 6000 B), with

images captured using a 20x objective. The evaluation of neural patterning and axon guidance defects was conducted using Fiji-ImageJ, focusing on the observation and quantification of the presence or absence of the two Mauthner cells and their midline crossing in the corpus callosum. A total of 15 to 70 embryos were analyzed for each mutant line from the main founders.

Generation of neuronal primary cultures and quantification of neurite outgrowth

We developed a protocol for isolation, culture and quantification of neurite outgrowth from larval zebrafish neurons. As a general experimental design, we first performed an initial screen, where we used homozygous mutant (Del) incrosses from each main founder, with independent incrosses of Tg(*HuC:GFP*) used as matched control samples for each batch. For those microexons for which significant differences were obtained, we performed additional biological replicates of the main founder and tested the second founder as well. Finally, for the most promising cases (*evi5b* and *vav2*), we generated heterozygous incrosses and grouped sibling larvae by genotype before cell isolation. To assay *srrm3*, *srrm4* and double *srrm3/4* mutants, we followed the same strategy, given that srrm3 and srrm3/4 homozygous mutants were not viable.

Fluorescent activated cell sorting (FACS) of zebrafish neurons

Embryos intended for neuronal cell culture were bleached between 24 and 30 hpf, prior to hatching, to prevent contamination. The bleaching protocol consisted of immersing the embryos in a 0.1% sodium hypochlorite solution for 5 minutes, followed by neutralization in 0.5 µg/L thiosulfate for an additional 5 minutes. Finally, the embryos were transferred to E3 medium containing methylene blue and stored at 28°C. At 48 hpf, the embryos were dechorionated using Pronase (Sigma, 10165921001) at a final concentration of 1 mg/mL in E3 medium. Embryos were gently swirled until the chorion softened, usually within 3 to 5 minutes. They were then transferred to a Petri dish with fresh E3 medium supplemented with 1% penicillin-streptomycin (PNS) to remove any residual Pronase and prevent tissue degradation. Prior to dissociation, embryos were anesthetized by rapid cooling, dechorionated with pronase, and organized into sample groups of 50 embryos per tube, with two biological replicates per condition (control and mutant).

Dissociation was performed under strict sterile conditions. Embryos were immersed in 400 µl of Neurobasal™ medium (NB) and 100 µl of 0.5% trypsin-EDTA. Three rounds of enzymatic and manual dissociation, each lasting 10 minutes, were performed using sterile pestles. After dissociation, samples were centrifuged for 3 minutes at 5,000 revolutions per minute (rpm). The supernatant was removed, and fresh NB medium with supplements (1% P/S, 1% N2, 1% Fungizone, 2% B27, 1x L-glutamine, and 2% fetal bovine serum) was added to stop the trypsinization reaction. The cell suspension was then filtered through a 30 µm cell strainer and kept on ice until sorting. Before sorting, samples were stained with propidium iodide (PI, 1:1000) to assess viability, and then filtered through a 20 µm filter. A high-resolution cytometer (BD Influx™ Cell Sorter) was used to detect Forward scatter (FSC), side scatter (SSC), and fluorescence detection lasers for FITC (488nm), PE-TR-PI were used to gate for live, single, GFP+ cells. Finally, GFP+ cells (ranging from 23-49% of the live population) were sorted and collected in pools of 200,000 cells in 300 µl of NB inside sterile Eppendorf tubes for various downstream applications, including RNA extraction and neuronal cell culture. All data analysis was performed using FlowJo software.

Primary cultures of sorted zebrafish neurons

The culture protocol was developed to be able to obtain a zebrafish neuronal culture from the mutant lines. The method was based on previous studies on culturing zebrafish cell types (Sakowski, et al. 2012; Sassen, et al. 2017). The starting material for the culture development were the isolated neurons obtained through FACS, that were centrifuged for 5 minutes at 5,000 rpm. Pellet cells were resuspended in 300 µL of Neurobasal™ (NB, Thermo, 21103-049) media with supplements (1% Penicillin streptomycin- 1% N2-, 1% Fungizone-, 2% B-27, 1x L-Glutamine-) and plated onto 8-well glass-bottom slides (IBIDI: 80827) coated with 500 µg/mL Poly-D-Lysine (coated for 3-4 hours at 37ºC). Cells were incubated at 28ºC with 5% CO_2. Cells obtained were fixed 15 minutes in 4% Paraformaldehyde (PFA) at different timepoints (4h, 8h, 10h,, 24h, 48h, 72h). Then cells were washed in 1xPBS and stored in 1xPBS supplemented with 0.02% Sodium Azide (Sigma, S2002) to avoid contaminations, for posterior immunostaining and neurite growth studies. Cultured neurons exhibited robust progression in neuronal development and growth (Figure 3 - figure supplement 1), enabling comprehensive study and quantification of neurite length and potential alterations across various genetic backgrounds.

Immunofluorescence of cultured neurons

For the main quantification assays, cells were fixed at 10 and 24 hours after plating (hap) with 4% paraformaldehyde (PFA) for 15 minutes. After fixation, cells were washed three times with 1x PBS and stored at 4°C in 300 µL of 1x PBS containing 0.02% sodium azide to prevent contamination. For immunofluorescence, cells were permeabilized three times for 5 minutes with 0.1% Triton-X100 in 1x PBS with 5% normal goat serum (NGS), followed by a 1-hour block at room temperature (RT) in 0.1% Triton-X100 in 1x PBS with 1% NGS. Primary antibodies were incubated overnight at 4°C in a humidified chamber: mouse anti-acetylated tubulin (1:400, BioLegend, 802001) and rabbit anti-GFP (1:500, Millipore, AB3080P). After incubation, samples were washed three times for 10 minutes in 0.1% Triton-X100 in 1x PBS with 1% NGS, followed by a 2-hour incubation at RT with secondary antibodies: Alexa Fluor 594 goat anti-mouse (1:500, Thermo Fisher, A-11005) and Alexa Fluor 488 goat anti-rabbit (1:500, Thermo Fisher, A-11034). Finally, samples were washed three times with 1x PBS and stained for 1 hour with Hoechst (1:1000, Sigma, B2261) in sterile water for nuclear staining. After staining, samples were stored in 1x PBS with 0.02% sodium azide at 4°C until imaging.

Imaging and analysis neurite length

We used a Leica TCS SP8 inverted confocal microscope to image neuronal culture samples. Neuronal cultures were performed in 8-well chamber slides to enhance imaging efficiency and maintain consistent conditions across all samples. Images were automatically acquired for all wells. For each well, we captured images at 5 randomly selected positions, covering the entire growth surface (1 cm²). Each position was imaged with 15 Z-stacks, with a stack depth of 1 µm per slice. We employed three lasers for imaging: 405 nm for DAPI (nuclei), 488 nm for HuC:GFP, and 594 nm for acetylated tubulin (Ac. Tub). The acquisition parameters included: an image size of 512 x 512 pixels, a scanning speed of 600, bidirectional phase-X correction, a zoom factor of 1.5x, and images were captured using a 20x magnification objective. For each experimental line, we analyzed at least two different wells, with five positions imaged per well. Neurite length was manually quantified using ImageJ, measuring from the tip of the projection to the soma. A total of 100 measurements of neurite length were taken for each well. Statistical differences in the main lines of deleted microexon and regulator were assessed by performing 10,000 bootstrap resampling. This involved randomly selecting 50 data points per experiment per genotype and conducting a Wilcoxon test between control and mutant neurons, or between siblings of different genotypes (Figure 3 - figure supplement 2). When more than one founder was tested, an ANOVA was used to assess differences between genotypes.

SRF promoter activation assay upon *vav2* overexpression in COS cells

To determine VAV2 protein activity, we used a luciferase reporter assay based on SRF promoter activation. In brief, $1x10^6$ exponentially growing COS cells were transfected with 1µg of GFP-VAV2_MIC- (pAA7) or GFP-VAV2_MIC+ (pMCL81) and the firefly luciferase reporter pSRE–Luc (1µg)(Addgene) and the vector constitutively expressing the Renilla luciferase pRL–SV40 (3ng) (Addgene), using Lipofectamine 2000 (Cat. #11668019, Invitrogen). After 48 hours in complete medium, cells were washed in serum–free media and lysed in Passive Lysis Buffer (Cat. #E1960; Promega). The luciferase activity obtained in each condition was recorded using the Dual–Luciferase Reporter System (Cat.#E1960; Promega) according to the supplier's recommendations in a Lumat LB 9507 luminometer (Berthold). The raw values obtained were normalized according to the activity of the Renilla luciferase recorded in each sample. Final values are represented as the fold–change of the normalized luciferase activity obtained when compared to the GFP-VAV2_MIC- sample. In all cases, the abundance of the ectopically expressed proteins under each experimental condition was verified by analyzing aliquots of the cell extracts used in the luciferase experiments by immunoblot.

NanoBRET protein-protein assay between EVI5B and RAB11

Full length zebrafish EVI5B with or without the microexon was cloned into pHTNW and RAB11A into pNLF1W vectors (Yang, et al. 2018) by Gateway LR reaction (Thermo Fisher Scientific) following the manufacturer's indications. HEK293T cells were plated in 24-well plates at a density of 1.4 × 105 cells per well. Cells were transfected with 500 ng of pHTNW-EVI5B, 5 ng of pNLF1W-RAB11A, 0.75 µl of Lipofectamine 3000 and 1 µl of P3000 Reagent (Thermo Fisher Scientific). After 20 h, each transformation was re-plated in four wells of 96-well plates at a density of 1 × 104 cells per well for duplicate control and experimental samples (technical replicates), and protein-protein interactions were analyzed with NanoBRET™ Nano-Glo® Detection System kit (Promega) following manufacturer's instructions. Each transformation experiment was performed at least twice. The corrected NanoBRET ratio was calculated according to the manufacturer's instructions and corrected as previously described (Yang, et al. 2018). NanoBRET signal for EVI5B with or without the microexon co-transfected with or without RAB11A showed strong interaction signal, but similar for both EVI5B isoforms (Figure 3I).

Evaluation of larval activity and response to stimuli using the DanioVision system

Experimental design and procedures

DanioVision experiments were conducted using 5 dpf embryos placed in 48-well plates filled with E3 medium. The experiments were performed blindly, utilizing embryos from heterozygous incrosses of each microexon mutant line, as well as the regulator mutant lines. Animals were randomly assigned to the 48-well plate 1 hour prior to the experimental start to let them habituate to the environment. The experimental protocol in the Danio Vision chamber involved an initial 30 minutes of acclimatization, which included 5 minutes of habituation followed by 25 minutes of baseline activity recording. This was followed by consecutive rounds of dark-light transitions, consisting of three dark and two light phases. Finally, we assessed the startle response of the animals by delivering 30 mechanical tappings at one-second intervals. Video recordings were done at 30 frames per second with a sensitivity detection of 110. For pixel-based measures (activity [% delta pixels]) the moving pixel threshold was adapted to lighting and background (11-16 pixels). After completing the experimental procedures, the animals were collected and genotyped. Dead or unhealthy larvae were excluded from the analysis.

Data export, processing and analysis

Using the EthoVisionXT version 17.0 software, the mean activity data (% delta pixel) was exported in 1 sec intervals. For analysis purposes, technical replicates collected from the same clutch on the same day were combined. Larvae with unclear genotypes were excluded from the downstream analysis. For the computation of activity and visual stimulus transition parameters activity values were averaged by minute. Noisy trials with low video quality or inconsistent stimulus responses of the WT larvae were excluded prior to the analysis. The mean activity (% delta pixel) was subsequently calculated per larva for the baseline (B) period (experimental time 5-30 min), the dark (D) periods (experimental time 30-40 min, 50-60 min, 70-80 min) and the light (L) periods (experimental time 40-50 min, 60-70 min). For the light-dark and dark-light transitions, the difference in activity (% delta pixel) 1 min before and 1 min after the stimulus was obtained for each transition and average across same-type transitions. Differences were computed as follows: light to dark (LD) = activity 1st min dark - activity last min light; dark to light (DL) = activity 1st min light - activity last min dark. For the tapping parameters, larvae not responding to any of the first 3 taps were excluded from downstream analysis as low responders (n = 2 larvae across experiments). The mean activity for each larva at tap number 1 (Act1 tap), 3-5 and 21-30 was obtained. To measure a drop in responsiveness the mean activity of both, tapping 3-5 and tapping 21-30 was subtracted from *Act1 tap* to obtain *Diff 3to5 vs 1 tap* and *Diff 21to30 vs 1 tap* respectively. For the thigmotaxis parameters, arenas were split into center and periphery (38.5 mm^2 each), activity (% delta pixel) and total distance moved (TDM) (mm) were exported by minute and arena (periphery and center) using EthoVisionXT. To exclude larvae with suboptimal positional tracking activity (pixel-based) and TDM (tracking-based) were correlated and larvae with a pearson-correlation of $r < 0.9$ were removed. Larvae with little movement (activity = 0 for < 3 min per condition) were also excluded. Trials with < 3 larvae in any genotype were removed. Median thigmotaxis values per larvae was computed as TDM (mm) in the periphery divided by the sum of TDM (mm) in the center and periphery, multiplied by 100, for the time intervals of B, D and L only considering minutes of movement only (activity > 0).

Evaluation of social interactions in juvenile fish

Implementation of a custom behavioral system

The behavioral setup developed in the lab was based on (Hinz and de Polavieja 2017), developed by the Polavieja lab. It consisted of a custom-made, circular transparent tank with a diameter of 42 cm, filled with 4 L of system water (Figure 5 - figure supplement 1). This experimental arena was placed in the center of an opaque acrylic sheet held within a larger external tank measuring 80 x 60 x 20 cm, which contained 90 L of system water. To maintain a consistent water temperature of 28ºC, two water heaters were placed diagonally opposite each other in the external tank. The entire setup was housed in a 1.2 m² box with white walls. Uniform illumination was crucial, so LEDs were installed around the inside of the box. A hand-sewn curtain was used as a light diffuser, covering the diameter of the experimental arena to prevent reflections. The overall light intensity reached 2000 Lux. Videos were recorded from above using a 12.36 MP UI-3000SE monochrome camera with a 16-mm Tamron lens. The camera was mounted on an adjustable arm, positioned 100 cm above the center of the tank. Video recordings were conducted using Stream-Pix 7 software, running on a high-performance computer equipped with an Nvidia GeForce GTX 1070-8G graphics card for data acquisition and post-processing.

Experimental design and procedures

We used juvenile zebrafish at approximately 30 dpf, conducting experiments over two consecutive days for each microexon mutant line to ensure a representative sample size. Due to the slower growth rate of the homozygous *srrm3* mutant fish, they were studied at 3 mpf, when their body length matched that of 30 dpf wild-type zebrafish. Sex was not considered, as it is undetermined at this stage. All experiments were conducted between 8:00 AM and 4:00 PM. We used homozygous × heterozygous crosses to simplify the design and avoid an excessive number of genotype combinations. Each experiment was performed blind to fish pairs, and animals were fin-clipped and genotyped post-experiment. On the day of the experiment, fish tanks were placed in the experimental box for 1 hour to acclimate the animals. The experimental protocol had the following steps (Figure 5A): (i) selecting a random pair of fish and introducing them to the arena, (ii) allowing a 2-minute habituation, (iii) recording free movement for 10 minutes, (iv) removing fish 1, (v) removing fish 2 one minute later, (vi) anesthetizing, (vii) genotyping. After removal, fish were placed in a 1 L fish water tank with 30 mL of tricaine (4mg/mL, Sigma-E10521) for fin clipping, a critical step for matching each fish to its experimental ID, preventing misidentification. Videos were recorded at 30 frames per second (fps) using Stream-Pix 7, with manual image adjustments.

Video tracking with idtracker.ai

After video acquisition, the recordings were compressed using FFmpeg (version 8), an open-source multimedia framework. This reduced the file size while maintaining acceptable visual quality. The compressed files were successfully validated by tracking them alongside the uncompressed versions to ensure they met the required quality for further analysis. We used idtracker.ai (Romero-Ferrero, et al. 2019) to track animals and extract the trajectories of the fish in each video. These trajectories form the basis for analyzing animal behavior and interactions parameters. Before running the tracking, specific parameters were adjusted individually for each video using the graphical user interface (GUI) of idtracker.ai to ensure proper identification of the fish. The key parameters were: (i) Region of Interest (ROI): adjusted to match the perimeter of the arena (Figure 5 - figure supplement 1), (ii) Time intervals: first interval set to 10 minutes (18,000 frames) + second interval of variable time for fish identification, (iii) Pixel intensity: used to differentiate fish from the background, ranging from 0–255, (iv) Area threshold: defined between 0–6000 to identify individual fish blobs by filtering based on size (and excluding other objects of different sizes), allowing for better distinction from pixel intensity variations. (v) Number of blobs: set to 2 (one for each fish in the pair). After setting these parameters, all videos were tracked, and tracking performance was evaluated based on the estimated accuracy, which measures the proportion of correctly identified fish. An accuracy threshold of 0.98 was applied, allowing for up to 2% misidentification. Videos falling below this accuracy threshold were excluded from further analysis.

Data processing and statistical analysis

For data processing, we customized the Python-based *trajectorytools* package (https://github.com/fjhheras/trajectorytools) to better suit our needs (https://github.com/vastgroup/mic-social-behavior-analysis). First, we included "Genotype" (Heterozygous or Homozygous) and "Pair" (Het-Het, Het-Del, Del-Del) as key variables for statistical comparisons. Next, we developed an automated system to associate each fish with its experimental ID and correlate it with the tracking ID. We leveraged the video's second interval, which captures the removal of the two fish, to define the experimental ID for genotyping. By checking for the presence or absence of trajectories in this interval, we matched each fish to its corresponding trajectory and ID number. We used *trajectorytools* to import the trajectories generated by idtracker.ai and to compute the following variables from the fish trajectories: (i) Speed: rate at which an individual fish or group of fish moves through their environment measured in cm/s. (ii) Absolute normal acceleration (*Abs. N. Accel): absolute value of the* acceleration vector component that is directly perpendicular to the fish's current direction of movement. This component of the acceleration is associated with changes in

direction (turning) and is measured in cm/s². (iii) Absolute tangential acceleration *(Abs. Tg. Accel):* absolute value of the acceleration vector that is parallel to the fish's current direction of movement. It represents how fast the zebrafish is speeding up or slowing down without changing direction (associated scape response and group cohesion) measured in cm/s². (iv) Distance traveled*:* distance traveled (cm). (v) Time in the periphery: Total number of frames that a fish was found in the periphery (border) of the arena. We defined the periphery as the ring defined from 0.8*R to the border, where R is the radius of the arena. (vi) Normalized distance to origin: Normalized distance to the center of the arena being 0 = center and 1 = border (walls). (vii) Ratio in front: The proportion of time that a fish has another fish in front. From a focal fish perspective, lower values are associated with higher leadership. (viii) Polarization: measure of how aligned the zebrafish are in terms of their movement direction. When polarization is low individuals are moving in random directions. When polarization is high most individuals in the group are moving in the same or similar directions. Unitless, range 0-1. (ix) Distance to neighbor: distance between the two fish measured in cm.

Measures i-vii corresponded to individual fish measures within a pair, while measures viii and ix are pair-specific. For statistical analyses, for the individual measures, we split them by genotype (heterozygous [Het] or homozygous [Del]) and according to the pair in which they were tested (homotypic Het-Het or Del-Del [same, S], heterotypic Het-Del [different, D]). For measures i-vi, a single value for each S pair was collected (the average of the two fish), to avoid double counting of nearly identical measures. For group features, we split them by pair type and compared Het-Het pairs against either Het-Del or Del-Del. For all comparisons two-sided Wilcoxon Rank-Sum tests were used to assess statistical significant differences.

Considerations regarding statistical analyses

Given the complex and diverse structure of the data in Figures 3, 4 and 5, as well as the associated supplemental figures, we took the following approaches. When a varying number of biological replicates of the same founder were present (e.g., Figure 3C,4B), we performed a permutation-based test to obtain the median of the p-value distribution of bootstrap resampling Wilcoxon tests. When the two founders were tested together (e.g., Figure 3D), we used ANOVA tests to assess the significance of genotype. Finally, for direct comparisons between the distributions of specific features between WT and Het/Del, we used two-sided Wilcoxon Rank-Sum tests (Figures 4 and 5 and boxplots in the associated supplementary figures). Importantly, given the large amount of tests performed in those figures, and given that defining the level to which to apply the multiple testing correction (microexon, feature, figure, etc.) would be to a large extent arbitrary, we opted for reporting the nominal p-value and use this value not as a hard cut-off, but as a way to help identify and highlight potentially meaningful biological effects, along with the effect size of the difference and the consistency across replicates and founders (when available).

Generation of RNA sequencing and transcriptomic analysis

To assess transcriptome-wide changes in gene expression, we generated RNA-seq for WT and Del 5 dpf larvae for all 18 microexon main founder lines, as well as 5 secondary ones (Table S6). In addition, we generated two biological replicates of *srrm3* WT and Del 5 dpf larvae. To produce these data, incrosses of heterozygous parents were set for each line, and larvae were genotyped by fin clipping (see above) at 5 dpf. Between 10-12 larvae of either WT or Del were pooled for each line and RNA was extracted using the RNeasy Mini Kit (Qiagen, 74134), following the manufacturer's instructions. Final RNA concentrations were quantified using a Qubit Fluorometer with the RNA HS Assay Kit (Invitrogen, Q32855). PolyA+ stranded libraries for RNA sequencing were generated at the CRG Genomics Unit, and sequenced in an Illumina HiSeq2500 machine to produce an average of 42.5 million 50-nt single end reads

(Table S6). For samples of the regulator mutants, 72.8 million 125-nt paired end reads were generated to allow for alternative splicing analyses. All RNA-seq samples were submitted to Gene Expression Omnibus (GEO), identifier: GSE278690.

RNA-seq data was mapped with STAR (Dobin, et al. 2013) to the *Danio rerio* genome version danRer10 (Ensembl v91). Mappings were used for correcting bias due to the heterogeneous patterns of transcript degradation with the Bioconductor package named *DegNorm* (Xiong, et al. 2019) using the gene annotations from Ensembl v91. Gene read counts were then normalized with the variance stabilizing transformation (VST) from DESeq2 (Love, et al. 2014). Additionally, batch variation was removed using the Empirical Bayes-moderate adjustment for unwanted covariates from the R package WGCNA fitting WT samples (Figure 6 - figure supplement 1). Differences between Del and WT samples were obtained from the subtraction of these values from each genotype after all corrections and normalizations. Gene Set Enrichment Analyses (GSEA) were performed with the R-package *fgsea* using *idep* (Ge, et al. 2018) and *shinyGO* (Ge, et al. 2020) GO annotations. To select globally enriched GO categories across microexon deletion lines, we first sum the absolute differences between Del and WT across all main founders and performed a positive GSEA test. Jaccard distance was then calculated between enriched GOs (adjusted p-value <0.01) and used for a complete hierarchical clustering, and tree cutting at a 0.9 height (<10% shared genes between clustered GOs). Clusters with at least one term with a p-value < 0.001 were filtered and named after the most significant term in it. Additionally, for each individual microexon deletion comparison, a GSEA was estimated for GOs enriched globally and merged cluster categories (Figure 6C, right plot). Finally, we selected various gene sets of interest to investigate their differential expression patterns among microexon deletions using GSEA (Figure 6D). These gene sets (Table S7) were obtained as follows: (i) ASD genes: zebrafish orthologs of SFARI category 1 and 2 genes [April 2020]; (ii) Schizophrenia genes: from (Thyme, et al. 2019); (iii) Immediate early genes: zebrafish orthologs of genes reported in (Piwecka, et al. 2017); (iv) Developmental pathways: from (Marlétaz, et al. 2018).

AUTHOR CONTRIBUTIONS

Conceptualization: MI, LLB, FM. Resources: MI, GGP, XRB. Data curation: LLB, CRM, TM, FM, LPI, FRF. Software: FRF, LPI. Formal analysis: LLB, TM, FM, LPI, FRF, MC. Funding acquisition: MI, GGP, XRB. Validation: CR, JP. Investigation: LLB, CRM, FM, LPI, JP, EMK, TM, MCT, JFA, MC. Visualization: FM, LPI, MI. Methodology: LLB, CRM, EMK, JFA. Writing - original draft: MI. Project administration: MI. Writing – review and editing: all authors.

ACKNOWLEDGEMENTS

This project has received funding from the European Research Council (ERC) under the European Union's Horizon 2020 research and innovation programme (grant agreements No 637591 and No 101002275, both to MI) and the Spanish Ministry of Science, Innovation and Universities through the State Investigation Agency (PID2020-115040GB-I00 / AEI / 10.13039/501100011033 to MI). CRG acknowledges support of the Spanish Ministry of Science and Innovation through the Centro de Excelencia Severo Ochoa (CEX2020-001049-S, MCIN/AEI/10.13039/501100011033), and the Generalitat de Catalunya through the CERCA program. GP and FRF were funded by Champalimaud Foundation and the FCT (PTDC/BIA-COM/5770/2020). RNA-seq samples were generated at the CRG Genomics Unit and NanoBRET assays at the CRG Protein Technologies Unit, both part of the CRG Core Technologies Programme.

REFERENCES

Ahituv N, Zhu Y, Visel A, Holt A, Afzal V, Pennacchio LA, Rubin EM. 2007. Deletion of ultraconserved elements yields viable mice. PLoS Biol 5:e234.

Amores A, Force A, Yan YL, Joly L, Amemiya C, Fritz A, Ho RK, Langeland J, Prince V, Wang YL, et al. 1998. Zebrafish hox clusters and vertebrate genome evolution. Science 282:1711-1714.

Bebee TW, Park JW, Sheridan KI, Warzecha CC, Cieply BW, Rohacek AM, Xing Y, Carstens RP. 2015. The splicing regulators Esrp1 and Esrp2 direct an epithelial splicing program essential for mammalian development. Elife 4:doi: 10.7554/eLife.08954.

Bindea G, Mlecnik B, Hackl H, Charoentong P, Tosolini M, Kirilovsky A, Fridman WH, Pages F, Trajanoski Z, Galon J. 2009. ClueGO: a Cytoscape plug-in to decipher functionally grouped gene ontology and pathway annotation networks. Bioinformatics 25:1091-1093.

Bodmer D, Ascano M, Kuruvilla R. 2011. Isoform-specific dephosphorylation of dynamin1 by calcineurin couples neurotrophin receptor endocytosis to axonal growth. Neuron 70:1085-1099.

Burguera D, Marquez Y, Racioppi C, Permanyer J, Torres-Mendez A, Esposito R, Albuixech-Crespo B, Fanlo L, D'Agostino Y, Gohr A, et al. 2017. Evolutionary recruitment of flexible Esrp-dependent splicing programs into diverse embryonic morphogenetic processes. Nat Commun 8:1799.

Calarco JA, Superina S, O'Hanlon D, Gabut M, Raj B, Pan Q, Skalska U, Clarke L, Gelinas D, van der Kooy D, et al. 2009. Regulation of vertebrate nervous system alternative splicing and development by an SR-related protein. Cell 138:898-910.

Ciampi L, Mantica F, Lopez-Blanch L, Permanyer J, Rodriguez-Marin C, Zang J, Cianferoni D, Jimenez-Delgado S, Bonnal S, Miravet-Verde S, et al. 2022. Specialization of the photoreceptor transcriptome by Srrm3-dependent microexons is required for outer segment maintenance and vision. Proc Natl Acad Sci U S A 119:e2117090119.

Dergai M, Tsyba L, Dergai O, Zlatskii I, Skrypkina I, Kovalenko V, Rynditch A. 2010. Microexon-based regulation of ITSN1 and Src SH3 domains specificity relies on introduction of charged amino acids into the interaction interface. Biochem Biophys Res Commun 399:307-312.

Dobin A, Davis CA, Schlesinger F, Drenkow J, Zaleski C, Jha S, Batut P, Chaisson M, Gingeras TR. 2013. STAR: ultrafast universal RNA-seq aligner. Bioinformatics 29:15-21.

El-Brolosy MA, Kontarakis Z, Rossi A, Kuenne C, Gunther S, Fukuda N, Kikhi K, Boezio GLM, Takacs CM, Lai SL, et al. 2019. Genetic compensation triggered by mutant mRNA degradation. Nature 568:193-197.

Ellis JD, Barrios-Rodiles M, Colak R, Irimia M, Kim T, Calarco JA, Wang X, Pan Q, O'Hanlon D, Kim PM, et al. 2012. Tissue-specific alternative splicing remodels protein-protein interaction networks. Mol Cell 46:884-892.

Eva R, Dassie E, Caswell PT, Dick G, ffrench-Constant C, Norman JC, Fawcett JW. 2010. Rab11 and its effector Rab coupling protein contribute to the trafficking of beta 1 integrins during axon growth in adult dorsal root ganglion neurons and PC12 cells. J Neurosci 30:11654-11669.

Faitar SL, Dabbeekeh JT, Ranalli TA, Cowell JK. 2005. EVI5 is a novel centrosomal protein that binds to alpha- and gamma-tubulin. Genomics 86:594-605.

Frankel N, Davis GK, Vargas D, Wang S, Payre F, Stern DL. 2010. Phenotypic robustness conferred by apparently redundant transcriptional enhancers. Nature 466:490-493.

Gagnon JA, Valen E, Thyme SB, Huang P, Akhmetova L, Pauli A, Montague TG, Zimmerman S, Richter C, Schier AF. 2014. Efficient mutagenesis by Cas9 protein-mediated oligonucleotide insertion and large-scale assessment of single-guide RNAs. PLoS One 9:e98186.

Ge SX, Jung D, Yao R. 2020. ShinyGO: a graphical gene-set enrichment tool for animals and plants. Bioinformatics 36:2628-2629.

Ge SX, Son EW, Yao R. 2018. iDEP: an integrated web application for differential expression and pathway analysis of RNA-Seq data. BMC Bioinformatics 19:534.

Gonatopoulos-Pournatzis T, Niibori R, Salter EW, Weatheritt RJ, Tsang B, Farhangmehr S, Liang X, Braunschweig U, Roth J, Zhang S, et al. 2020. Autism-Misregulated eIF4G Microexons Control Synaptic Translation and Higher Order Cognitive Functions. Mol Cell 7:1176-1192.e1116.

Goudarzi M, Berg K, Pieper LM, Schier AF. 2019. Individual long non-coding RNAs have no overt functions in zebrafish embryogenesis, viability and fertility. Elife 8.

Hinz RC, de Polavieja GG. 2017. Ontogeny of collective behavior reveals a simple attraction rule. Proc Natl Acad Sci U S A 114:2295-2300.

Irimia M, Rukov JL, Roy SW, Vinther J, Garcia-Fernandez J. 2009. Quantitative regulation of alternative splicing in evolution and development. Bioessays 31:40-50.

Irimia M, Weatheritt RJ, Ellis J, Parikshak NN, Gonatopoulos-Pournatzis T, Babor M, Quesnel-Vallières M, Tapial J, Raj B, O'Hanlon D, et al. 2014. A highly conserved program of neuronal microexons is misregulated in autistic brains. Cell 159:1511-1523.

Jacob J, Haspel J, Kane-Goldsmith N, Grumet M. 2002. L1 mediated homophilic binding and neurite outgrowth are modulated by alternative splicing of exon 2. J Neurobiol 51:177-189.

Juan-Mateu J, Bajew S, Miret-Cuesta M, Íñiguez LP, López-Pascual A, Bonnal S, Atla G, Bonàs-Guarch S, Ferrer J, Valcárcel J, et al. 2023. Pancreatic microexons regulate islet function and glucose homeostasis. Nat Metab 5:219-236.

Kjer-Hansen P, Weatheritt RJ. 2023. The function of alternative splicing in the proteome: rewiring protein interactomes to put old functions into new contexts. Nat Struct Mol Biol 30:1844-1856.

Li YI, Sanchez-Pulido L, Haerty W, Ponting CP. 2015. RBFOX and PTBP1 proteins regulate the alternative splicing of micro-exons in human brain transcripts. Genome Res 25:1-13.

Love MI, Huber W, Anders S. 2014. Moderated Estimation of Fold Change and Dispersion for RNA-Seq Data with DESeq2. Genome Biol 15:550.

Marlétaz F, Firbas PN, Maeso I, Tena JJ, Bogdanovic O, Perry M, Wyatt CD, de la Calle-Mustienes E, Bertrand S, Burguera D, et al. 2018. Amphioxus functional genomics and the origins of vertebrate gene regulation. Nature 564:64-70.

Marquez Y, Mantica F, Cozzuto L, Burguera D, Hermoso-Pulido A, Ponomarenko J, Roy SW, Irimia M. 2021. ExOrthist: a tool to infer exon orthologies at any evolutionary distance. Genome Biol 22:239.

Martín G, Márquez Y, Mantica F, Duque P, Irimia M. 2021. Alternative splicing landscapes in Arabidopsis thaliana across tissues and stress conditions highlight major functional differences with animals. Genome Biol 22:35.

Matalkah F, Jeong B, Sheridan M, Horstick E, Ramamurthy V, Stoilov P. 2022. The Musashi proteins direct post-transcriptional control of protein expression and alternate exon splicing in vertebrate photoreceptors. Commun Biol 5:1011.

Matsushita M, Yamamoto R, Mitsui K, Kanazawa H. 2009. Altered motor activity of alternative splice variants of the mammalian kinesin-3 protein KIF1B. 2009 10:1647-1654.

Moon MS, Gomez TM. 2010. Balanced Vav2 GEF activity regulates neurite outgrowth and branching in vitro and in vivo. Mol Cell Neurosci 44:118-128.

Moreno-Mateos MA, Vejnar CE, Beaudoin JD, Fernandez JP, Mis EK, Khokha MK, Giraldez AJ. 2015. CRISPRscan: designing highly efficient sgRNAs for CRISPR-Cas9 targeting in vivo. Nature Methods 12:982-988.

Nakano Y, Jahan I, Bonde G, Sun X, Hildebrand MS, Engelhardt JF, Smith RJ, Cornell RA, Fritzsch B, Bánfi B. 2012. A mutation in the Srrm4 gene causes alternative splicing defects and deafness in the Bronx waltzer mouse. PLoS Genet 8:e1002966.

Nakano Y, Wiechert S, Bánfi B. 2019. Overlapping Activities of Two Neuronal Splicing Factors Switch the GABA Effect from Excitatory to Inhibitory by Regulating REST. Cell Rep 27:860-871.

Naslund J. 2014. A simple non-invasive method for measuring gross brain size in small live fish with semi-transparent heads. PeerJ 2:e586.

Ohnishi T, Shirane M, Hashimoto Y, Saita S, Nakayama KI. 2014. Identification and characterization of a neuron-specific isoform of protrudin. Genes Cells 19:97-111.

Ohnishi T, Shirane M, Nakayama KI. 2017. SRRM4-dependent neuron-specific alternative splicing of protrudin transcripts regulates neurite outgrowth. Sci Rep 7:41130.

Pan Q, Shai O, Lee LJ, Frey BJ, Blencowe BJ. 2008. Deep surveying of alternative splicing complexity in the human transcriptome by high-throughput sequencing. Nat Genet 40:1413-1415.

Park HC, Kim CH, Bae YK, Yeo SY, Kim SH, Hong SK, Shin J, Yoo KW, Hibi M, Hirano T, et al. 2000. Analysis of upstream elements in the HuC promoter leads to the establishment of transgenic zebrafish with fluorescent neurons. Dev Biol 227:279-293.

Parras A, Anta H, Santos-Galindo M, Swarup V, Elorza A, Nieto-Gonz?lez JL, Pico S, Hernandez IH, Diaz-Hernandez JI, Belloc E, et al. 2018. Autism-like phenotype and risk gene mRNA deadenylation by CPEB4 mis-splicing. Nature 560:441-446.

Piwecka M, Glazar P, Hernandez-Miranda LR, Memczak S, Wolf SA, Rybak-Wolf A, Filipchyk A, Klironomos F, Cerda Jara CA, Fenske P, et al. 2017. Loss of a mammalian circular RNA locus causes miRNA deregulation and affects brain function. Science 357.

Poliński P, Cuesta MM, Zamora-Moratalla A, Mantica F, Cantero-Recasens G, Normanno D, Rabago LI, Morenilla-Palao C, Ordoño P, Bonnal S, et al. 2023. A novel regulatory mechanism of actin cytoskeleton dynamics through a neural microexon in DAAM1 is important for proper memory formation. bioRxiv:2023.2001.2012.523772.

Quesnel-Vallieres M, Dargaei Z, Irimia M, Gonatopoulos-Pournatzis T, Ip J, Wu M, Sterne-Weiler T, Nakagawa S, Woodin MA, Blencowe BJ, et al. 2016. Misregulation of an Activity-Dependent Splicing Network as a Common Mechanism Underlying Autism Spectrum Disorders. Mol Cell 64:1023-1034.

Quesnel-Vallières M, Irimia M, Cordes SP, Blencowe BJ. 2015. Essential roles for the splicing regulator nSR100/SRRM4 during nervous system development. Genes Dev 29:746-759.

Romero-Ferrero F, Bergomi MG, Hinz RC, Heras FJH, de Polavieja GG. 2019. idtracker.ai: tracking all individuals in small or large collectives of unmarked animals. Nat Methods 16:179-182.

Roth JF, Braunschweig U, Wu M, Li JD, Lin ZY, Larsen B, Weatheritt RJ, Gingras AC, Blencowe BJ. 2023. Systematic analysis of alternative exon-dependent interactome remodeling reveals multitasking functions of gene regulatory factors. Mol Cell 83:4222-4238 e4210.

Rukov JL, Irimia M, Mork S, Lund VK, Vinther J, Arctander P. 2007. High Qualitative and Quantitative Conservation of Alternative Splicing in Caenorhabditis elegans and Caenorhabditis briggsae. Mol Biol Evol 24:909-917.

Sakowski SA, Lunn JS, Busta AS, Palmer M, Dowling JJ, Feldman EL. 2012. A novel approach to study motor neurons from zebrafish embryos and larvae in culture. J Neurosci Methods. 205:277-282.

Samarut E, Lissouba A, Drapeau P. 2016. A simplified method for identifying early CRISPR-induced indels in zebrafish embryos using High Resolution Melting analysis. BMC Genomics 17:547.

Sassen WA, Lehne F, Russo G, Wargenau S, Dubel S, Koster RW. 2017. Embryonic zebrafish primary cell culture for transfection and live cellular and subcellular imaging. Dev Biol 430:18-31.

Spruce T, Plass M, Gohr A, Ray D, Martinez de Lagran M, Rot G, Novoa A, Burguera D, Permanyer J, Miret M, et al. 2022. The X-linked splicing regulator MBNL3 has been co-opted to restrict placental growth in eutherians. PLoS Biol 20:e3001615.

Tapial J, Ha KCH, Sterne-Weiler T, Gohr A, Braunschweig U, Hermoso-Pulido A, Quesnel-Vallières M, Permanyer J, Sodaei R, Marquez Y, et al. 2017. An atlas of alternative splicing profiles and functional associations reveals new regulatory programs and genes that simultaneously express multiple major isoforms. Genome Res 27:1759-1768.

Thyme SB, Pieper LM, Li EH, Pandey S, Wang Y, Morris NS, Sha C, Choi JW, Herrera KJ, Soucy ER, et al. 2019. Phenotypic Landscape of Schizophrenia-Associated Genes Defines Candidates and Their Shared Functions. Cell 177:478-491 e420.

Torres-Méndez A, Bonnal S, Marquez Y, Roth J, Iglesias M, Permanyer J, Almudí I, O'Hanlon D, Guitart T, Soller M, et al. 2019. A novel protein domain in an ancestral splicing factor drove the evolution of neural microexons. Nature Ecol Evol 3:691-701.

Torres-Mendez A, Pop S, Bonnal S, Almudi I, Avola A, Roberts RJV, Paolantoni C, Alcaina-Caro A, Martin-Anduaga A, Haussmann IU, et al. 2022. Parallel evolution of a splicing program controlling neuronal excitability in flies and mammals. Sci Adv 8:eabk0445.

Wang ET, Sandberg R, Luo S, Khrebtukova I, Zhang L, Mayr C, Kingsmore SF, Schroth GP, Burge CB. 2008. Alternative isoform regulation in human tissue transcriptomes. Nature 456:470-476.

Wang J, Telese F, Tan Y, Li W, Jin C, He X, Basnet H, Ma Q, Merkurjev D, Zhu X, et al. 2015. LSD1n is an H4K20 demethylase regulating memory formation via transcriptional elongation control. Nat Neurosci 18:1256-1264.

Worley TL, Cornel E, Holt CE. 1997. Overexpression of c-src and n-src in the developing Xenopus retina differentially impairs axonogenesis. Mol Cell Neurosci 9:276-292.

Xiong B, Yang Y, Fineis FR, Wang JP. 2019. DegNorm: normalization of generalized transcript degradation improves accuracy in RNA-seq analysis. Genome Biol 20:75.

Yang JS, Garriga-Canut M, Link N, Carolis C, Broadbent K, Beltran-Sastre V, Serrano L, Maurer SP. 2018. rec-YnH enables simultaneous many-by-many detection of direct protein-protein and protein-RNA interactions. Nat Commun 9:3747.

Zhu B, Ramachandran B, Gulick T. 2005. Alternative pre-mRNA splicing governs expression of a conserved acidic transactivation domain in myocyte enhancer factor 2 factors of striated muscle and brain. J Biol Chem 280:28749-28760.

Zibetti C, Adamo A, Binda C, Forneris F, Toffolo E, Verpelli C, Ginelli E, Mattevi A, Sala C, Battaglioli E. 2010. Alternative splicing of the histone demethylase LSD1/KDM1 contributes to the modulation of neurite morphogenesis in the mammalian nervous system. J Neurosci 30:2521-2532.

SUPPLEMENTARY TABLES

Table S1 - Neural exons and microexons in zebrafish.

Table S2 - Selected microexons for phenotypic characterization and associated regulatory data.

Table S3 - Sequence of guide RNAs used to generate microexon deletion lines.

Table S4 - Primers for genotyping and for mRNA validation of microexon inclusion.

Table S5 - Config file used for the *Get_Tissue_Specific_AS.pl* script.

Table S6 - RNA-seq samples generated in this study.

Table S7 - Gene sets of special interest used in this study.

SUPPLEMENTARY VIDEOS

Video S1 - Behavior of adult *srrm3* mutants.
https://www.dropbox.com/scl/fi/nz5k8lsk6mozmexr4ulfs/Video_S1.m4v?rlkey=vj1p60nr1ie3uajre1zbysbfe&dl=0

Video S2 - Group of five *srrm3* mutant juvenile fish
https://www.dropbox.com/scl/fi/eex0y01suqrk2sbipi9t3/Video_S2.mp4?rlkey=gwt8fe4tah5pndjzjo404uk4v&dl=0

Video S3 - Group of five WT juvenile fish
https://www.dropbox.com/scl/fi/0bsi35ulmq5n1oufz7l1i/Video_S3.mp4?rlkey=b9xwud2uzgyl4bwuesibgdvwe&dl=0

MAIN FIGURES

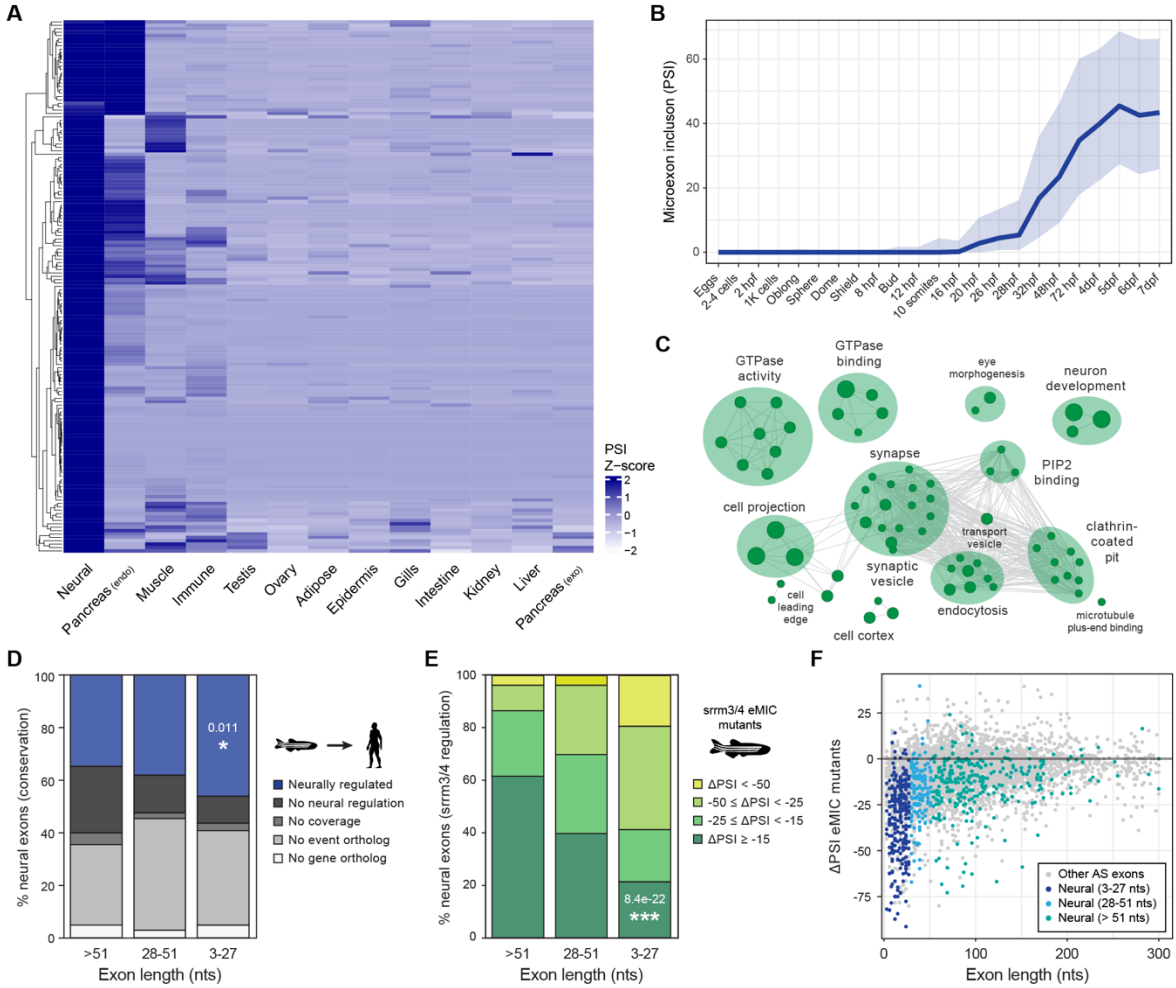

Figure 1: Neural microexon program in zebrafish. A) Heatmap showing relative inclusion levels of neural microexons identified in zebrafish (Table S1). The value for each tissue type corresponds to the average inclusion in the samples for that tissue in *VastDB* (Table S1). Only events with sufficient read coverage in >10 tissue groups are plotted (N = 157) and missing values were imputed. **B)** Inclusion of neural microexons along embryo development (egg to 7 days post-fertilization [dpf]). Thick line corresponds to the median PSI and the shades to the first and third quartile of the PSI distribution. **C)** Enriched Gene Ontology (GO) categories among genes harboring neural microexons in zebrafish. GO terms were grouped into networks by ClueGO. **D)** Evolutionary conservation of zebrafish neural exons of different length group at the genomic and tissue-regulatory level compared with human. Exons conserved at the regulatory level (blue) are those with enriched inclusion in neural samples (ΔPSI ≥ 15) also in human. Those with no neural regulation (black) are conserved at the genomic level (Irimia, et al. 2009), but are not neurally enriched. Those conserved but with insufficient coverage to assess regulation are indicated as "No coverage" (dark grey). P-value corresponds to a two-sided Fisher's Exact test for neural conservation vs. others between exons > 51 nts and 3-27 nts. **E)** Distribution of exons of different length by the level of *srrm3/4* misregulation in larva or retina (see Methods). P-value corresponds to a two-sided Fisher's Exact test for non-regulated exons (ΔPSI ≥ -15) vs. others between exons > 51 nts and 3-27 nts. **F)** Change in inclusion levels [ΔPSI (eMIC mutant-WT)] for all exons shorter than 300 bp. Dots with different blue colors correspond to neural exons of different length.

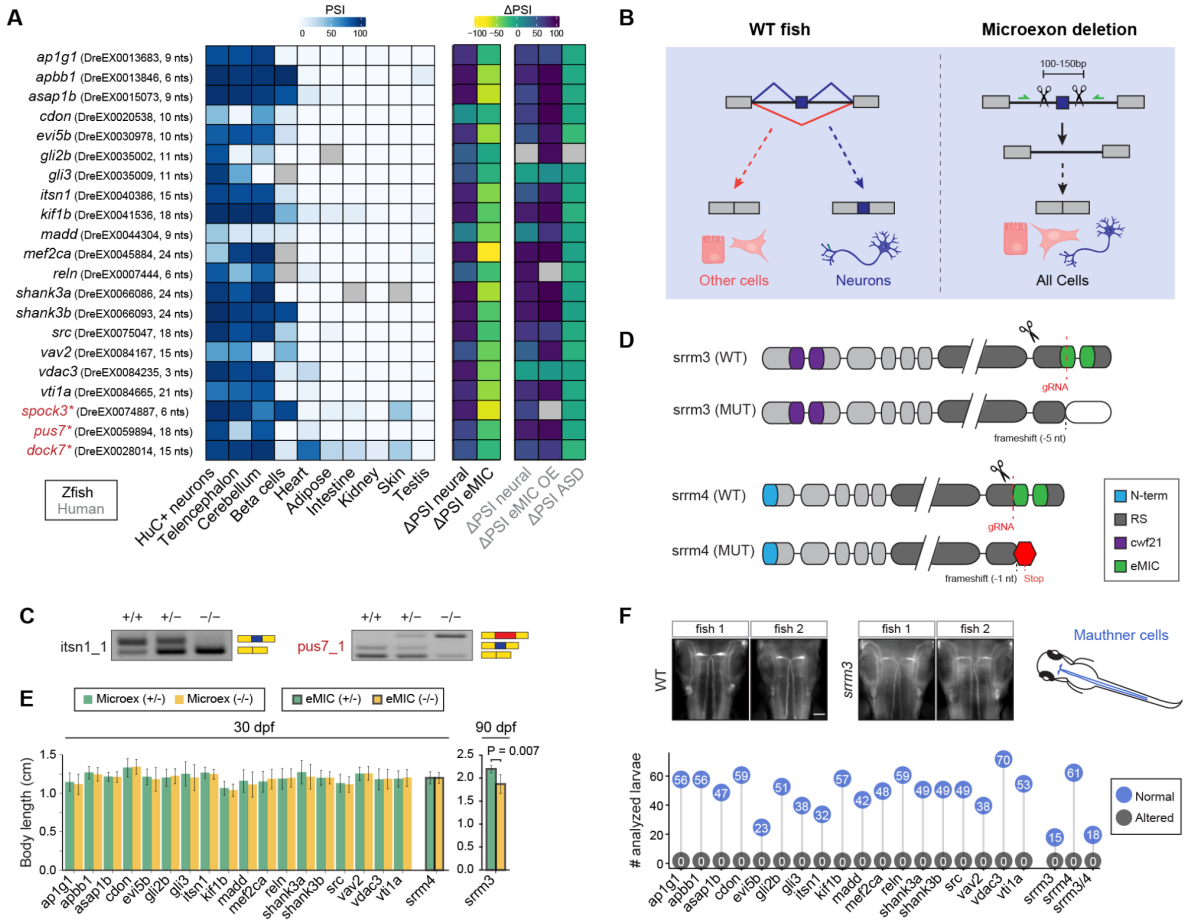

Figure 2: Selected neural microexons and experimental design. A) Inclusion levels of the 21 selected conserved microexons across zebrafish tissues as well as differential inclusion in neural vs other tissues (ΔPSI neural) in zebrafish and human, change in inclusion in response to eMIC depletion in zebrafish (ΔPSI eMIC) or eMIC overexpression in human (ΔPSI eMIC OE), and change in inclusion between ASD patients and control individuals (ΔPSI ASD). The three microexons with asterisks were excluded from phenotypic analyses. **B)** Schematic representation of the CRISPR-Cas9 based deletions of individual microexons. A pair of guide RNAs flanking each microexon were designed, which is expected to lead to normal gene expression without the microexon in all cells. **C)** Examples of two RT-PCRs testing the inclusion of the targeted microexon upon CRISPR-Cas9 removal. *itsn1_1* shows the expected clean deletion in the homozygous, while *pus7_1* exhibits inclusion of a cryptic sequence of higher length (red block) (see Figure 2 - figure supplement 1). **D)** Schematic representation of *srrm3* and *srrm4* protein domains and the impact of the CRISPR-Cas9 derived mutations (from (Ciampi, et al. 2022)). **E)** Distribution of body lengths at 30 dpf for heterozygous (green) and homozygous (yellow) fish for each microexon deletion or the *srrm4* mutation. For *srrm3*, the values are shown for 90 dpf. P-value corresponds to a two-sided t-test. **F)** Top: two representative images from WT and *srrm3* homozygous mutant larvae showing staining for 3A10 in Mauthner cells (schematized on the right side). Bottom: quantification of normal and altered number of larvae with respect to Mauthner cell morphology in homozygous mutants for each microexon or regulator line.

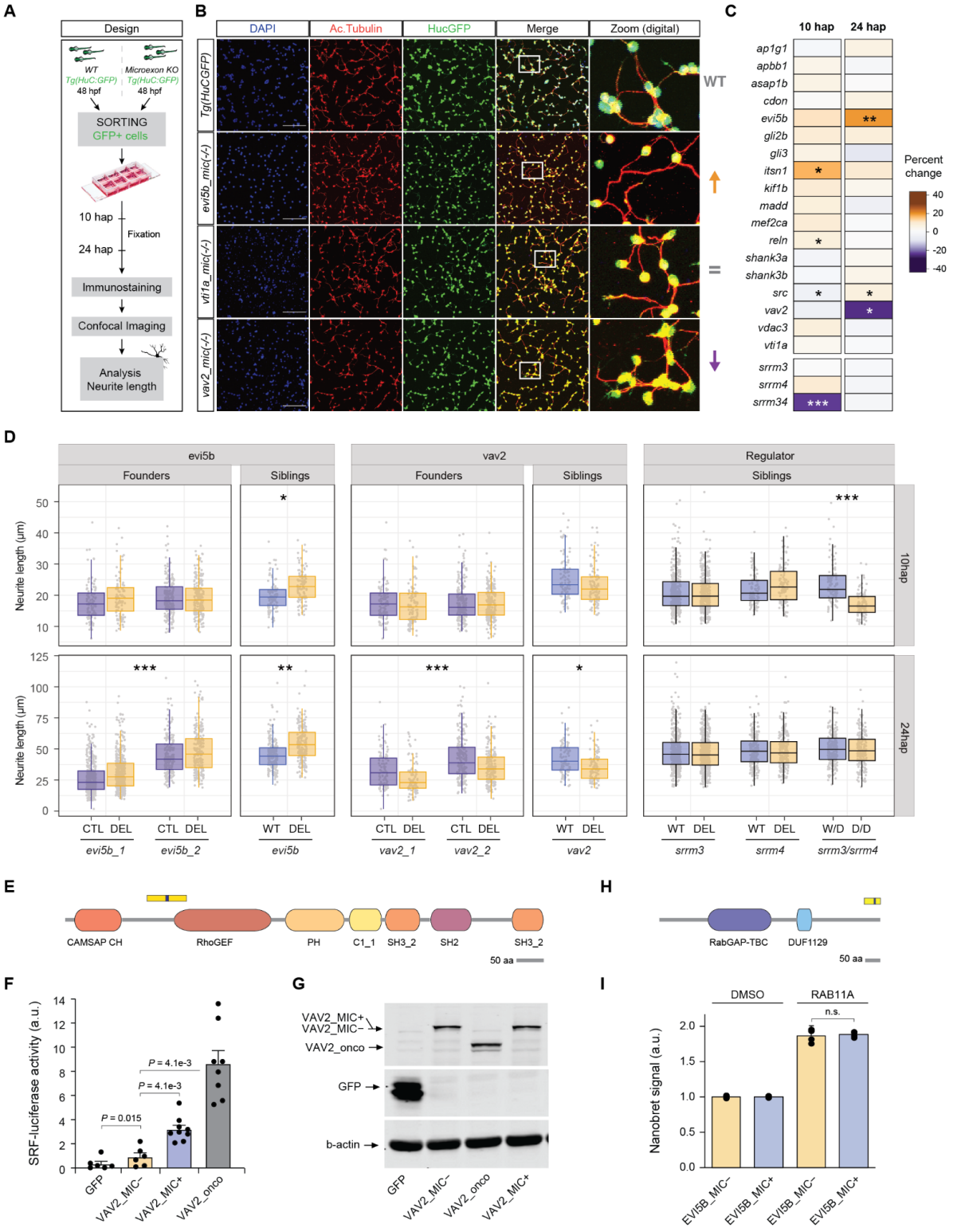

Figure 3: Impact of microexon deletion on neurite outgrowth. A) Schematic representation of the experimental design used to assess neurite outgrowth in zebrafish neuronal primary cultures (see Methods). **B)** Confocal images of example microexon deletions at 24 hours post-plating (hap). 20x magnification images, white squares indicate the zoom region amplified in the right panel (digital zoom). Scale bar 50µm. **C)** Heatmap showing the median percent of change in neurite length at 10 and 24 hap of the homozygous mutant with respect to the matched control neurons (HuC:GFP line) for each main microexon deletion line (data for all tested lines in Figure 3 - figure supplement 2). Significance is based on the median of p-value distribution of 10,000 bootstrap resampling Wilcoxon tests for each main founder. * 0.01 < p ≤ 0.001, ** 0.001 < p ≤ 0.0001, *** p < 0.0001. **D)** Boxplots of the distribution of the length of the longest neurite (one neuron per data point) for both lines of *evi5b* and *vav2*, as well as the length distributions for neurons of WT and homozygous deletion (Del) siblings for the main founders. For the regulators,

neurite length distributions for neurons of WT and homozygous mutants (Del) siblings are shown for *srrm3*, *srrm4* and the double mutant *srrm3/4*, for which the control sibling corresponds to the WT of *srrm3* but homozygous mutant for *srrm4* (i.e., *srrm4* Del). P-values correspond to ANOVA tests for *evi5b* and *vav2* founders and for siblings the median of 10,000 bootstrap Wilcoxon tests. * $0.01 < p \leq 0.001$, ** $0.001 < p \leq 0.0001$, *** $p < 0.0001$. **E)** Schematic representation of the domain architecture of VAV2 in zebrafish and region encoded by the microexon and upstream and downstream exons (upper blocks). **F)** Luciferase readout of the activation of SRF upon ectopic expression of zebrafish VAV2 proteins with and without the microexon, a negative control and an oncogenic VAV2 mutant protein in COS7 cells. P-values correspond to Student's t-test after Holm-Sidak's multiple test correction. **G)** Western blot for each overexpressed protein. **H)** Schematic representation of the domain architecture of EVI5B in zebrafish and region encoded by the microexon and upstream and downstream exons (upper blocks). Microexon inclusion/exclusion leads to different C-termini. **I)** NanoBRET quantification of protein-protein interaction between EVI5B with and without the microexon and RAB11 proteins from zebrafish.

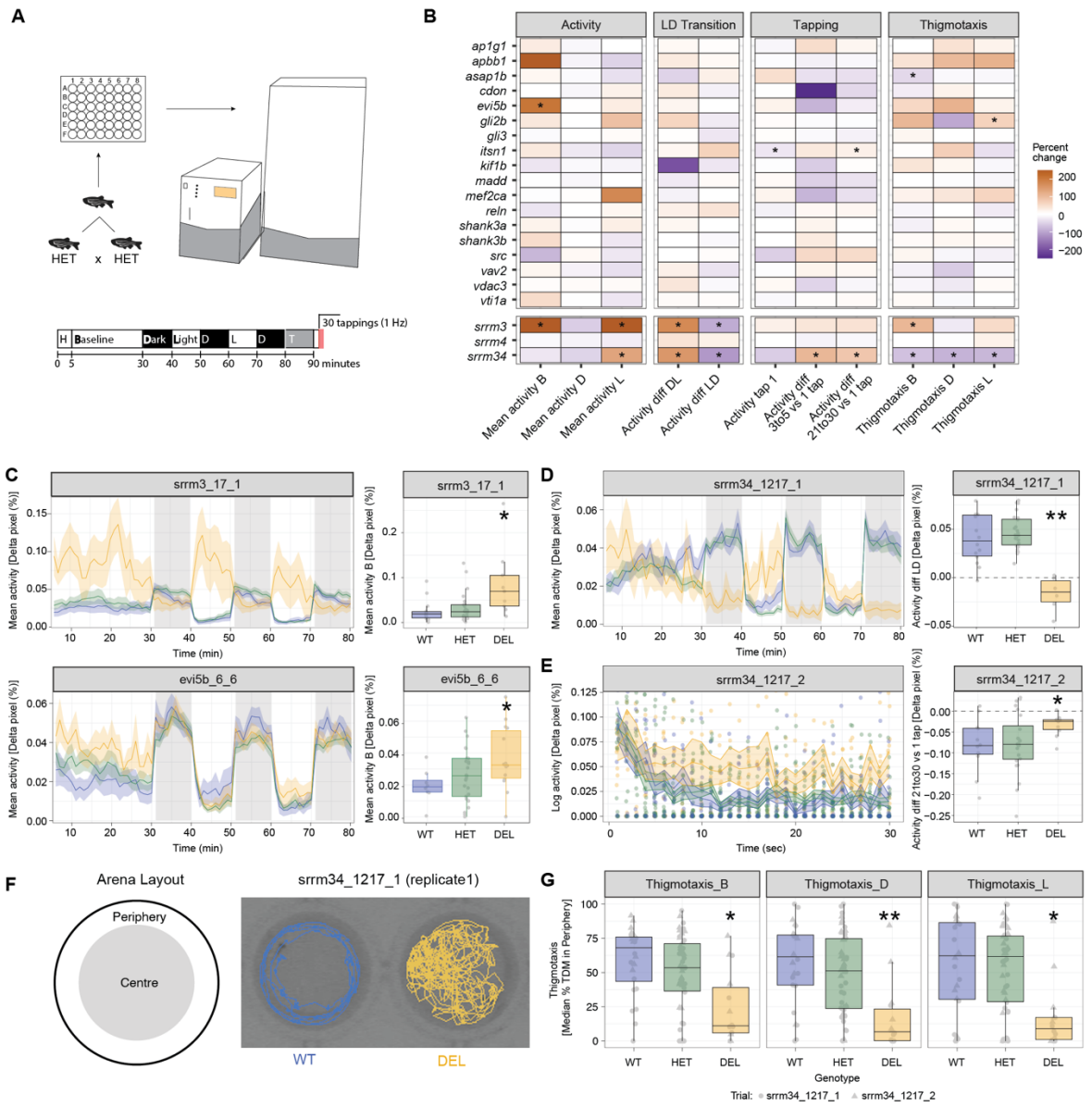

Figure 4: Impact of microexon misregulation in larval activity and response to stimuli. A) Experimental design to assess larval activity patterns and response to stimuli using the DanioVision system and the EthoVision XT - Video tracking software. The protocol we implemented consists of 5' of habituation, 25' of baseline recording, five alternating 10' intervals of dark-light, 10' of re-habituation and the tapping experiment (30 taps at 1 Hz). **B)** Heatmap showing the percent of change with respect to the WT value for the homozygous (Del) of each main microexon deletion line as well as the single and double regulator mutants for features related to activity and response to stimuli (full plots in Figure 4 - figure supplement 1-14). For visualization purposes, the percent change for median WT values equal to zero was computed using the minimum median WT value of the relative category across founders. P-values correspond to the median P-value from 100 permutation tests selecting 10 observations per genotype across replicates of the main founder. **C)** Left: Activity (percentage of Δpixels/min) plots for a representative clutch of *srrm3* and *evi5b* main lines. Traces represent mean ± SEM across larvae from the same clutch and genotype. Dark and light periods are shown with gray or white background, respectively. Right: boxplots showing the distribution of the mean baseline activity for each larvae of each genotype. P-values correspond to two-sided Wilcoxon Rank-Sum tests of each genotype against the WT. **D)** Left: Activity (percentage of Δpixels/min) plots for a representative clutch of *srrm3/4* double mutant line. Traces represent mean ± SEM across larvae from the same clutch and genotype. Dark and light periods are shown with gray or white background, respectively. Right: boxplots showing the mean difference in activity during the dark-to-light transition for each larvae of each genotype. P-values correspond to two-sided Wilcoxon Rank-Sum tests. **E)** Left: Activity (percentage of Δpixels/sec) after each of the 30 consecutive taps representative clutch of *srrm3/4* double mutant line. Traces represent mean ± SEM across larvae from the same clutch and genotype. **F)** Left: schematic representation of a well, divided between center and periphery regions. Right: two representative tracks of WT and Del *srrm3/4* larvae for 60 sec at baseline. **G)** Boxplots showing the median percentage total distance moved (TDM) (mm) in the periphery for larvae of different

genotypes of the *srrm3/4* double mutant line, under baseline, dark and light conditions. P-values correspond to two-sided Wilcoxon Rank-Sum tests of each genotype against the WT. For simplicity, in D-G, WT denotes *srrm3+/+,srrm4-/-* fish and Het *srrm3+/+,srrm4+/-* ones. For all panels: * $0.05 < p \leq 0.001$, ** $0.001 < p \leq 0.0001$, *** $p < 0.0001$.

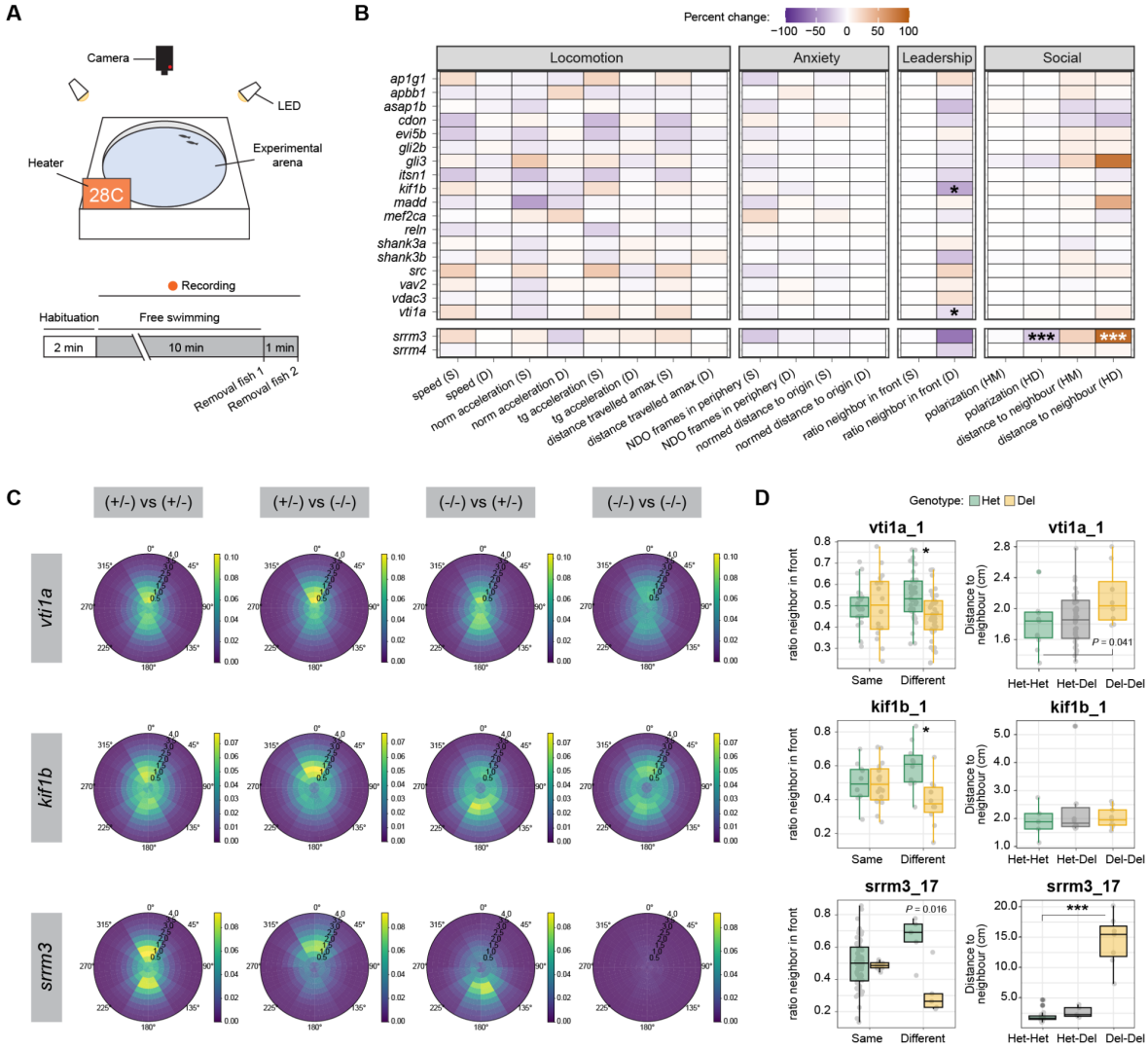

Figure 5: Impact of microexon misregulation on social behavior. A) Schematic representation of the behavioral station (details in Figure 5 - figure supplement 1) and experimental design for each tested pair of 30 dpf juveniles. **B)** Heatmap showing the percent of change with respect to the control value for each main microexon and regulator deletion line for nine different parameters related to locomotion, anxiety or social behavior (full plots in Figure 5 - figure supplement 2-10). For parameters referring to individual (locomotion, anxiety and leadership), two comparisons are shown: the average of the fish from Del-Del pairs vs the control Het-Het pairs (homotypic pairs, same "S"), or the value of the Del fish with respect to the Het one within each Het-Del pair (heterotypic pairs, different "D"). For group parameters (polarization order and distance to neighbors), the following two comparisons are shown: Het-Het vs Het-Del (HM) and Het-Het vs Del-Del (HD). **C)** Relative position map showing the position of the other fish of the pair (right genotype) with respect to the focal fish located at the center of the map (left genotype). For instance, (+/-) vs (-/-) shows the position of the Del fish respect to the focal Het one in a Het-Del pair. The merge plot of all fish pairs for *vti1a*, *kif1b* and *srrm3* are shown. **D)** Boxplots for the fish pairs shown in (C). Left: ratio in front of the non-focal fish. Lower values indicate higher leadership (i.e., more time in front). "Same" corresponds to either Het-Het or Del-Del pairs and "Different" to Het-Del pairs, with values of individual fish plotted by genotype. Right: median of the distances between the two fish throughout the time course for each genotype pair combination. P-values correspond to Wilcoxon Rank-Sum tests for the indicated comparisons. * $0.01 < p \leq 0.001$, ** $0.001 < p \leq 0.0001$, *** $p < 0.0001$.

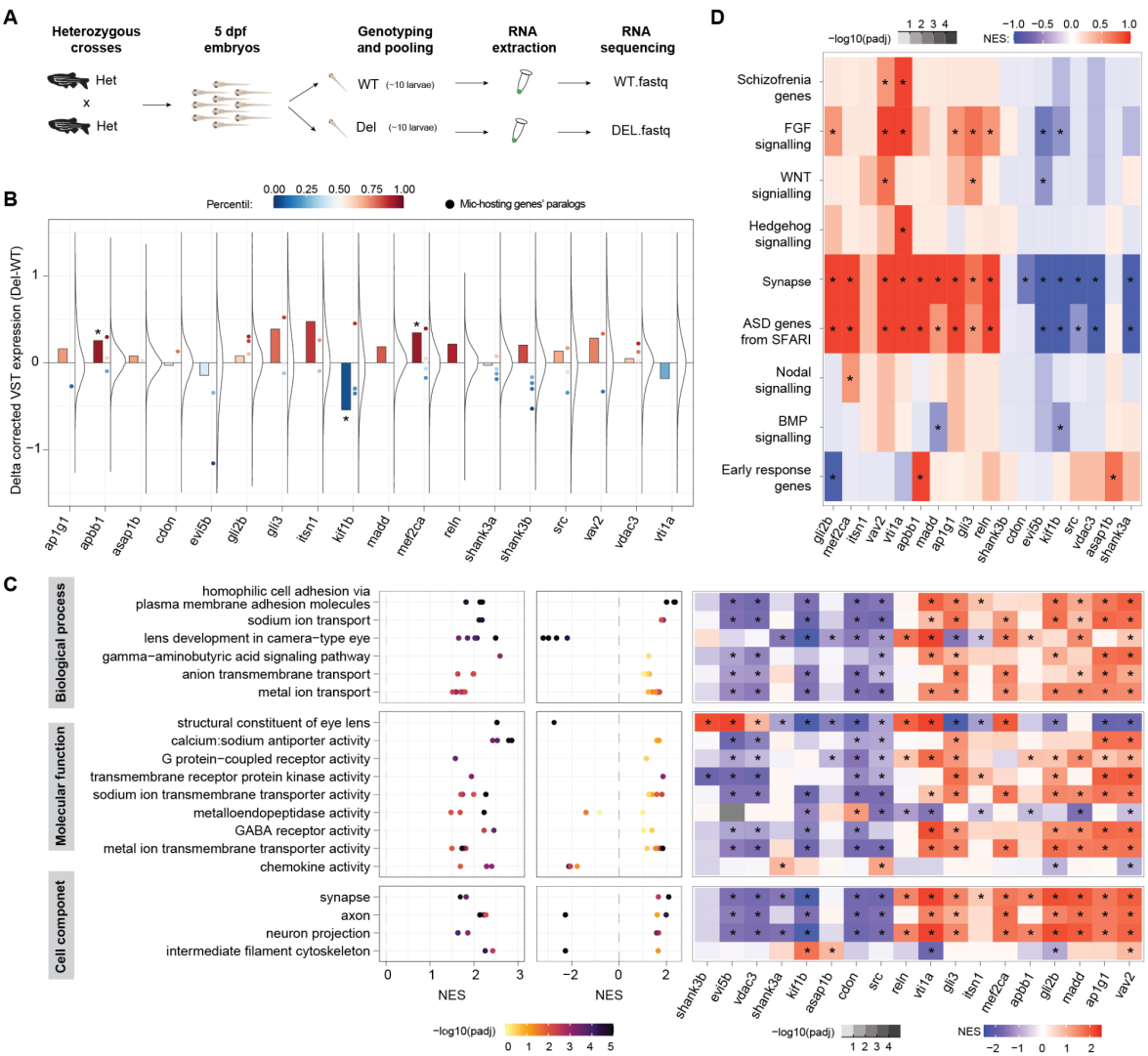

Figure 6: Transcriptomic analyses of 5 dpf larvae suggest potential compensatory changes. A) Schematic representation of the experimental design. **B)** Distribution of changes in gene expression (Δ corrected VST expression) between the Del and WT larvae for each main microexon deletion line, as well as change of the host gene (barplots) of closely related paralogs (chordate or younger origin according to Biomart) (dots). The color scale indicates the percentile of the expression change within the overall distribution. Asterisk on bars indicate change in the bottom or top decil. **C)** Left: Gene Ontology (GO) categories (dots) clustered in related groups (rows) that are enriched among genes globally changing upon individual microexon deletions. Middle: Normalized Enrichment Scores (NES; X-axis) and adjusted p-values (color code) for the same GO categories in the comparison of *srrm3* mutant larvae and WT siblings. Right: heatmap showing the NES for the gene sets comprising the union of all GO categories within each group for each specific microexon comparison. Stars indicate adjusted p-value < 0.01. **D)** NES for specific gene sets (Table S7) with relevance in neurobiology and/or development for each microexon deletion comparison.

SUPPLEMENTARY FIGURES

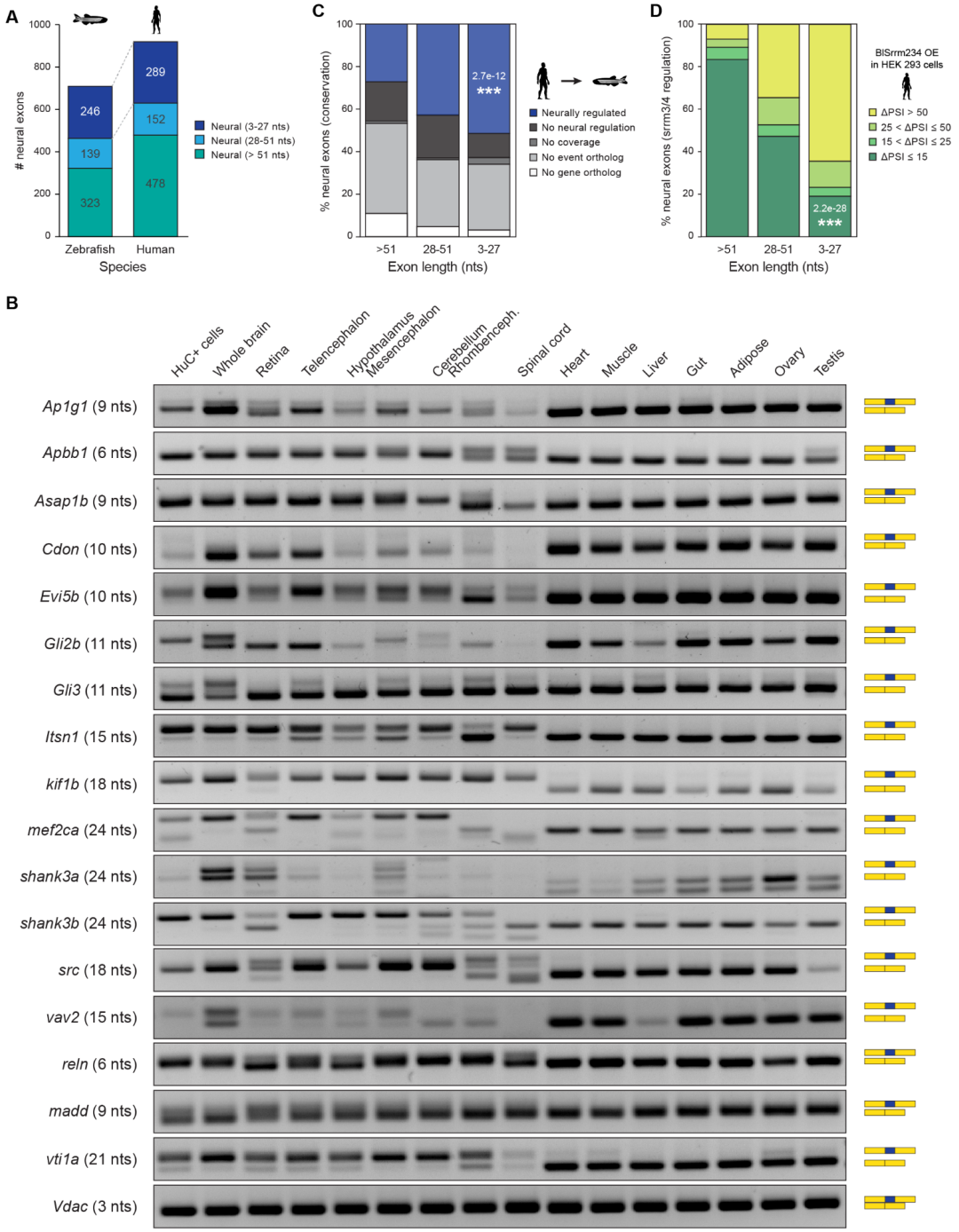

Figure 1 - figure supplement 1: Identification and validation of neural microexons in zebrafish. A) Distribution of neural exons in zebrafish and human according to their length group. **B)** RT-PCR assays assessing the inclusion of 21 selected microexons across zebrafish tissues. Primer sequences are provided in Table S4. **C)** Evolutionary conservation of human neural exons of different length group at the genomic and tissue-regulatory level compared with zebrafish. Exons conserved at the regulatory level (blue) are those with enriched inclusion in neural samples (ΔPSI ≥ 15) also in zebrafish. Those with no neural regulation (black) are conserved at the genomic level (Irimia, et al. 2009), but are not neurally enriched. Those conserved but with insufficient coverage to assess regulation are indicated as "No coverage" (dark grey). P-value corresponds to a two-sided Fisher's Exact test for neural conservation vs. others between exons > 51 nts and 3-27 nts. **E)** Distribution of exons of different length by the level of upregulation upon overexpression of the regulator in HEK cells (see Methods). P-value corresponds to a two-sided Fisher's Exact test for non-regulated exons (ΔPSI ≤ 15) vs. others between exons > 51 nts and 3-27 nts.

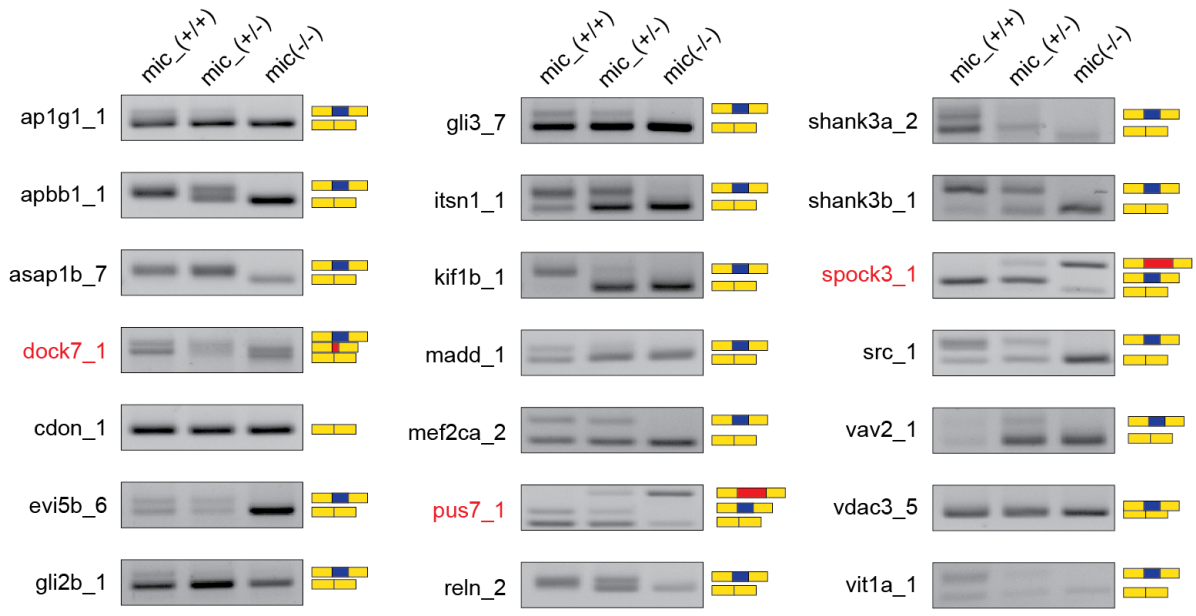

Figure 2 - figure supplement 1: Validation of microexon deletion lines. RT-PCR validations of embryo siblings for the main founder of each zebrafish microexon deletion line and genotype are shown. Wildtype (+/+), heterozygous (+/-) and homozygous (-/-). Red font indicates the three lines where the deletion of the microexon leads to the inclusion of cryptic sequences, potentially producing a loss of function of the gene. These microexons were excluded from the subsequent analyses.

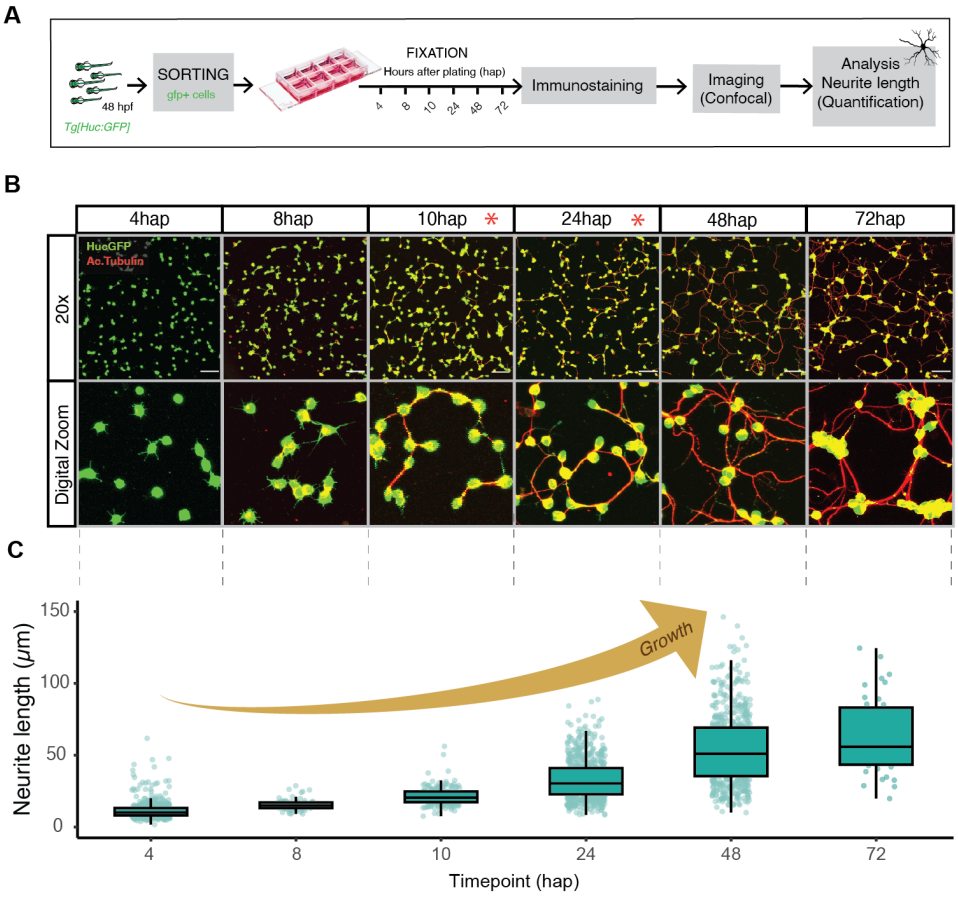

Figure 3 - figure supplement 1: Zebrafish neuronal primary culture. A) Schematic summary of the experimental steps in the generation of zebrafish neuronal primary cultures from FACS-sorted HuC:GFP cells. **B)** Confocal images of immunofluorescence anti GFP and acetylated tubulin to study zebrafish neuronal outgrowth over time (4, 8, 10, 24, 48, 72 hours after plating [hap]). Top panel: 20x confocal images. Bottom panel: digital zoom to show details of neural development progression. Red asterisk shows the two timepoints selected for this study. Scale bars 50μm. **C)** Neurite length manual quantifications of the corresponding confocal images.

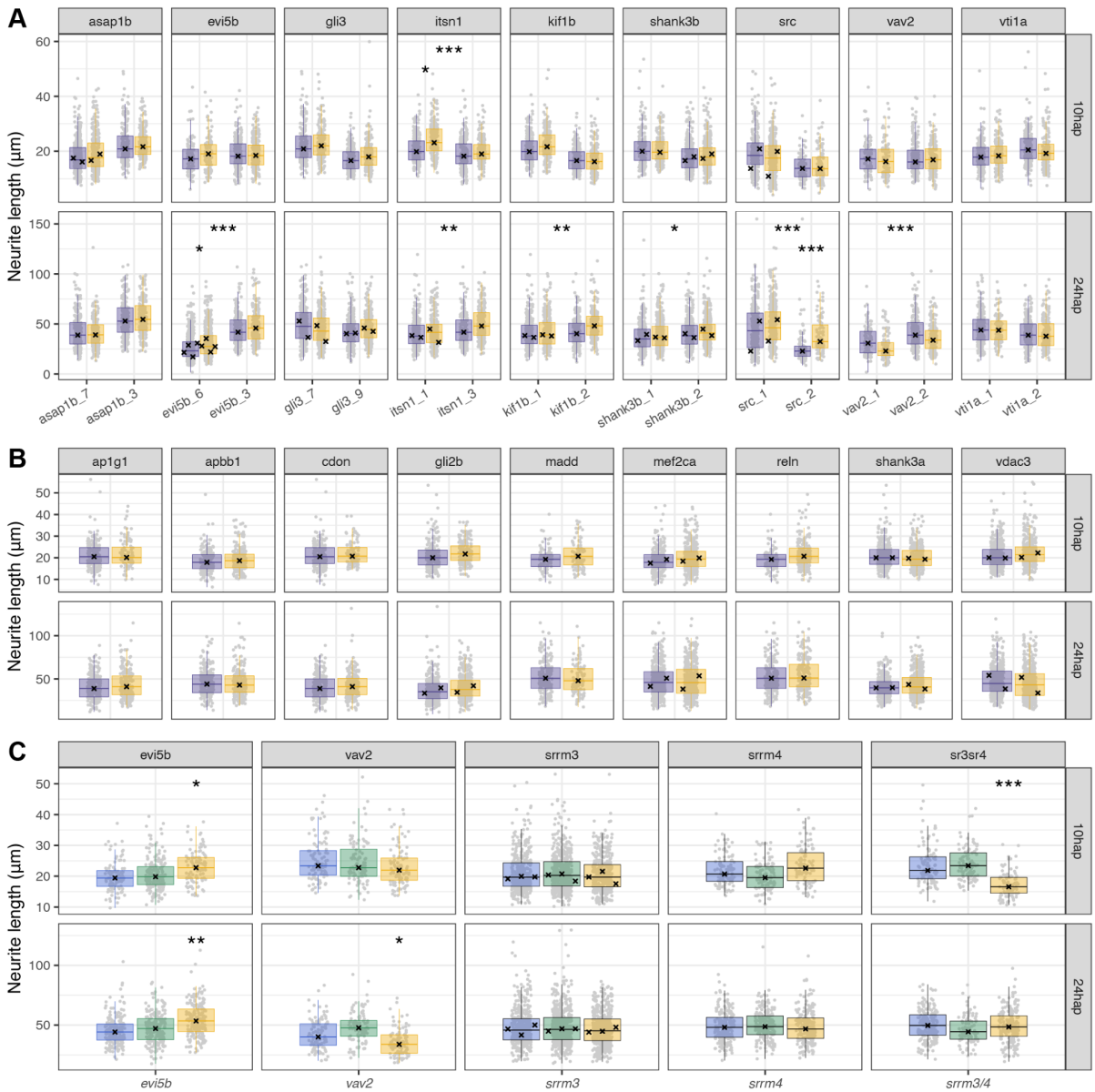

Figure 3 - figure supplement 2: Quantification of neurite outgrowth across zebrafish mutant lines. A) Boxplots showing neurite length distributions at 10 and 24 hap for each founder of the microexon deletion lines. The main founder (shown in Figure 3C) is highlighted in bold. Red boxplots correspond to neurons from a Del x Del cross for each microexon line. Dark boxplots correspond to matched control neurons from WT HuC:GFP fish processed in parallel in each experiment (see Methods). **B)** Boxplots showing neurite length distributions at 10 and 24 hap for the main founder of the microexon deletion lines. The second founder was not tested since no significant differences were found in any of the initial replicates with the exception of *reln*, for which no second founder could be obtained. **C)** Boxplots showing neurite length distributions at 10 and 24 hap for siblings of WT (blue), heterozygous (yellow) or homozygous (red) genotype. These samples were generated through Het x Het crosses, fin clip genotyping of each larva and processing of pools of larvae of the same genotype. P-value corresponds to ANOVA tests for each of the groups. * $0.01 < p \leq 0.001$, ** $0.001 < p \leq 0.0001$, *** $p < 0.0001$.

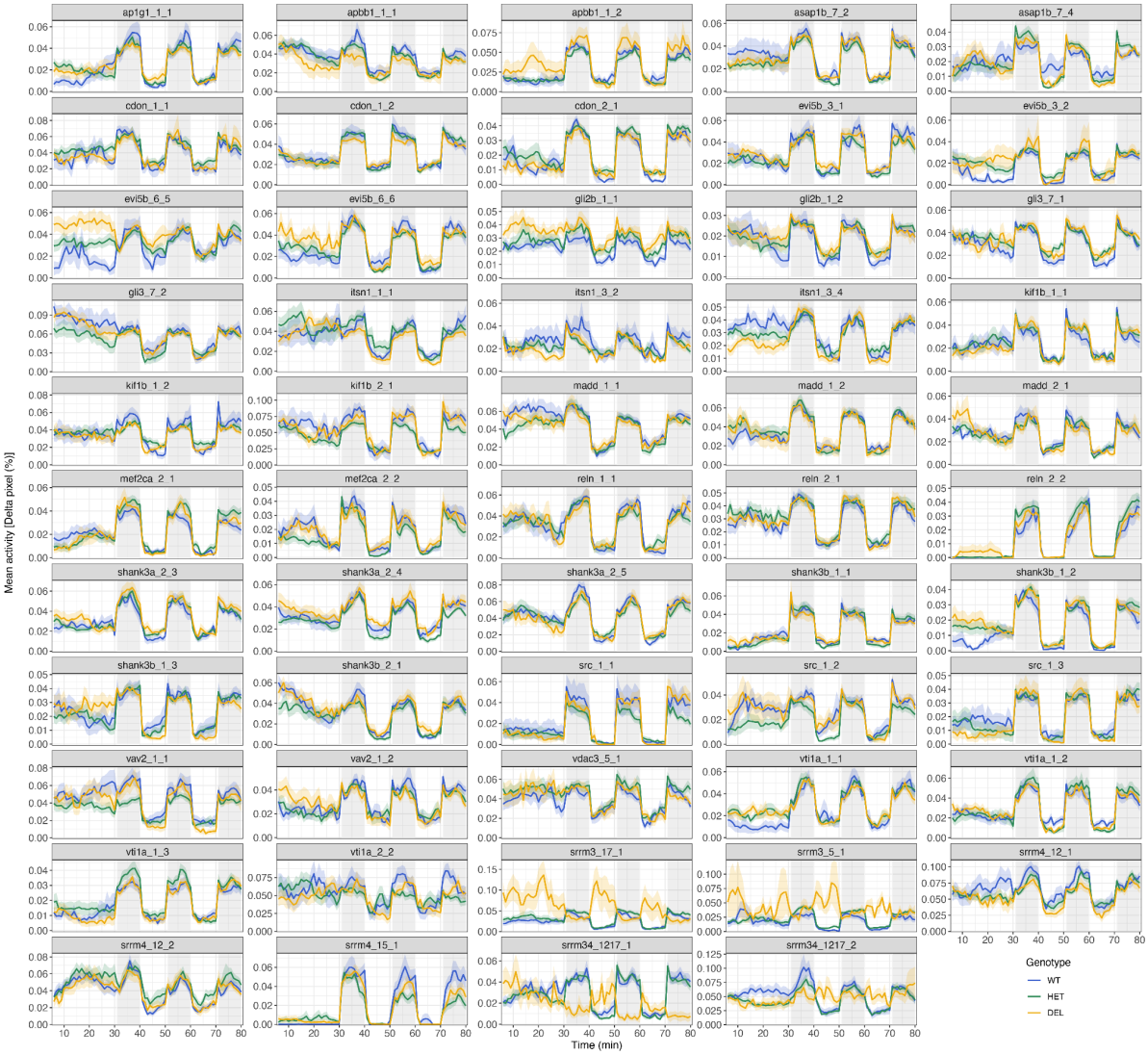

Figure 4 - figure supplement 1: Larval activity over the time course of the experiment. Activity (percentage of Δpixels/min) for each microexon and regulator deletion line and biological replicate (clutch). Traces represent mean ± SEM across larvae from the same clutch and genotype. Dark and light periods are shown with gray or white background, respectively.

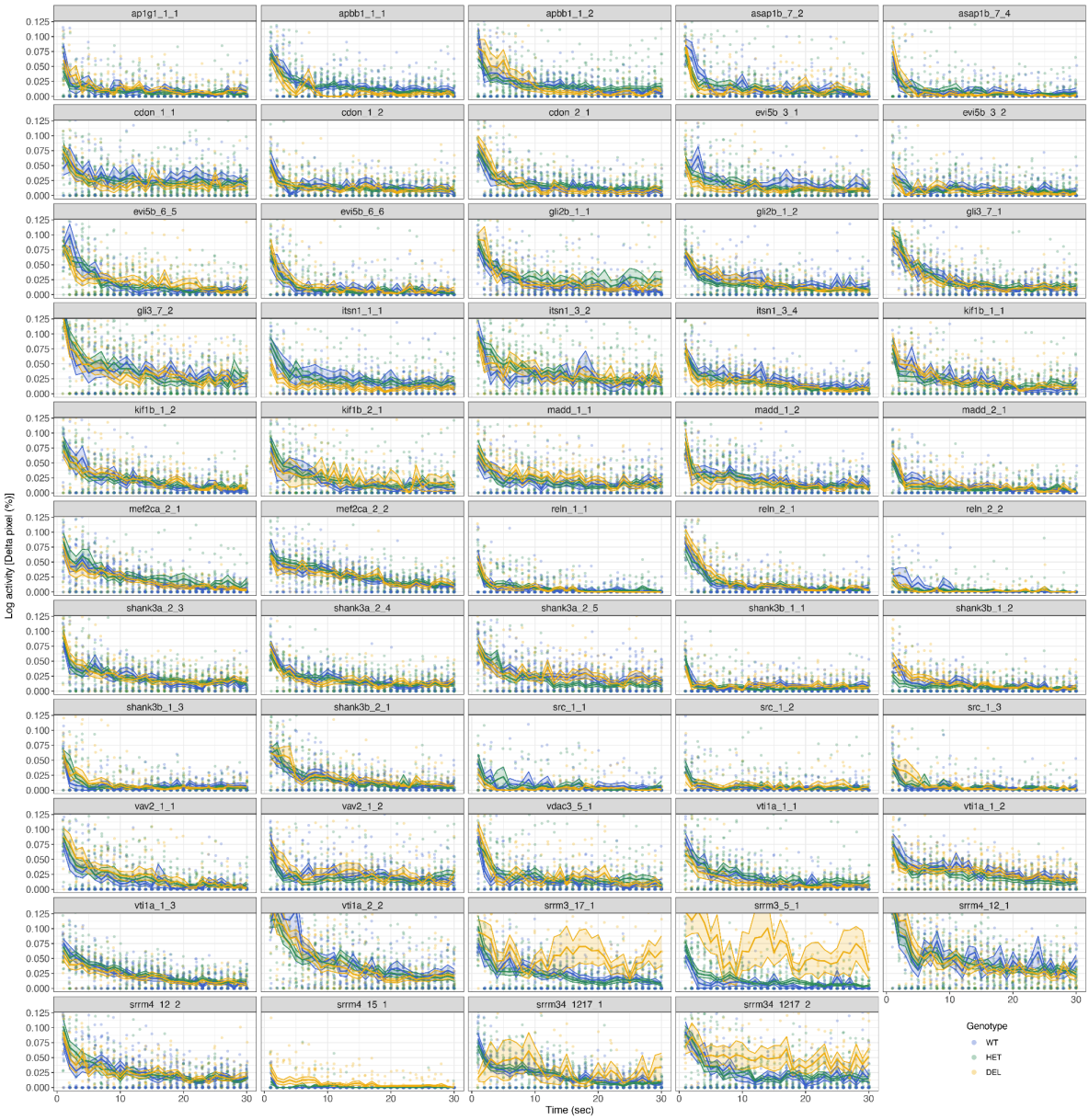

Figure 4 - figure supplement 2: Activity response and habituation to tapping stimuli. Log-scaled activity (percentage of Δpixels/sec) at each of the 30 consecutive taps for each microexon and regulator deletion line and biological replicate (clutch). A +1 pseudocount was added to the activity data for plotting purposes only. Traces represent mean ± SEM across larvae from the same clutch and genotype.

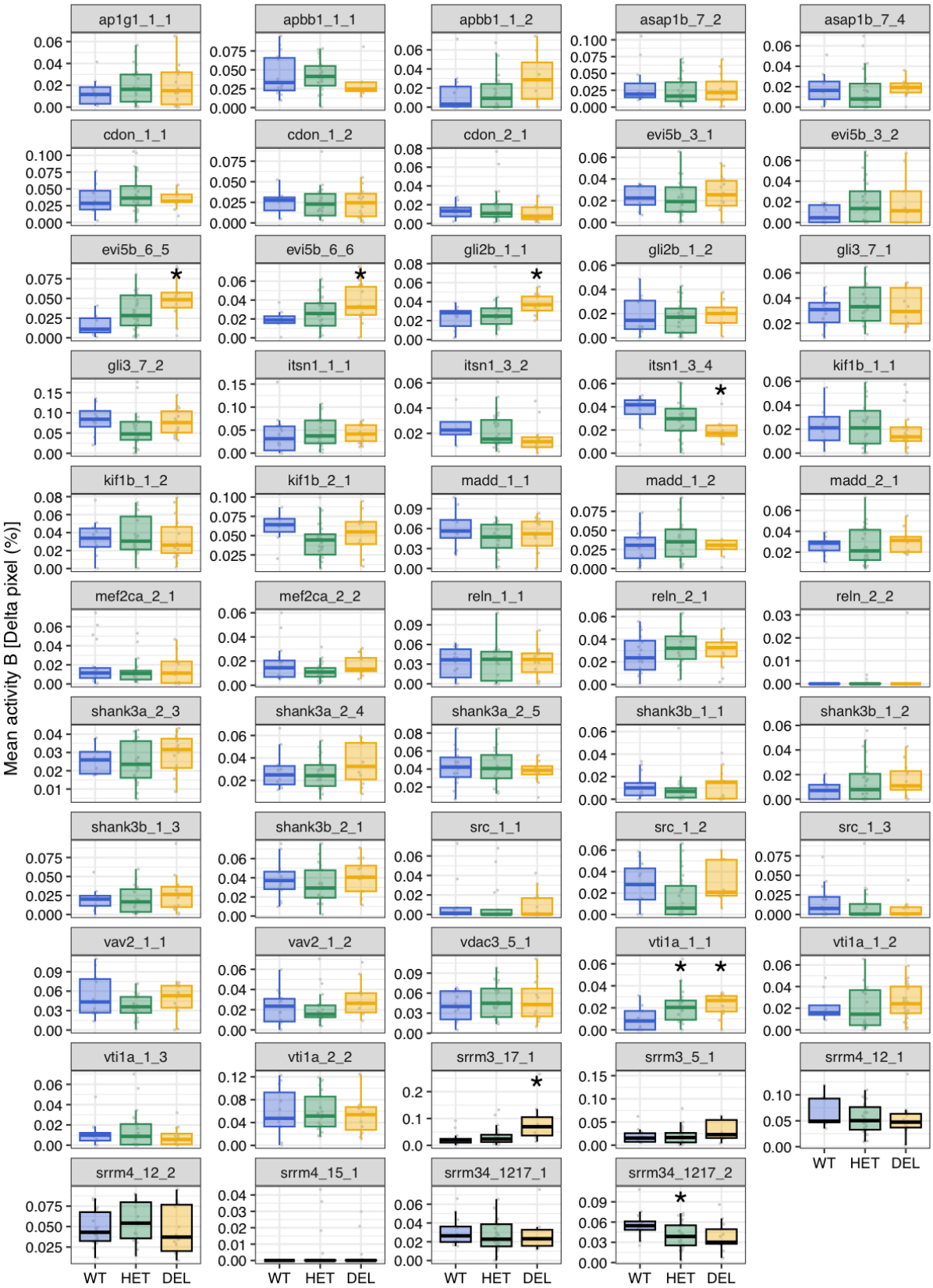

Figure 4 - figure supplement 3: Baseline activity. Boxplots showing baseline (B) activity (percentage of Δpixels/min) for each microexon and regulator deletion line and biological replicate (clutch). P-values correspond to Wilcoxon Rank-Sum tests between WT and each of the other genotypes. * 0.05 < p ≤ 0.001, ** 0.001 < p ≤ 0.0001, *** p < 0.0001.

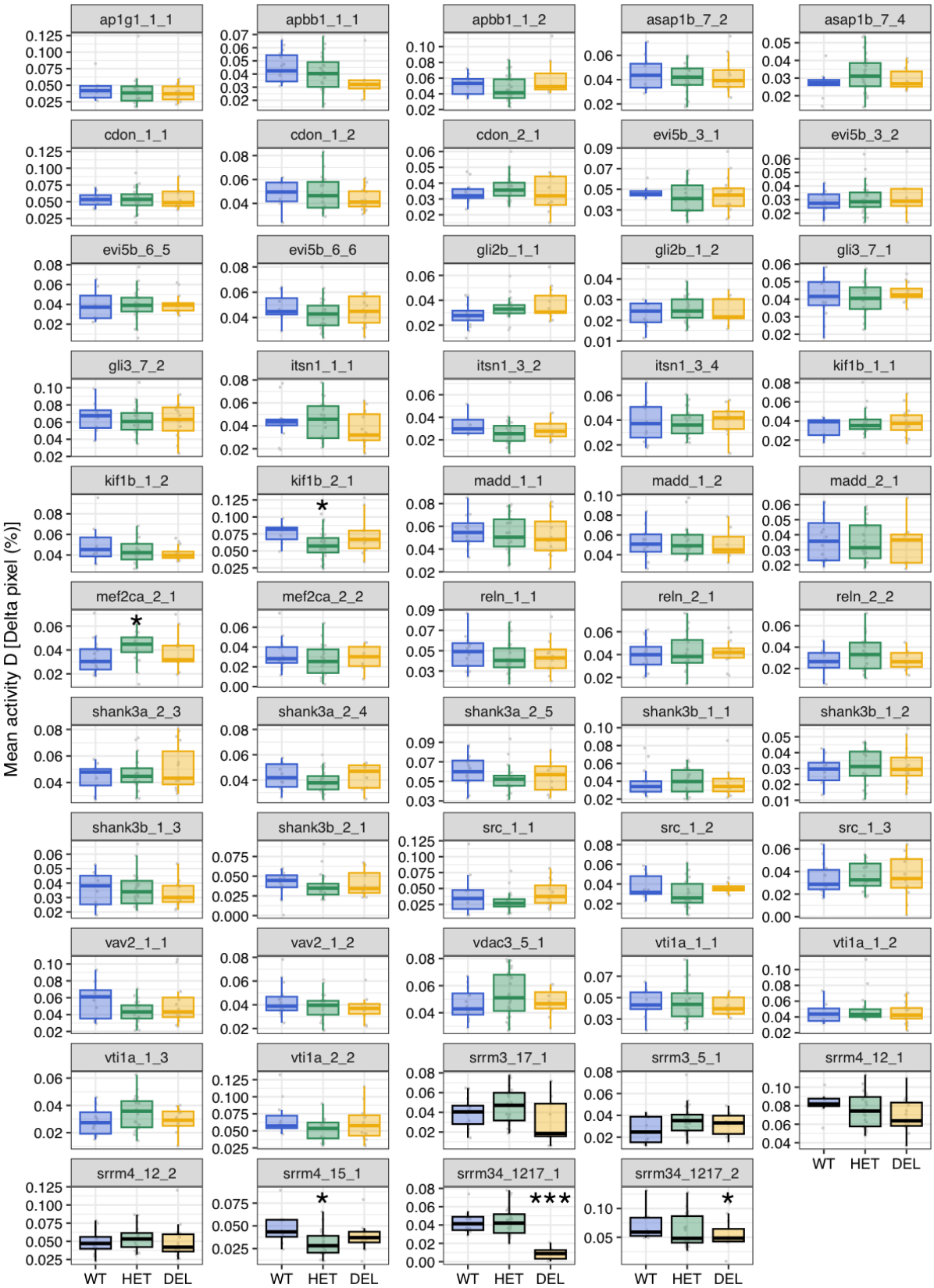

Figure 4 - figure supplement 4: Activity during the light intervals. Boxplots showing activity (percentage of Δpixels/min) during the light intervals for each microexon and regulator deletion line and biological replicate (clutch). P-values correspond to Wilcoxon Rank-Sum tests between WT and each of the other genotypes. * 0.05 < p ≤ 0.001, *** p < 0.0001.

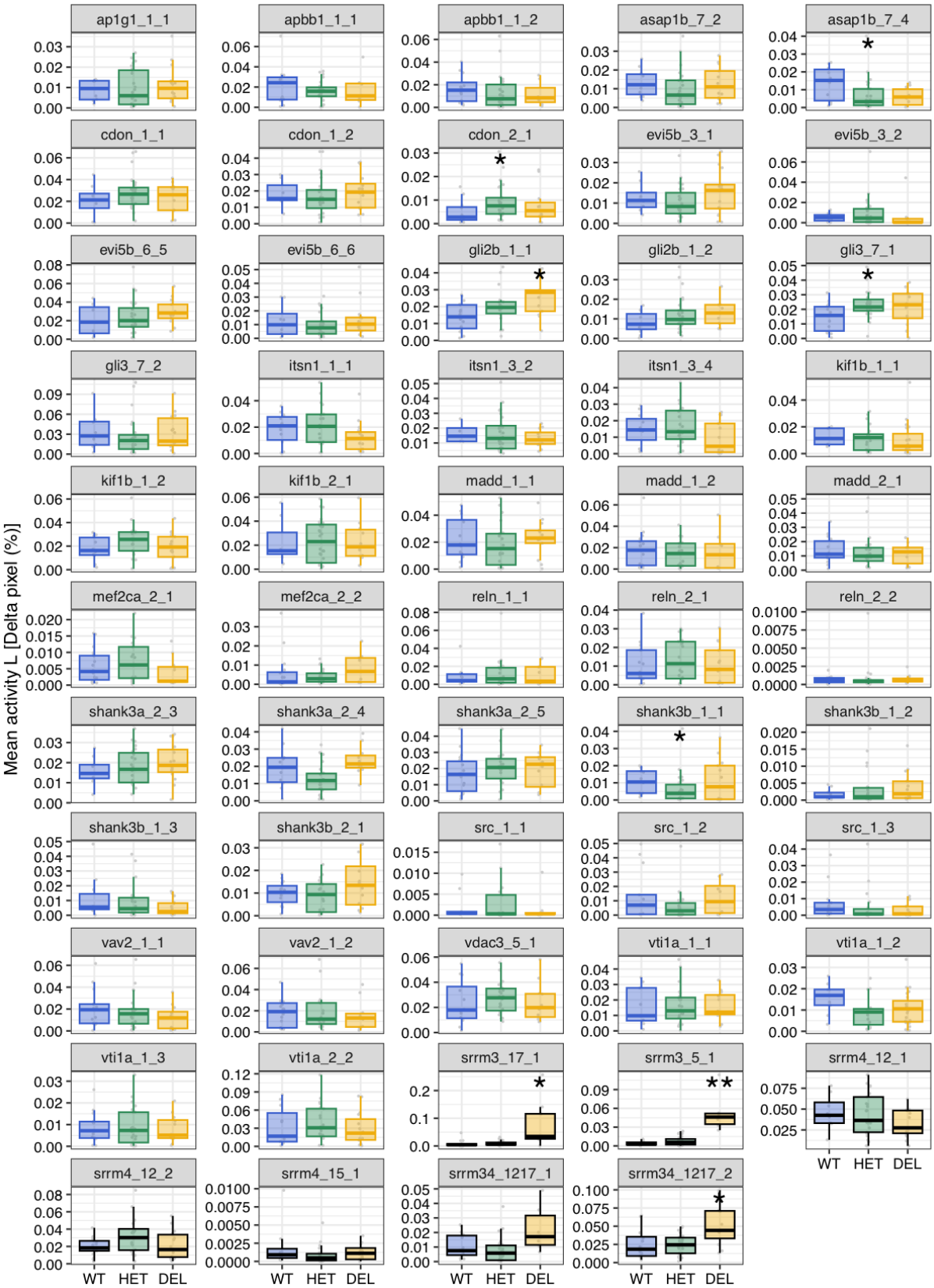

Figure 4 - figure supplement 5: Activity during the dark intervals. Boxplots showing activity (percentage of Δpixels/min) during the dark intervals for each microexon and regulator deletion line and biological replicate (clutch). P-values correspond to Wilcoxon Rank-Sum tests between WT and each of the other genotypes. * 0.05 < p ≤ 0.001, ** 0.001 < p ≤ 0.0001.

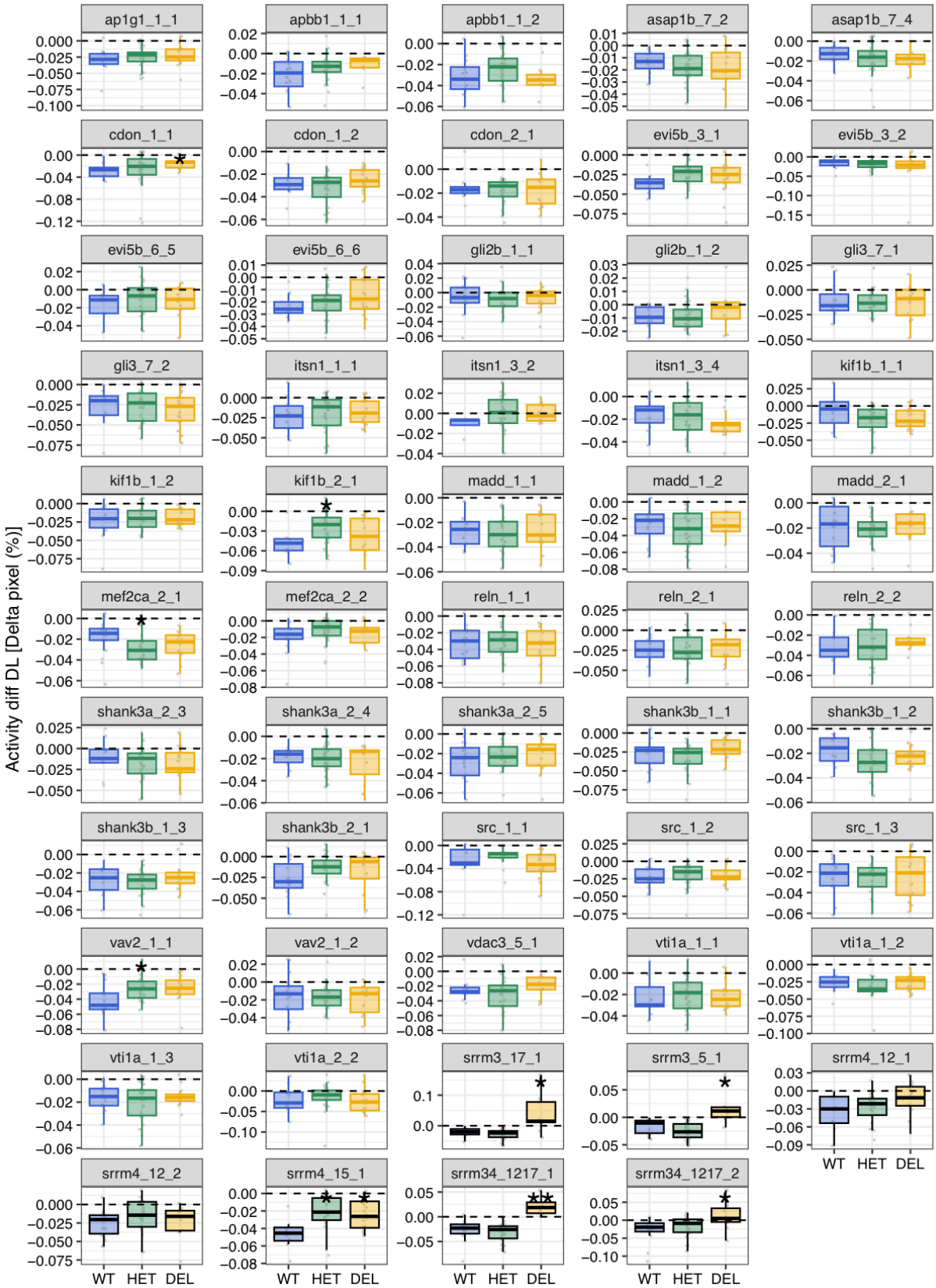

Figure 4 - figure supplement 6: Activity during the dark-to-light transitions. Boxplots showing activity (percentage of Δpixels/min) during the dark-to-light (DL) transitions for each microexon and regulator deletion line and biological replicate (clutch). P-values correspond to Wilcoxon Rank-Sum tests between WT and each of the other genotypes. * 0.05 < p ≤ 0.001, ** 0.001 < p ≤ 0.0001.

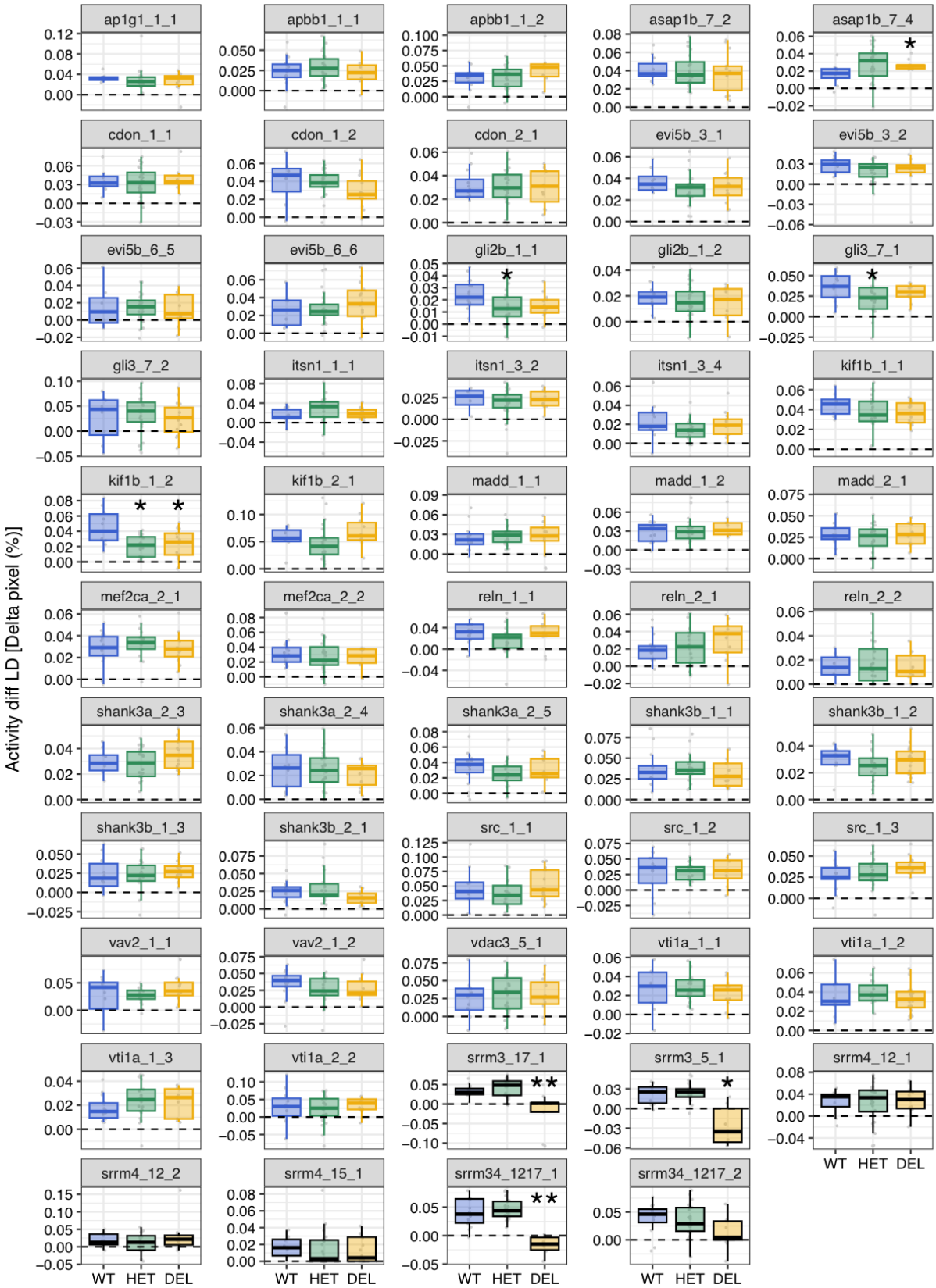

Figure 4 - figure supplement 7: Activity during the light-to-dark transitions. Boxplots showing activity (percentage of Δpixels/min) during the light-to-dark (LD) transitions for each microexon and regulator deletion line and biological replicate (clutch). P-values correspond to Wilcoxon Rank-Sum tests between WT and each of the other genotypes. * 0.05 < p ≤ 0.001, *** p < 0.0001.

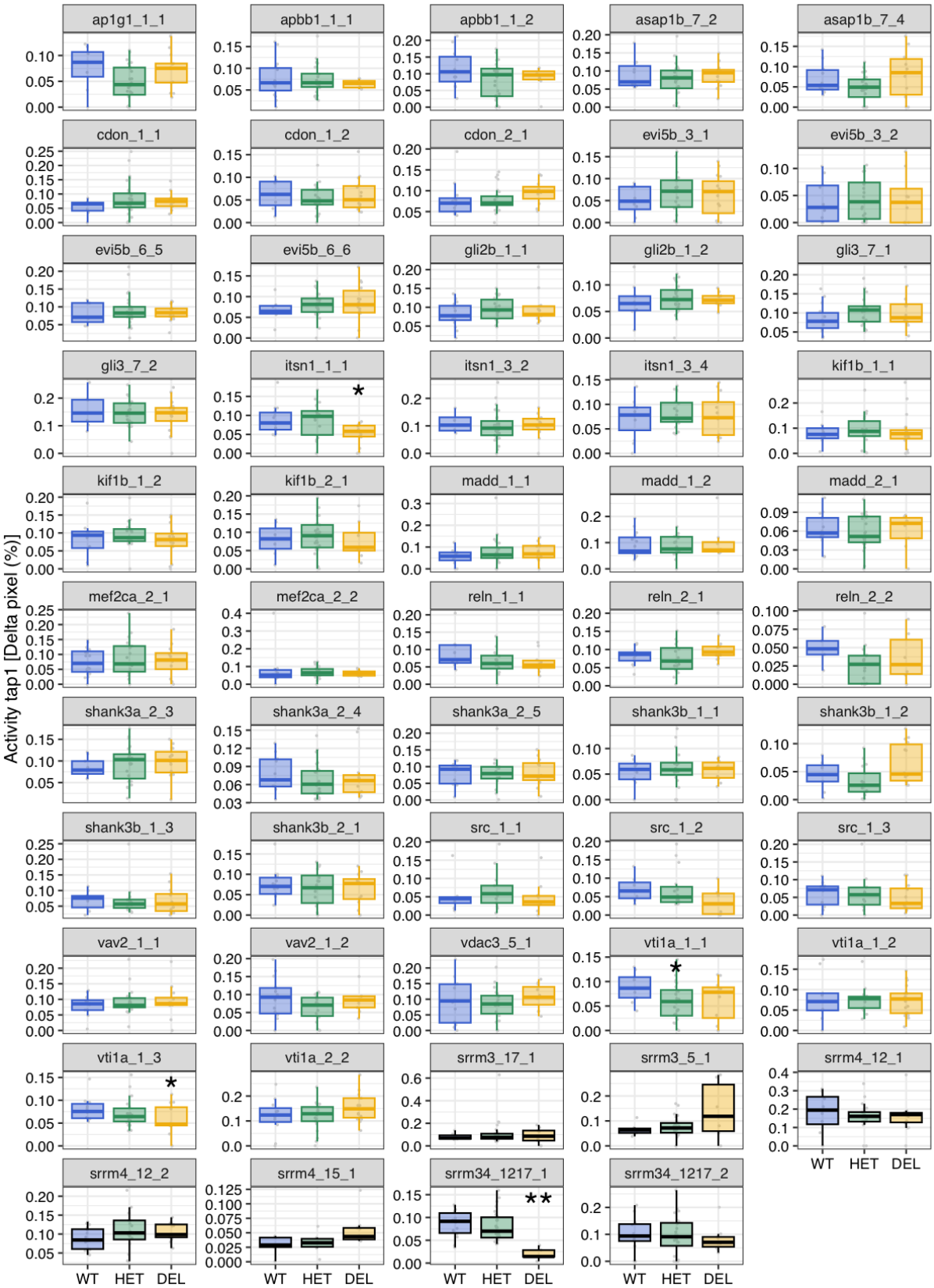

Figure 4 - figure supplement 8: Median activity after the first tap. Boxplots showing activity (percentage of Δpixels/min) after the first tap for each microexon and regulator deletion line and biological replicate (clutch). P-values correspond to Wilcoxon Rank-Sum tests between WT and each of the other genotypes. * 0.05 < p ≤ 0.001, ** 0.001 < p ≤ 0.0001.

Figure 4 - figure supplement 9: Difference in activity between the first tap and taps 3-5. Boxplots showing the change in activity in the first tap vs. taps 3-5 for each microexon and regulator deletion line and biological replicate (clutch). P-values correspond to Wilcoxon Rank-Sum tests between WT and each of the other genotypes. * 0.05 < p ≤ 0.001.

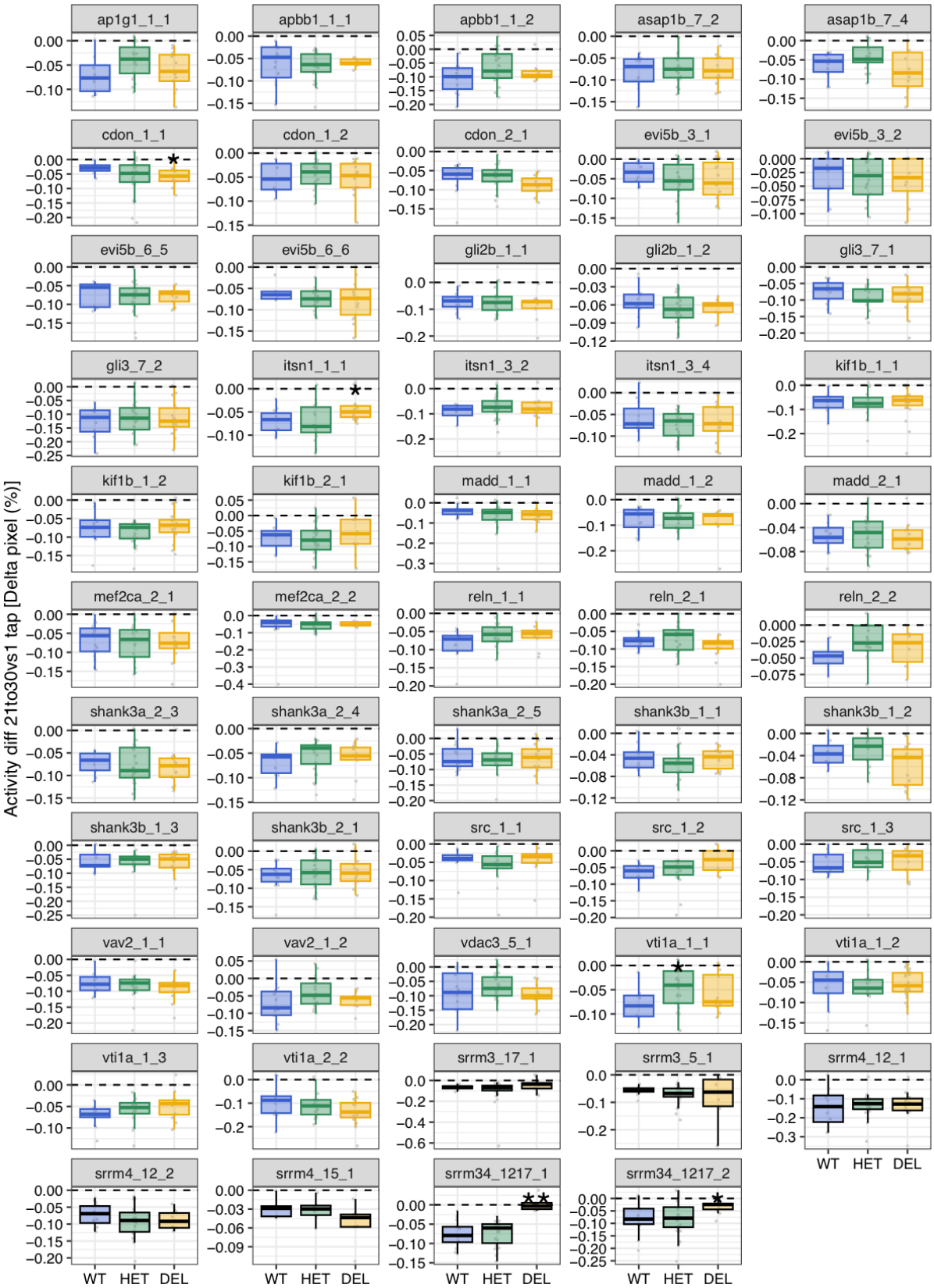

Figure 4 - figure supplement 10: Difference in activity between the first tap and taps 21-30. Boxplots showing the change in activity in the first tap vs. taps 21-30 for each microexon and regulator deletion line and biological replicate (clutch). P-values correspond to Wilcoxon Rank-Sum tests between WT and each of the other genotypes. * 0.05 < p ≤ 0.001, ** 0.001 < p ≤ 0.0001.

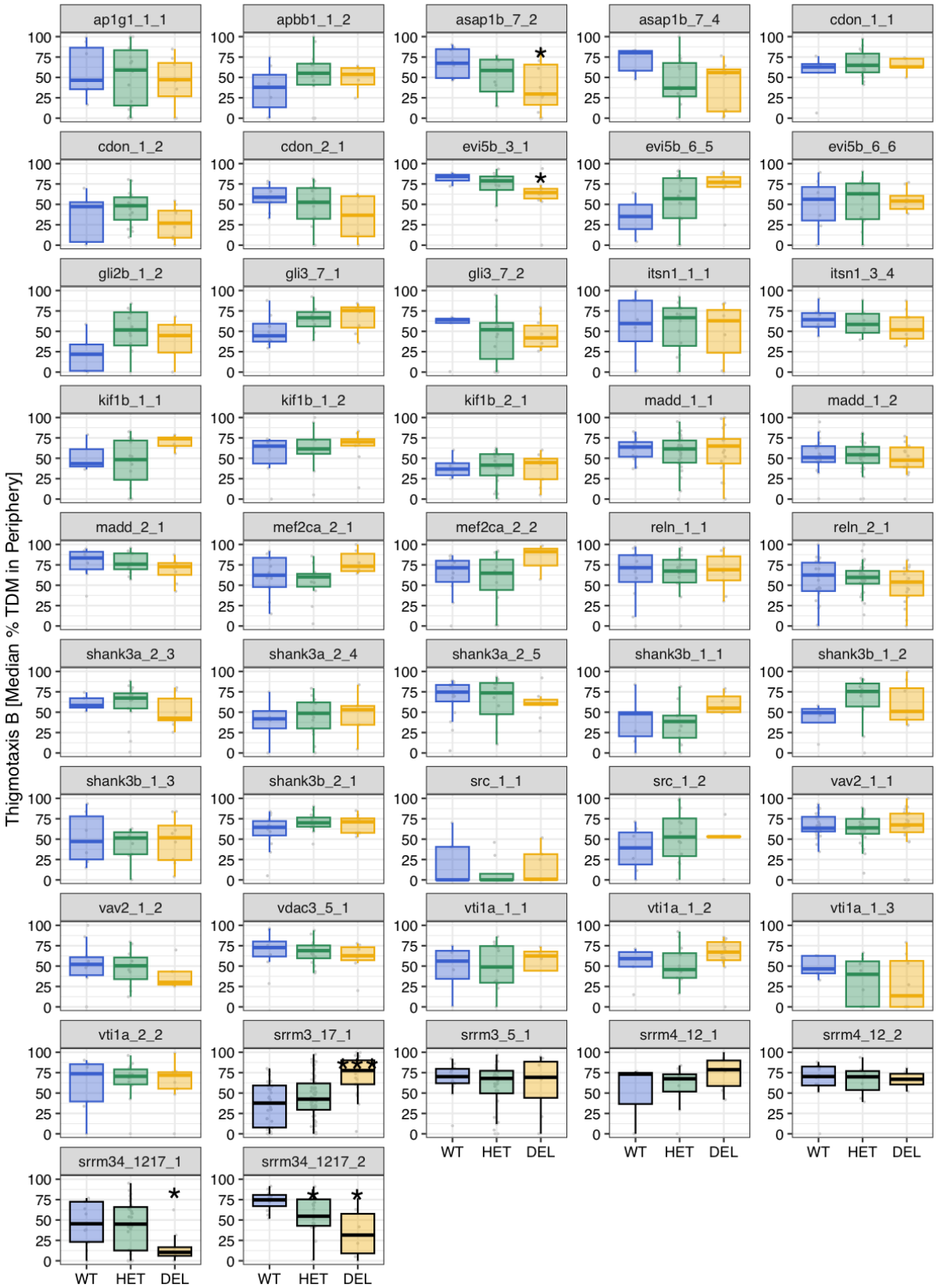

Figure 4 - figure supplement 11: Thigmotaxis during the baseline condition. Boxplots showing activity (percentage of Δpixels/min) during the baseline condition for each microexon and regulator deletion line and biological replicate (clutch). P-values correspond to Wilcoxon Rank-Sum tests between WT and each of the other genotypes. * $0.05 < p \leq 0.001$, *** $p < 0.0001$.

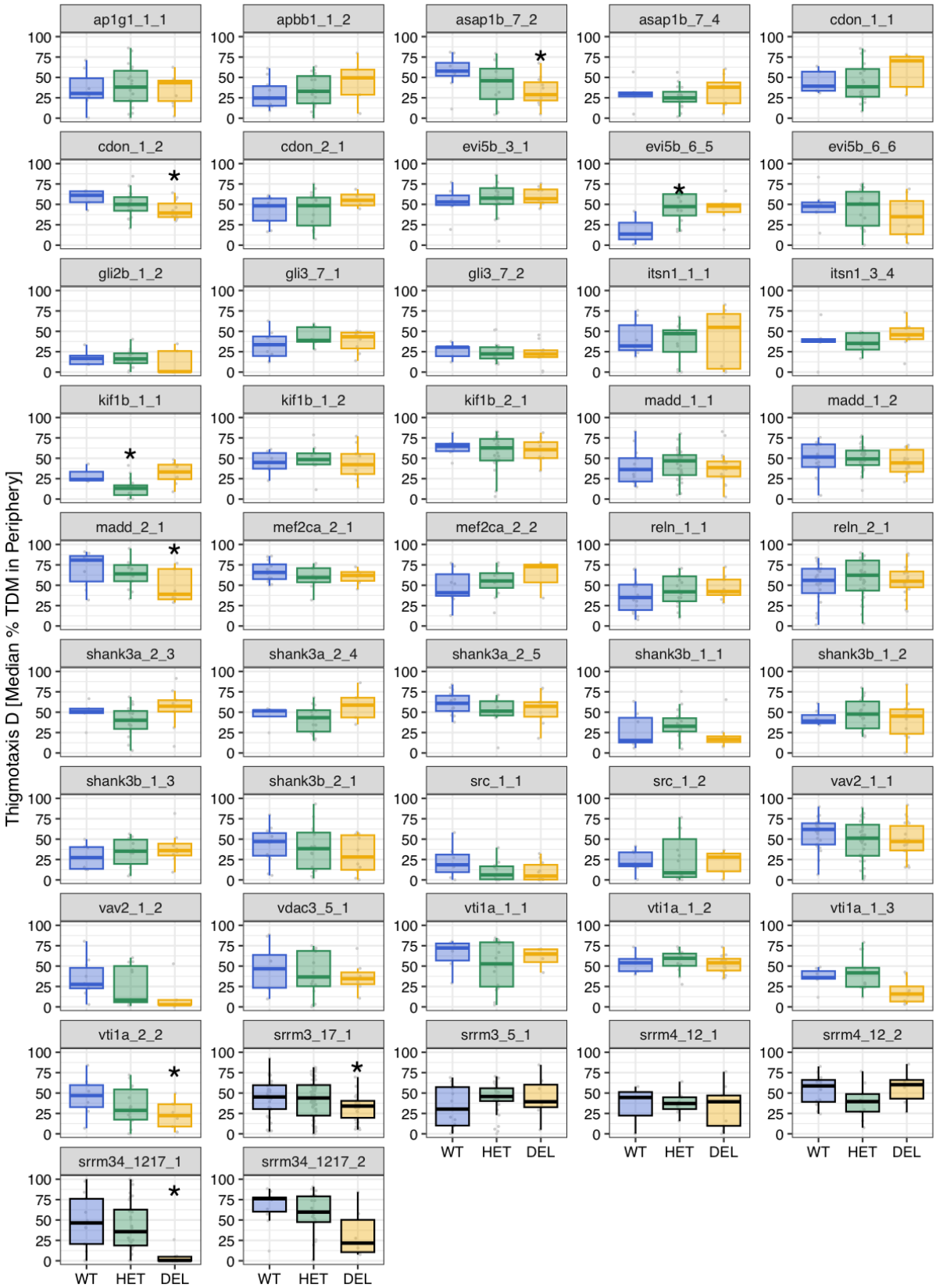

Figure 4 - figure supplement 12: Thigmotaxis during the light intervals. Boxplots showing activity (percentage of Δpixels/min) during the light intervals for each microexon and regulator deletion line and biological replicate (clutch). P-values correspond to Wilcoxon Rank-Sum tests between WT and each of the other genotypes. * 0.05 < p ≤ 0.001.

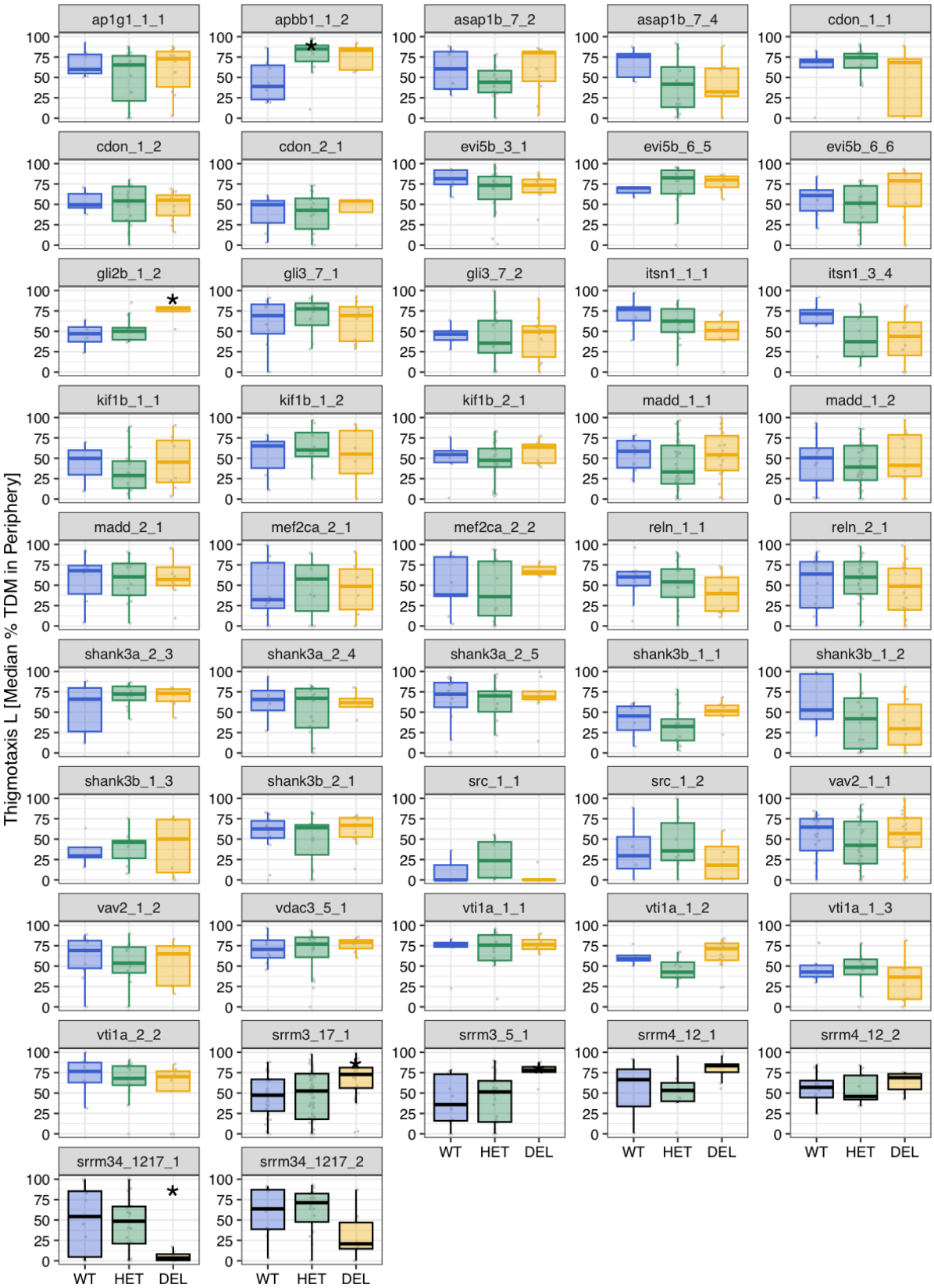

Figure 4 - figure supplement 13: Thigmotaxis during the dark intervals. Boxplots showing activity (percentage of Δpixels/min) during the dark intervals for each microexon and regulator deletion line and biological replicate (clutch). P-values correspond to Wilcoxon Rank-Sum tests between WT and each of the other genotypes. * 0.05 < p ≤ 0.001.

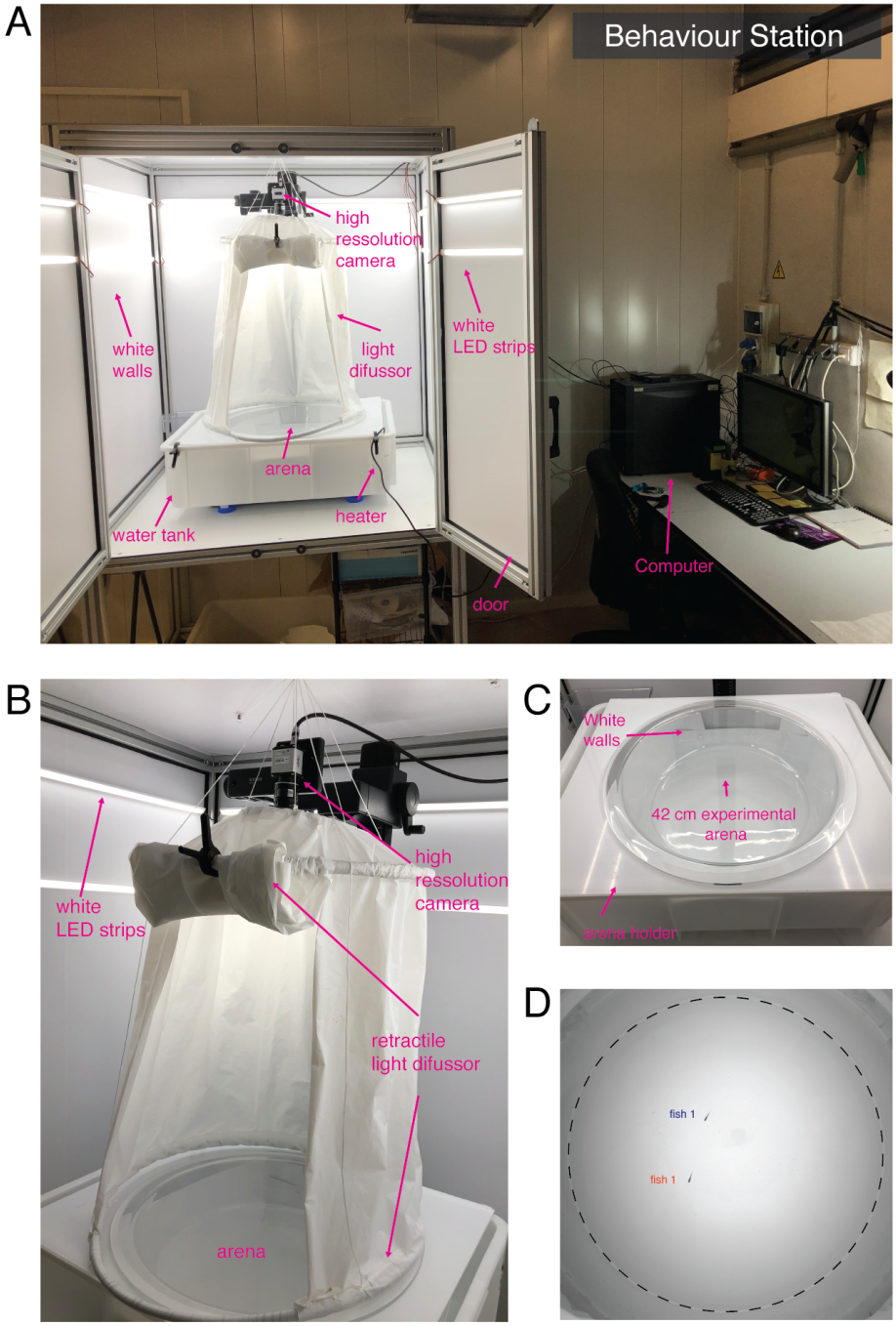

Figure 5 - figure supplement 1: Custom behavioral station. A) Overview of the behavioral system, based on (Hinz and de Polavieja 2017). **B-D)** Details of the arena used to assess social interactions between pairs of juvenile fish.

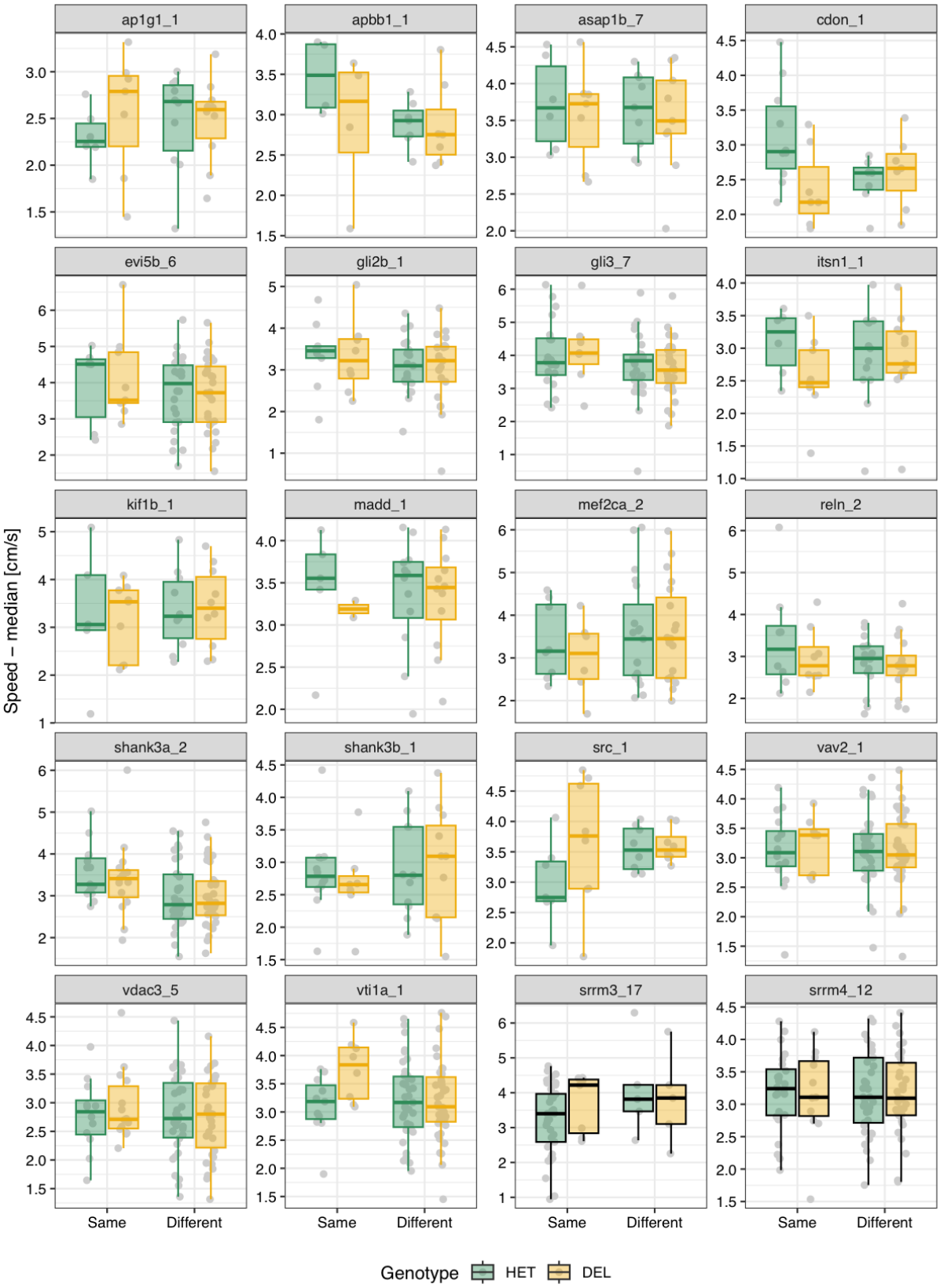

Figure 5 - figure supplement 2: Median speed by genotype for each main microexon and regulator line. A) Median speed (cm/s) for each fish over the 10' time course by pair type. "Same" corresponds to either Het-Het or Del-Del pairs, and each data point is the median of the pair, and "Different" to Het-Del pairs and each data point corresponds to an individual fish. None of the comparisons between Het and Del individuals were significant at a threshold of $P < 0.01$ using Wilcoxon Rank-Sum tests.

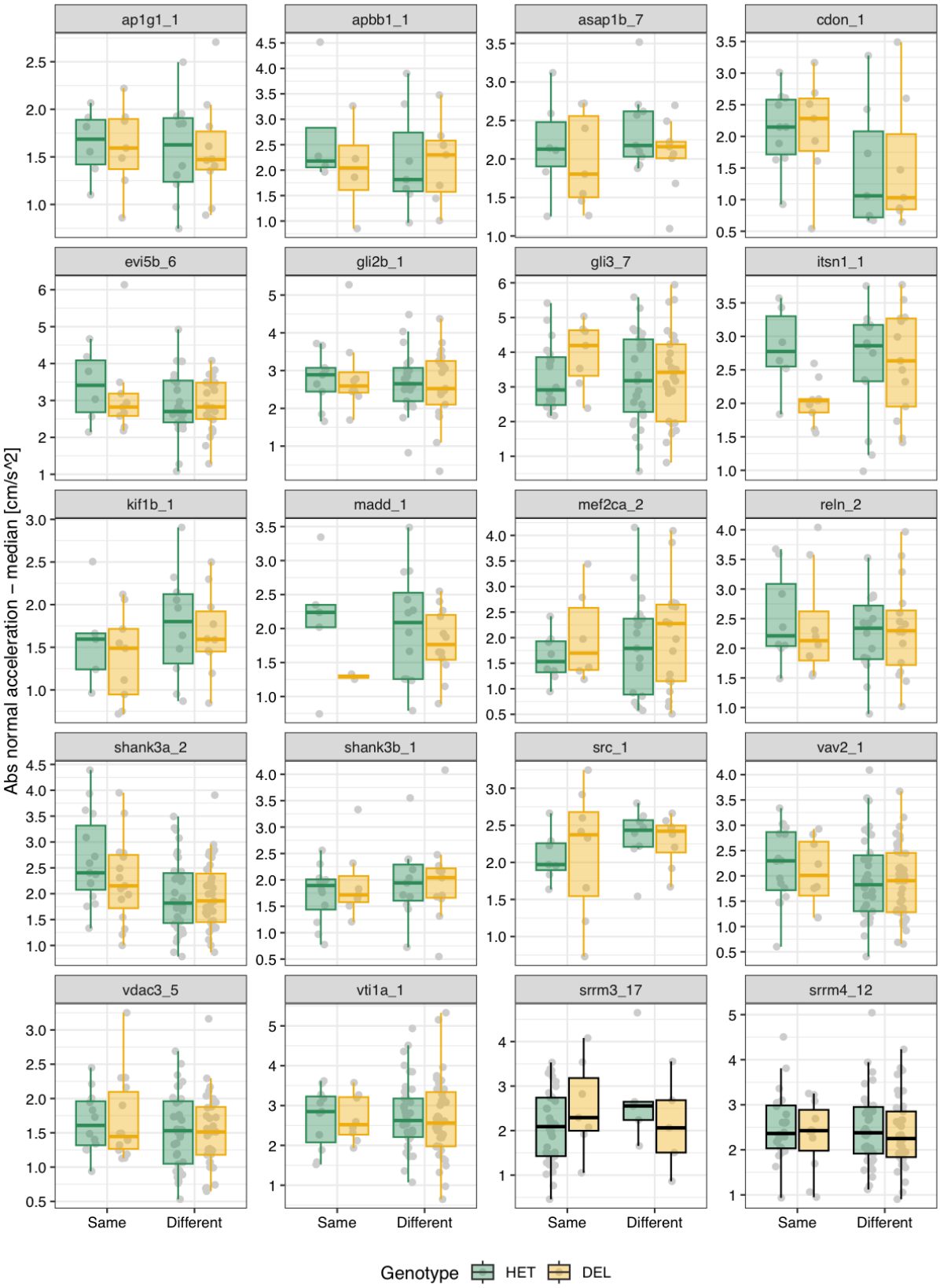

Figure 5 - figure supplement 3: Median absolute normal acceleration by genotype for each main microexon and regulator line. A) Median absolute normal acceleration (cm/s2) for each fish over the 10' time course by pair type. "Same" corresponds to either Het-Het or Del-Del pairs, and each data point is the median of the pair, and "Different" to Het-Del pairs and each data point corresponds to an individual fish. None of the comparisons between Het and Del individuals were significant at a threshold of P < 0.01 using Wilcoxon Rank-Sum tests.

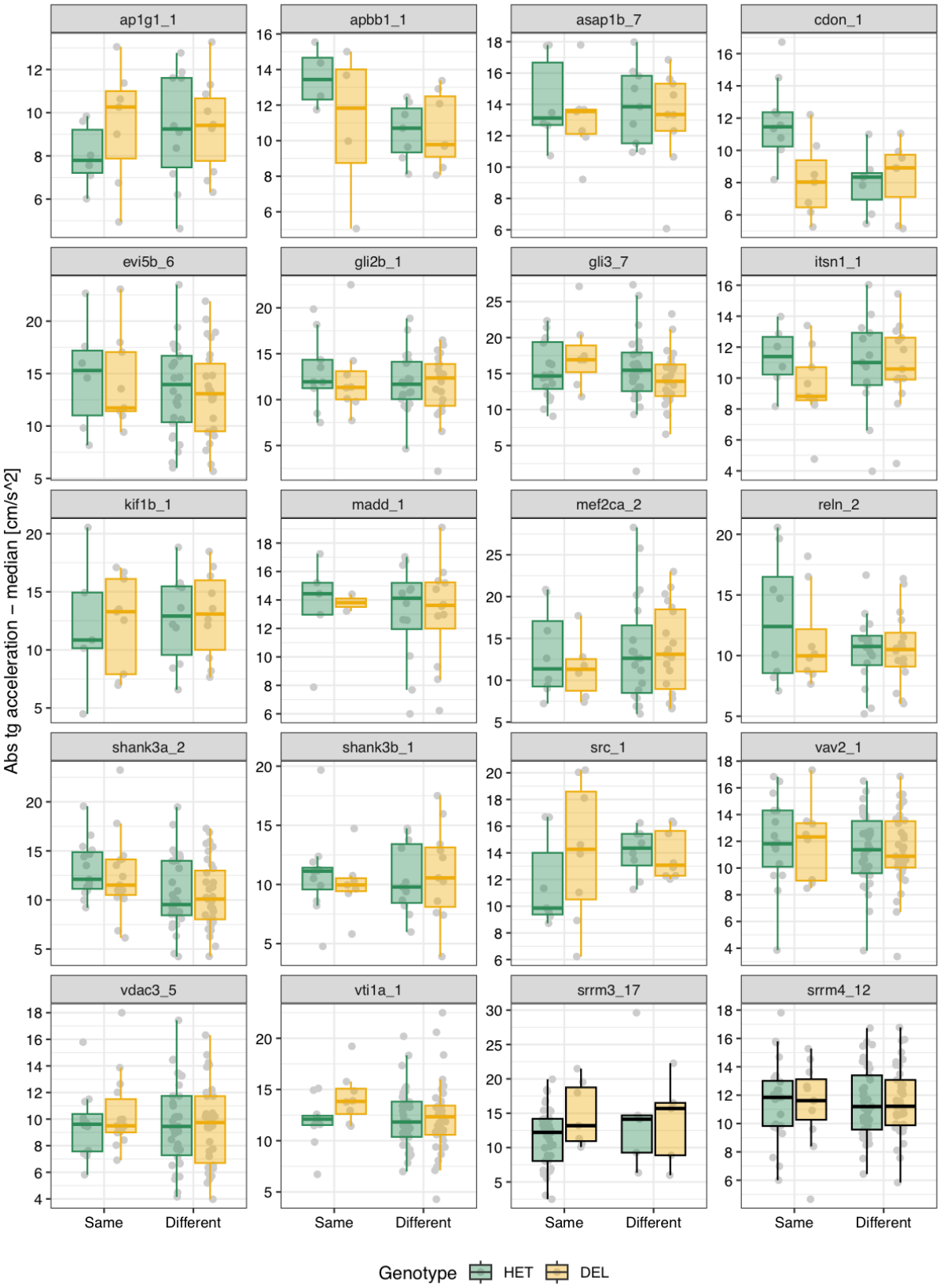

Figure 5 - figure supplement 4: Median absolute tangential acceleration by genotype for each main microexon and regulator line. A) Median absolute tangential acceleration (cm/s2) for each fish over the 10' time course by pair type. "Same" corresponds to either Het-Het or Del-Del pairs and "Different" to Het-Del pairs. None of the comparisons between Het and Del individuals were significant at a threshold of $P < 0.01$ using Wilcoxon Rank-Sum tests.

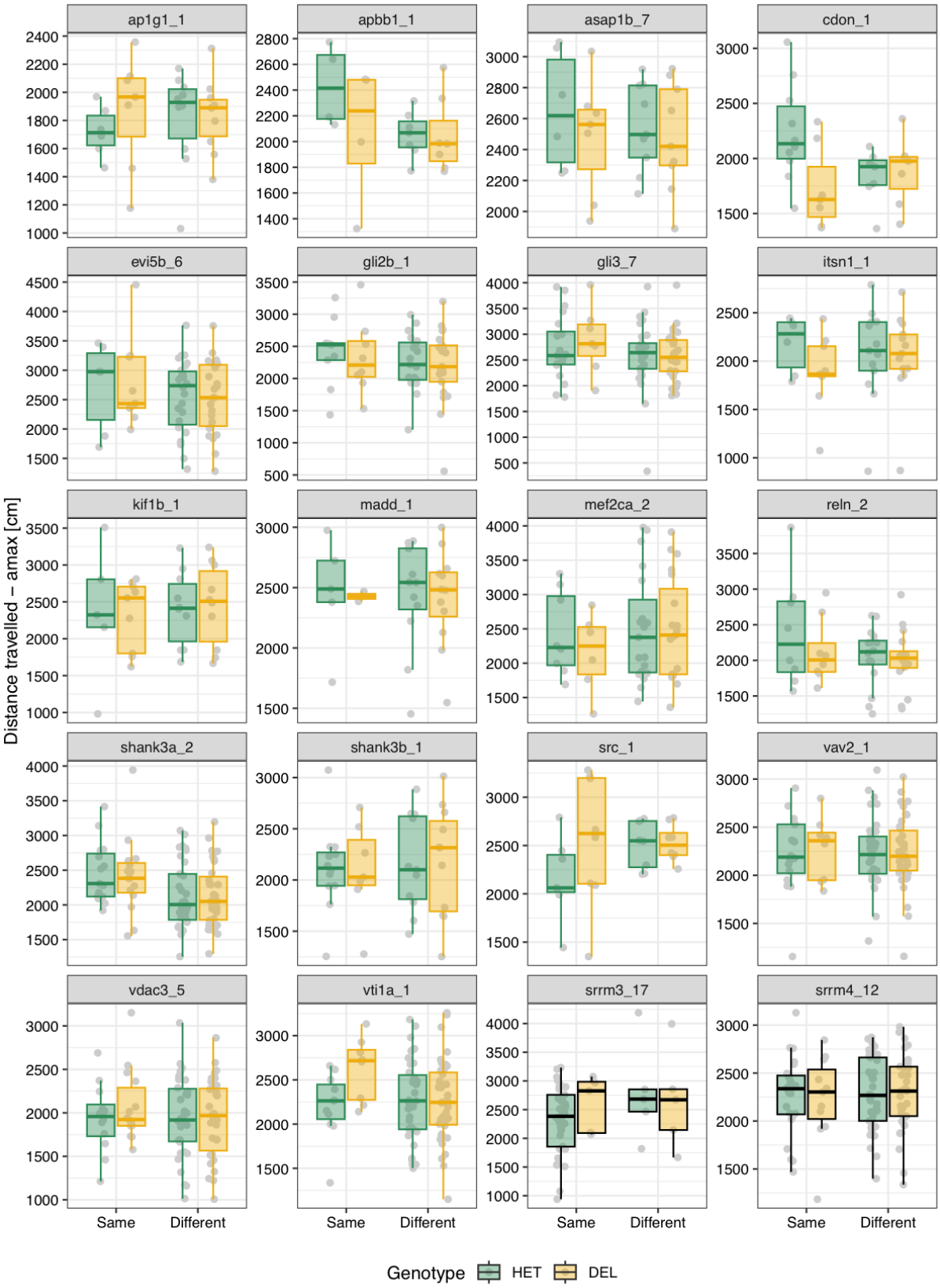

Figure 5 - figure supplement 5: Median distance traveled by genotype for each main microexon and regulator line. A) Median distance traveled (cm) for each fish over the 10' time course by pair type. "Same" corresponds to either Het-Het or Del-Del pairs and "Different" to Het-Del pairs. None of the comparisons between Het and Del individuals were significant at a threshold of $P < 0.01$ using Wilcoxon Rank-Sum tests.

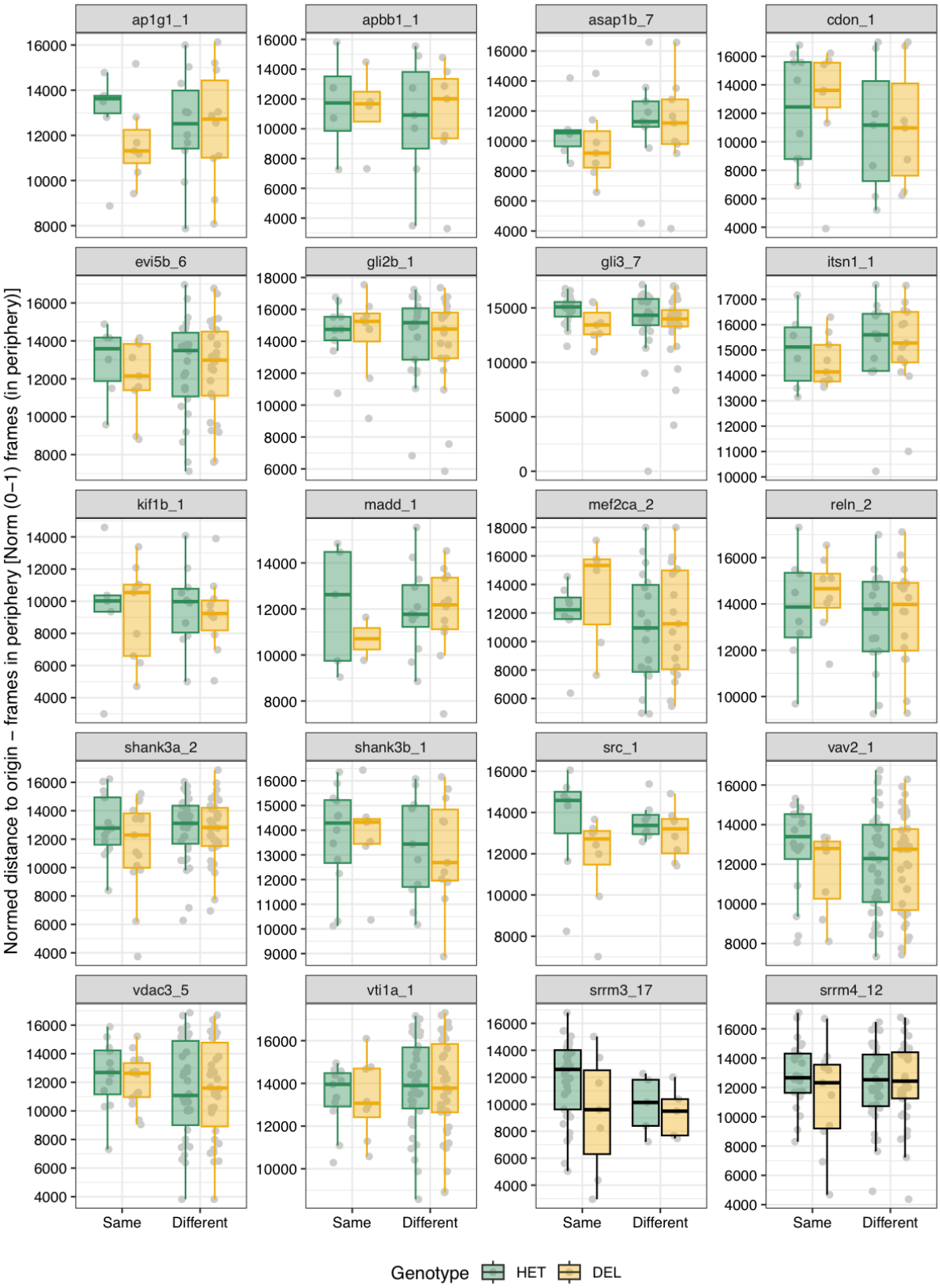

Figure 5 - figure supplement 6: Time in the periphery by genotype for each main microexon and regulator line. A) Median normalized frames in periphery (from 0 to 1) for each fish over the 10' time course by pair type. "Same" corresponds to either Het-Het or Del-Del pairs, and each data point is the median of the pair, and "Different" to Het-Del pairs and each data point corresponds to an individual fish. None of the comparisons between Het and Del individuals were significant at a threshold of $P < 0.01$ using Wilcoxon Rank-Sum tests.

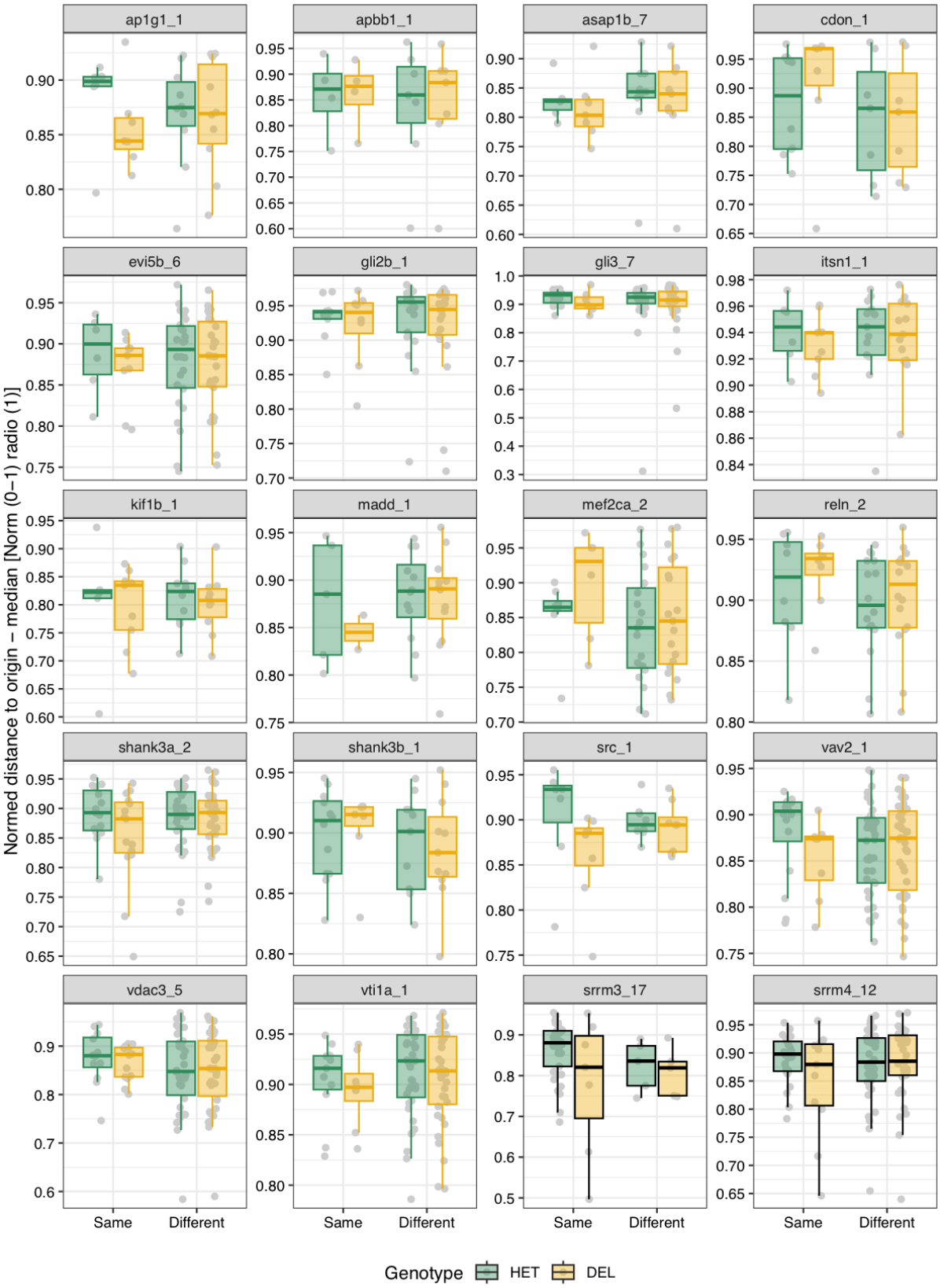

Figure 5 - figure supplement 7: Median normalized distance to origin by genotype for each main microexon and regulator line. A) Median normalized distance to origin/center (from 0 to 1) for each fish over the 10' time course by pair type. "Same" corresponds to either Het-Het or Del-Del pairs, and each data point is the median of the pair, and "Different" to Het-Del pairs and each data point corresponds to an individual fish. None of the comparisons between Het and Del individuals were significant at a threshold of $P < 0.01$ using Wilcoxon Rank-Sum tests.

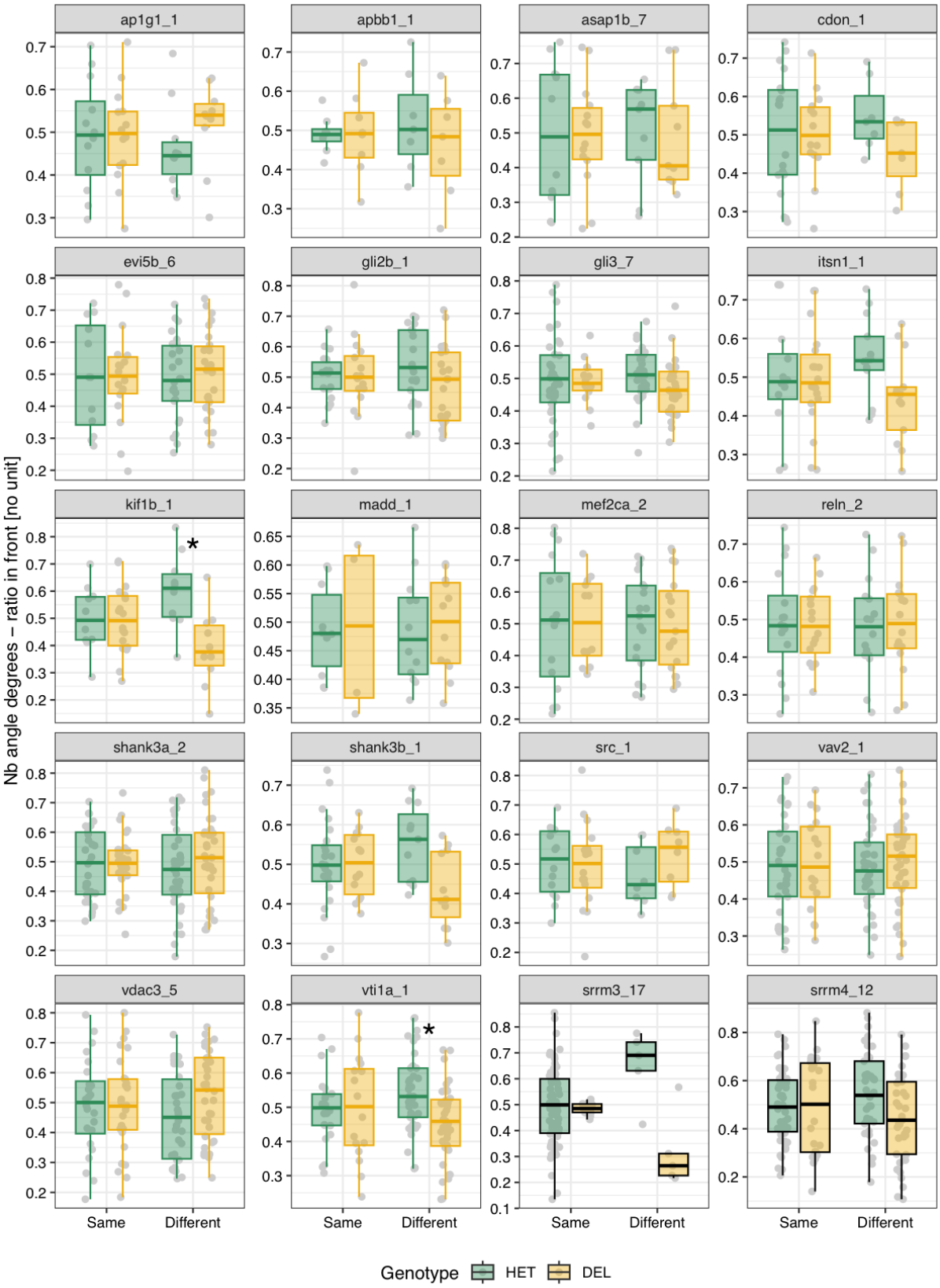

Figure 5 - figure supplement 8: Ratio neighbor in front by genotype for each main microexon and regulator line. A) Median ratio neighbor (nb) in front (from 0 to 1) for each fish over the 10' time course by pair type. "Same" corresponds to either Het-Het or Del-Del pairs and "Different" to Het-Del pairs. In both cases, each data point corresponds to an individual fish. None of the comparisons between Het and Del individuals were significant at a threshold of P < 0.01 using Wilcoxon Rank-Sum tests.

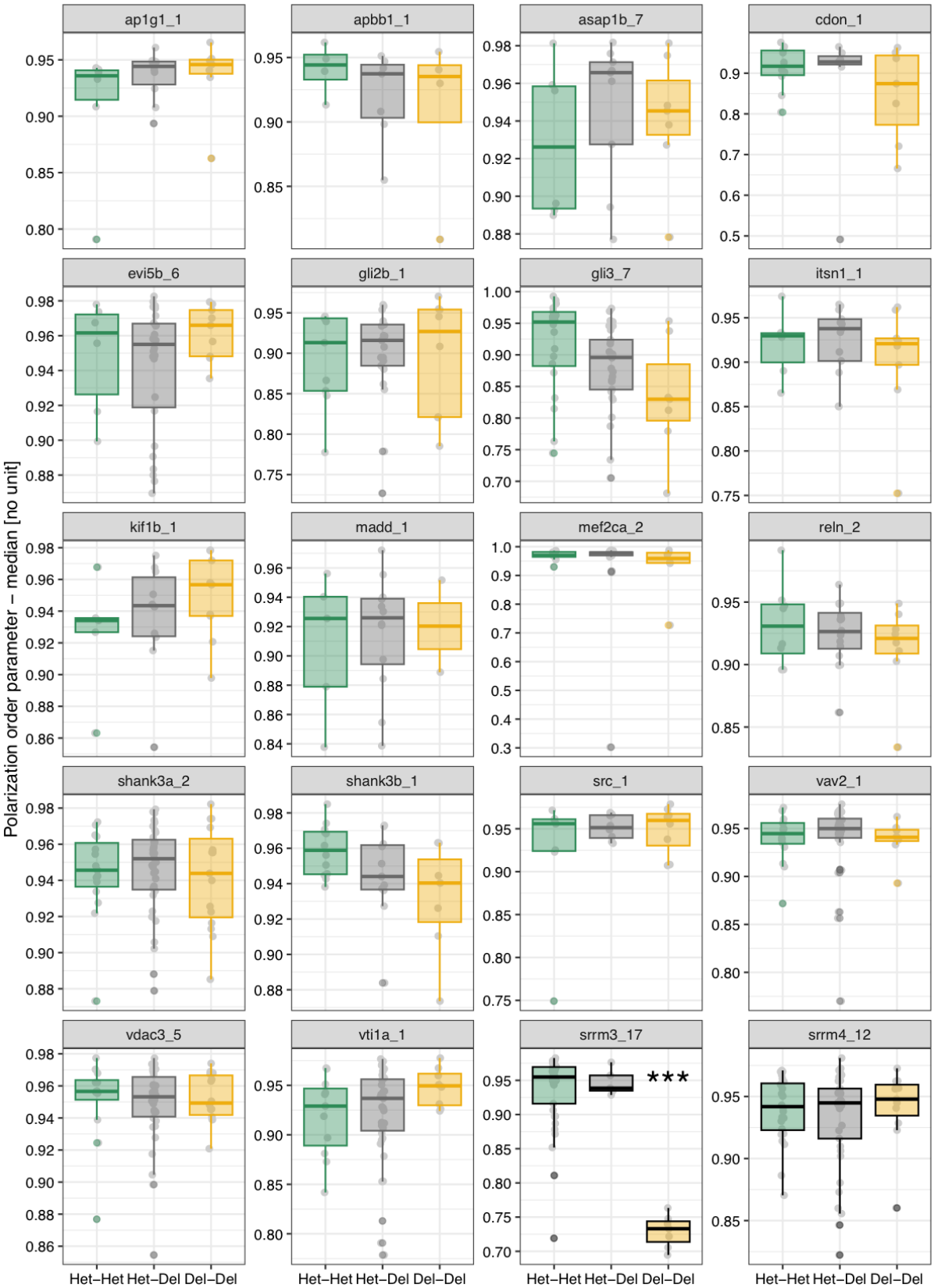

Figure 5 - figure supplement 9: Polarization by genotype pair combination for each main microexon and regulator line. A) Median value of the polarization order parameter (1 = fully concordant vectors) for each fish pair over the 10' time course by pair type (Het-Het, Het-Del and Del-Del). P-values correspond to Wilcoxon Rank-Sum tests. *** $p < 0.0001$.

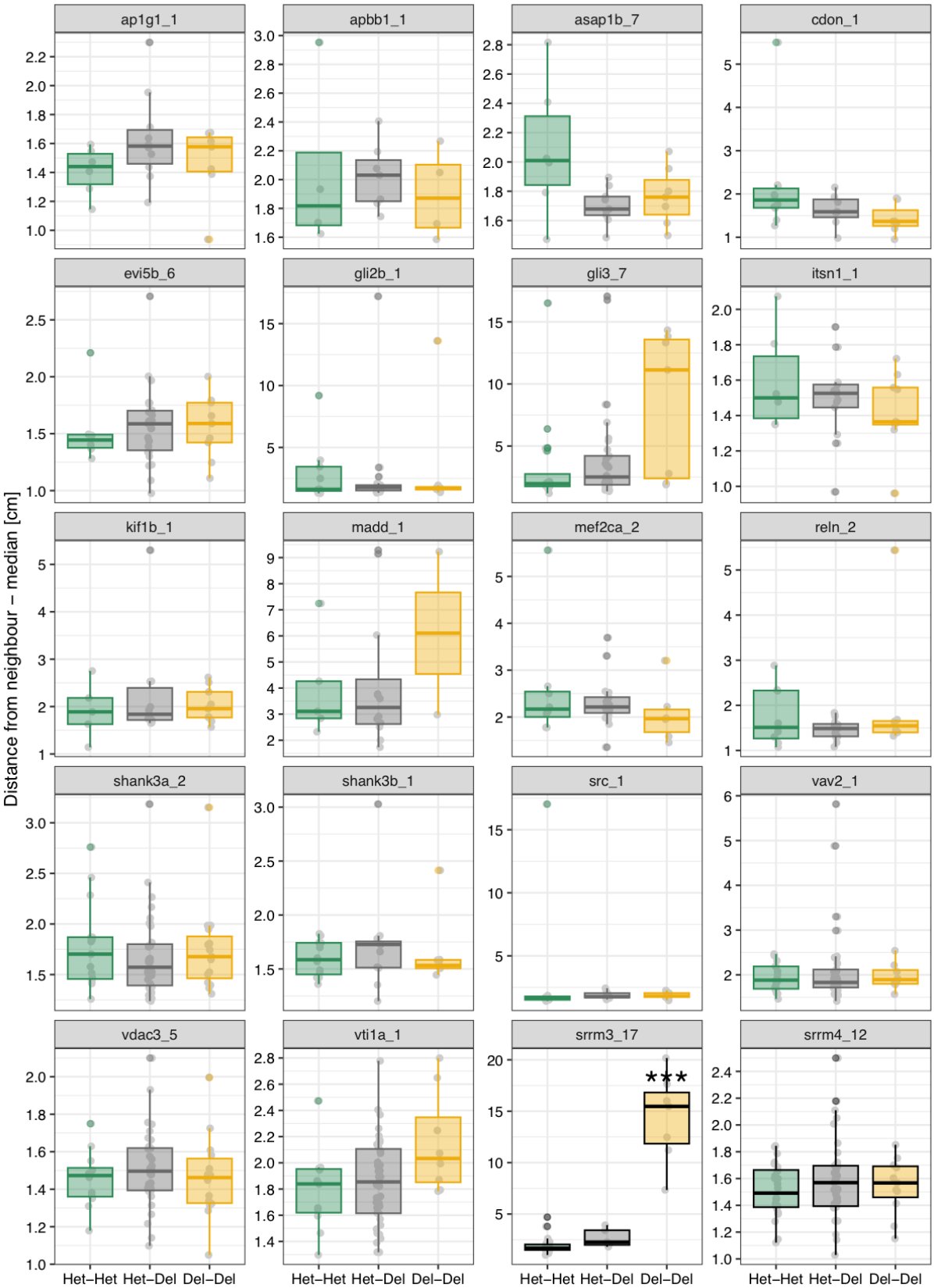

Figure 5 - figure supplement 10: Interindividual distance by genotype pair combination for each main microexon and regulator line. A) Median distance to neighbor (cm) for each fish pair over the 10' time course by pair type (Het-Het, Het-Del and Del-Del). P-values correspond to Wilcoxon Rank-Sum tests. *** $p < 0.0001$.

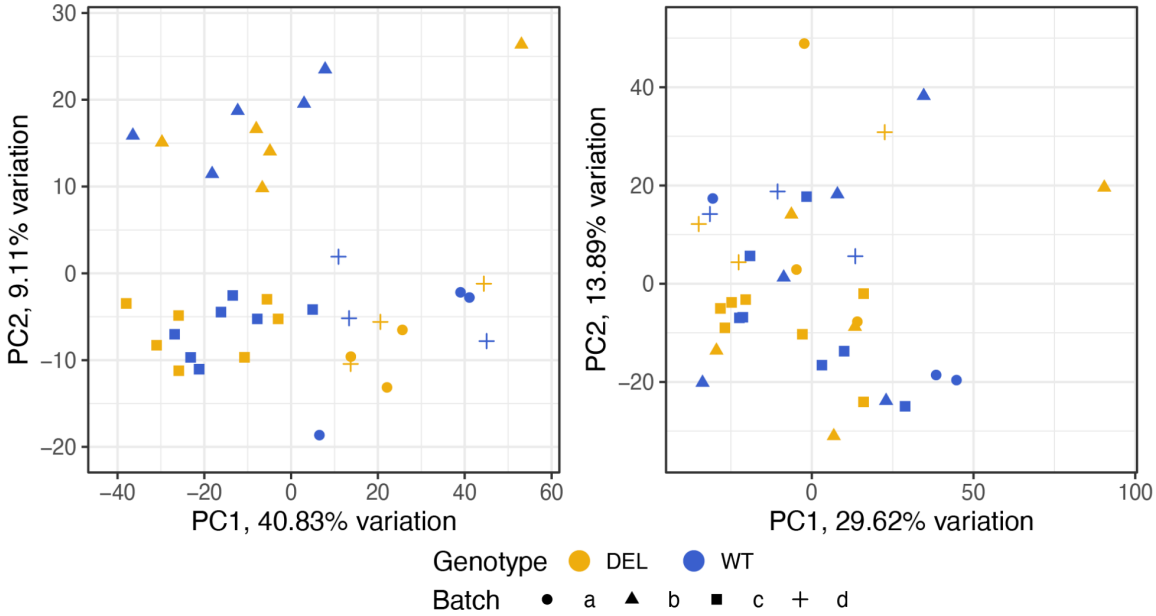

Figure 6 - figure supplement 1: Batch correction of RNA-seq data. Principal component analysis (PCA) on raw log10 transformed gene counts (left) and after (right) degradation correction, normalization and batch correction using *DegNorm*, *DESeq2* (VST) and *WCGNA* (Empirical Bayes-moderate adjustment), Bioconductor-packages, respectively.

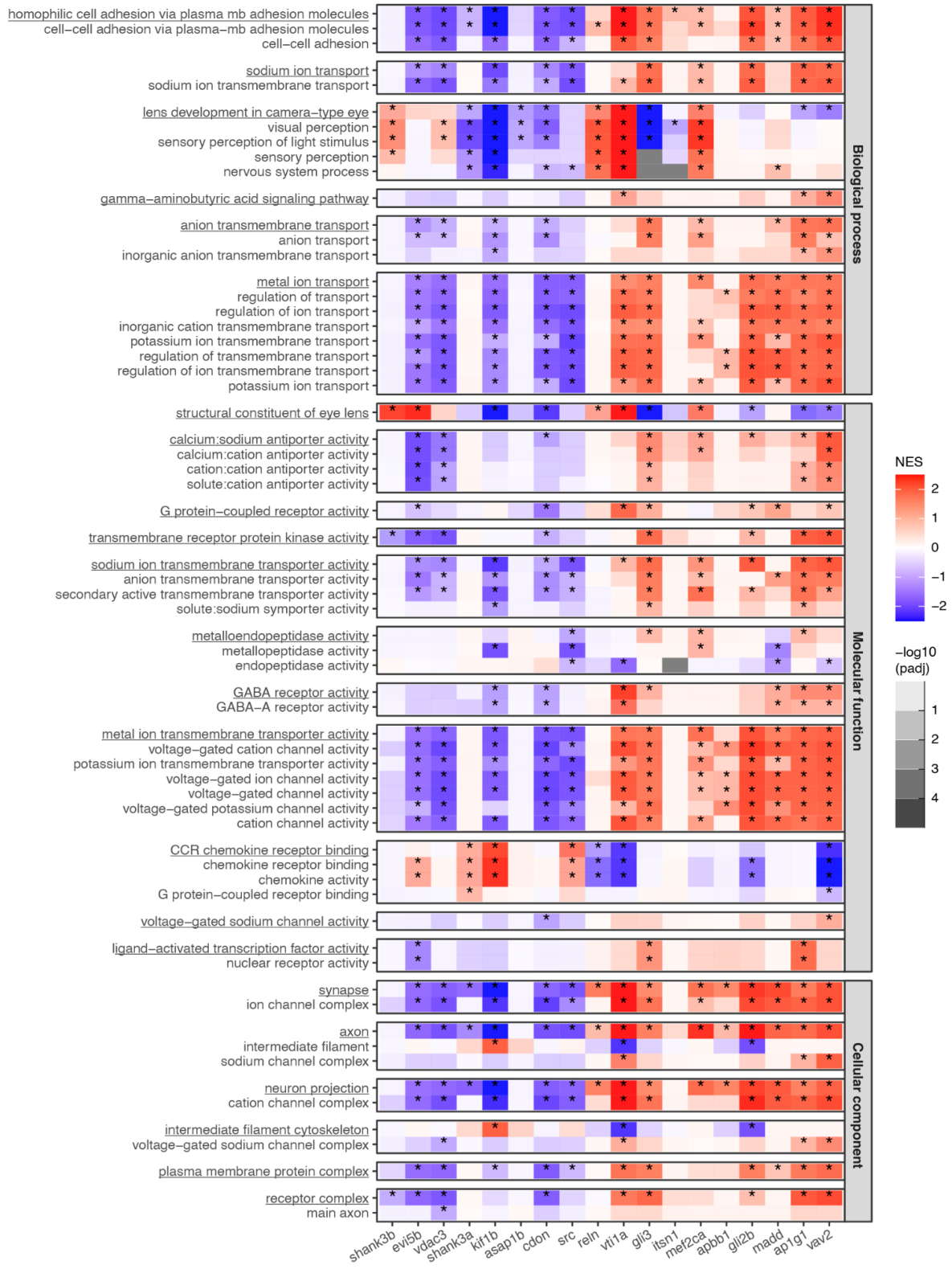

Figure 6 - figure supplement 2: Enriched GO categories. Enrichment of individual GO categories from categories groups highlighted in Figure 6C for each microexon deletion. Each block is a group of related GO categories and the block is named after the underlined category. Values obtained from Gene Set Enrichment Analyses (GSEA).